

Nonequilibrium Processes in Polymer Membrane Formation: Theory and Experiment

Marcus Müller* and Volker Abetz*



Cite This: *Chem. Rev.* 2021, 121, 14189–14231



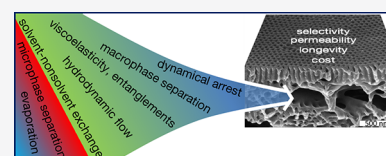
Read Online

ACCESS |

Metrics & More

Article Recommendations

ABSTRACT: Porous polymer and copolymer membranes are useful for ultrafiltration of functional macromolecules, colloids, and water purification. In particular, block copolymer membranes offer a bottom-up approach to form isoporous membranes. To optimize permeability, selectivity, longevity, and cost, and to rationally design fabrication processes, direct insights into the spatiotemporal structure evolution are necessary. Because of a multitude of nonequilibrium processes in polymer membrane formation, theoretical predictions via continuum models and particle simulations remain a challenge. We compiled experimental observations and theoretical approaches for homo- and block copolymer membranes prepared by nonsolvent-induced phase separation and highlight the interplay of multiple nonequilibrium processes—evaporation, solvent–nonsolvent exchange, diffusion, hydrodynamic flow, viscoelasticity, macro- and microphase separation, and dynamic arrest—that dictates the complex structure of the membrane on different scales.



CONTENTS

1. Introduction	14189	5.3. Influence of Solvent Evaporation Rate and Time	14213
2. Types of Membranes	14191	5.4. Self-Assembly in the Casting Solution	14214
2.1. Polymer Membranes: Rich Potential Due to Nonequilibrium	14191	5.5. Time-Resolved Studies of the Membrane-Structure Formation	14215
2.2. Block Copolymer Membranes	14191	5.6. Continuum Models for Studying Solvent Evaporation from Block Copolymer Films	14217
3. Thermodynamics of Membrane-Forming Systems	14191	5.7. Studying Solvent Evaporation from Block Copolymer Films by Particle Simulation	14219
3.1. Polymer–Solvent Mixtures	14192	6. Conclusions and Perspectives	14220
3.1.1. Ternary Mixtures of Polymer, Solvent, and Nonsolvent	14193	Author Information	14222
3.2. Self-Assembly of Block Copolymer in Solutions and Melts	14194	Corresponding Authors	14222
4. Homopolymer Membranes	14196	Notes	14222
4.1. Phase-Inversion Membranes	14196	Biographies	14222
4.2. Scope and Goals of Modeling	14197	Acknowledgments	14222
4.3. Continuum Models	14199	Additional Notes	14223
4.3.1. General Considerations	14199	References	14223
4.3.2. Free-Energy Functional for Spatially Inhomogeneous Systems	14199		
4.4. Particle Simulations	14203		
4.5. Applications to Nonsolvent-Induced Phase Separation (NIPS)	14204		
4.5.1. Continuum Models	14204		
4.5.2. Particle Simulations	14210		
5. Block Copolymer Membranes	14210		
5.1. Substructure of Isoporous Integral-Asymmetric Membranes	14212		
5.2. Influence of Solvent Quality and Selectivity on the Formation of an Isoporous Film Surface	14212		

1. INTRODUCTION

Sustainability is an increasingly important issue for many industrial processes, and, as a consequence, there is the need to develop technologies which are less energy consuming, less polluting, and more safe in operation. In the area of separation of

Special Issue: Molecular Self-Assembly

Received: January 11, 2021

Published: May 25, 2021



liquid or gaseous mixtures, in many cases membrane technology can contribute to energy savings and therefore a reduced carbon dioxide footprint compared to other technologies, such as, e.g., distillation.¹ Moreover, separation through a selective membrane also occurs under milder conditions. This is important in the case of purification of sensitive molecules, which would decompose, e.g., in the course of thermal separation, and opens up opportunities for separation membranes in biomedical applications.

Bechhold reported on membrane-based separations of colloids at the beginning of the 20th century.² After the initial work on tubular cellophane (regenerated cellulose) membranes as an artificial kidney by Kolff and Berk, published in 1944,³ hemodialysis became a prominent application of membrane technology.^{4,5} The first technically used membranes were porous in nature and were used for microfiltration (filtering particles in the range of 10 μm to 100 nm) and later for ultrafiltration (filtering particles and molecules in the range of 100 to 10 nm). Today, polymeric materials are still the most commonly employed materials both in microfiltration and ultrafiltration. The market for membranes is expected to increase significantly in the future due to the need for drinking water, industrial water, renewable energies, and sustainable processes for an increasing world population.^{6–8} The first membranes produced on a commercial scale were microfiltration membranes from the Membranfiltergesellschaft Sartorius-Werke in Göttingen, Germany, a company that still exists today, *inter alia* illustrating the ongoing relevance of membrane technology.⁹

The first membrane materials were based on derivatized cellulose, such as nitrocellulose or cellulose acetate. Because of limitations of cellulose materials in terms of chemical and thermal stability, synthetic polymers also were used for microfiltration and ultrafiltration membranes, with polysulfones, polyacrylonitrile, or poly(vinylidene fluoride) being the most prominent ones. Nowadays filtration membranes are used in many technical applications, such as the purification of water and air, medicine, biotechnology, food processing, or the chemical industry.^{4,9,10} Besides porous membranes, there are also dense membranes for large-scale applications such as desalination of seawater by reverse osmosis¹¹ and separation of gases (oxygen enrichment in air, purification of natural gas, separation of carbon dioxide or hydrogen from various gas streams, to mention just the most prominent examples).¹² Polymer-based membranes play an important role in all these applications, as they are comparably inexpensive in production and handling; however, also in the field of inorganic membranes, there are significant developments, although their production is more expensive.^{13,14}

Notwithstanding these advances, there is still a need and opportunities for improving membranes for a multitude of applications and also for their employment in new separation tasks. For example, irreversible fouling and scaling are problems, limiting the service time of membranes in pressure-driven separation processes such as water purification.^{8,15,16} In the petrochemical industry, a challenging separation task for membrane technology is the separation of olefins from paraffins, due to their similar size.¹⁷ So far, this separation is carried out by energy-intensive cryogenic distillation. Other challenges for membrane technology are the separation of biomacromolecules, such as mixtures of similar-sized proteins.^{18,19}

In this review, we focus on porous polymer membranes that still pose significant challenges for current membrane technology, such as, e.g., fouling or scaling of membranes during

operation,^{20–22} aging (densification with time),²³ or compaction (densification caused by large transmembrane pressure²⁴). These issues are strongly related to the membrane material itself, the membrane structure, and the operation conditions of the membrane separation process. Another challenge in the design of porous polymer membranes consists of simultaneously achieving high density of similar-sized short pores per unit area and mechanical stability, so that a high size selectivity and a high flux can be realized at the same time. This aim can be accomplished by integral-asymmetric isoporous membranes with a rather thin selective layer, supported by an open porous substructure in a single-step procedure based on the so-called nonsolvent-induced phase separation (NIPS), also known as “phase-inversion process”. This technique has been first established for cellulosic membranes by Loeb and Sourirajan.²⁵ As the envisioned pore sizes are in a range from a few nanometers up to a few tens of nanometers, self-assembling block copolymers have become a class of exciting candidates to fabricate a new generation of ultrafiltration and nanofiltration membranes based on NIPS.^{26,27} The NIPS process leads to a nonequilibrium structure, and it depends on a variety of materials and process parameters. This is already true for homopolymer membranes, and in the case of self-assembling block copolymers the fabrication process increases in complexity, as microphase separation and macrophase separation must be properly organized on both length and time scales in order to obtain a membrane with the desired structure.

So far, the literature has reported mainly on the preparation and characterization of these novel block copolymer membranes,^{27,28} whereas much less is known about the structure formation itself. Experimental investigations of the kinetics of structure formation on different scales are challenging, but some progress has been achieved, e.g., by cryogenic electron microscopy,²⁹ time-resolved grazing-incidence small-angle X-ray scattering (GISAXS),^{30–36} or real-time atomic force microscopy (AFM) imaging^{37,38} as well as in situ small-angle neutron scattering (SANS).³⁹ At the same time, there are significant advances in modeling and simulation techniques. Nowadays, highly coarse-grained particle models can investigate systems with 10^9 particles, addressing structure formation on the length scale of a micrometer and times scales of seconds and beyond.⁴⁰ Whereas the complexity of the fabrication processes and the wide span of time and length scales remain a substantial challenge for modeling and computation, the scales that can be addressed by continuum models and highly coarse-grained particle models start to converge toward the scales that are relevant for applications and studied by experiments. This overlap of experimental and computational scales is expected to widen in the near future and will allow for advances in understanding the nonequilibrium formation mechanism of polymer membranes and thereby contribute to guide the design of membrane-formation processes.

The growing need for membranes, the use of more complex macromolecular materials and fabrication processes in experiments, and advances in model building and computation motivated us to write this tutorial review, combining experiment and theory. We aim to provide a unified perspective on the nonequilibrium processes that dictate the large-scale morphologies in thin films and membranes by solvent evaporation, NIPS, and molecular self-assembly. Given the abiding interest that membrane fabrication has attracted since the seminal works of Bechhold,² Kolff and Berk,³ and Loeb and Sourirajan,²⁵ we cannot aim for a comprehensive overview but have selected

topics related to membrane structure and its nonequilibrium formation processes to highlight common aspects of experiment and theory. Therefore, various important and challenging topics of interest such as, e.g., solvent evaporation from homopolymer mixtures,^{41–44} solvent annealing of copolymer films,^{45–51} directing the orientation of membrane pores by electric fields,^{52–71} polymerization-induced phase-separation (PIPS),⁷² or polymerization-induced self-assembly (PISA)^{73–75} have not been covered. Functionalization of membrane pores^{76,77} and molecular transport on the atomic scale in the membranes⁷⁸ that are critical for the operation of membranes are also not addressed in the following.

2. TYPES OF MEMBRANES

In membrane-based separation technologies, different types of membranes are used that can be categorized by the material they are made of (polymer, ceramic, metal, or combinations thereof)⁷⁹ and their overall geometry (flat sheet or also spiral wound, as well as tubular, hollow fiber, nanofibrous membranes). They can further be distinguished by the structure of their cross-section, which can be symmetric or asymmetric.^{4,9,10} Most importantly, membranes are characterized by their separation properties. Selective separation can occur all over the cross-section of a membrane in symmetric membranes or it occurs at its surface in asymmetric membranes. The separation layer can be dense or porous on different length scales. According to IUPAC, nanometer-sized pores are categorized into micropores (<2 nm), mesopores (~2–50 nm), and macropores (>50 nm).⁸⁰ In the literature about porous membranes, however, another classification is often used: Nanofiltration, ultrafiltration, and microfiltration membranes are characterized by pore-size ranges, which are approximately 1–10 nm, 1–100 nm, and 0.1–10 μm , respectively. Sometimes, there are also overlaps between the different pore-size regions in this nomenclature. Reverse-osmosis membranes for desalination and dense membranes for gas separation have “pore” sizes below ~1 nm.

2.1. Polymer Membranes: Rich Potential Due to Nonequilibrium

The physical and structural properties of polymer materials depend on their processing and thermal history.^{81,82} This is very important for the preparation of polymer membranes, and there are many examples of membranes differing in their structure and thus functional properties but being made of the same polymer.^{4,83,84} This demonstrates that the polymer materials do not reach a unique thermodynamic equilibrium but rather become trapped in a nonequilibrium state. This nonequilibrium state may be metastable; i.e., there exist large free-energy barriers that the system has to overcome by a thermally activated process to finally equilibrate,⁸² or its relaxation is kinetically prevented by alternate phenomena such as, e.g., vitrification, crystallization, and chemical cross-linking (gelation), or combinations thereof.

NIPS is of particular interest in the field of porous polymer membranes, as it leads to so-called integral-asymmetric membranes, which consist of a rather thin selective layer on top of a more open, porous support structure of the same material. The advantage of such a structure is its combination of high selectivity by the top layer and high flux by the fact that the top layer is kept thin and the more open, porous substructure does not considerably contribute to the resistivity of the flux. These integral-asymmetric structures result from a complex interplay of thermodynamics and kinetics during their formation

from solution. While the top layer is relatively dense and phase separation occurs on the length scale of the macromolecules themselves or close to it, the lower parts of the membrane typically display macrophase separation. Many experimental studies on such membranes have investigated the influence of different processing parameters on this structure. In order to prepare a membrane with the desired structure, the parameters have to be judiciously chosen, which requires a series of experiments for any new membrane.

2.2. Block Copolymer Membranes

Block copolymers are well-known for their fascinating ability to self-assemble into a variety of microphase-separated structures on a mesoscopic length scale, depending on the chemical composition, degree of polymerization, and molecular topology.^{85,86} This allows different properties, such as mechanical or permeation properties, to be combined. A low-disperse block copolymer with a suitable composition and molecular weight may be transformed into a membrane with cylindrical,^{26,87,88} gyroidal,⁸⁹ or lamellar pores,^{90,91} respectively. Because of the low dispersity of such a tailor-made block copolymer, the microdomains will also have a low size dispersity.

There are different ways to prepare membranes from block copolymers. They can be prepared by casting a block copolymer solution onto a substrate and evaporating the solvent sufficiently fast in order to achieve the desired alignment of the microdomains in the perpendicular direction.⁹² Also an electric field can be applied to align, e.g., cylindrical domains.⁸⁷ After the pore-forming block is etched away to obtain open pores, the film is transferred from the solid substrate onto a porous support.⁹³ This method, however, involves many steps and is difficult to upscale. The formation of integral-asymmetric membranes from self-assembling block copolymers is a possible way to obtain membranes with an almost isoporous top layer on a more open porous sublayer of the same material. These membranes can be prepared directly on a porous nonwoven support, once an appropriate set of experimental parameters has been determined. The process parameters that dictate the nonequilibrium structure formation are the main focus of this review.

Early on, it has been recognized that two distinct sets of factors dictate the membrane structure: (i) the equilibrium thermodynamics of the multicomponent system and (ii) the processing conditions as quantified, e.g., by the magnitude of the overall material transfer between film and bath during the coagulation process.⁹⁴ In the following, we discuss these two aspects in turn.

3. THERMODYNAMICS OF MEMBRANE-FORMING SYSTEMS

The thermodynamics of membrane formation chiefly involves macroscopic phase equilibria between polymer, solvent, and nonsolvent, and, in the case of block copolymer membranes, the microphase separation between the different components of the block copolymer material. The equilibrium thermodynamics is dictated by the choice of the polymer, i.e., its molecular architecture and its interaction with the solvent and nonsolvent, the composition of the multicomponent mixture, and the thermodynamic state variables, such as temperature or pressure. Equilibrium thermodynamics provides a useful starting point for describing the underlying phase separation and the stability or metastability of homogeneous systems.

3.1. Polymer–Solvent Mixtures

The thermodynamics of polymer solutions has attracted abiding interest, both because it is important for polymer analytics, polymer processing, and many other applications and because of the intriguing interplay between single-chain properties and collective phase behavior.^{95,96} Depending on the thermodynamic interactions between polymer and solvent in a macroscopic homogeneous solution, good and poor solvents are distinguished. The quality of a solvent for a given polymer depends on its chemical structure, but also temperature affects the interactions between solvent and dissolved polymer. In a good solvent, the polymer swells because there is an effective repulsion between polymer segments that can be quantified by the second-order virial coefficient. In this case, the polymer's root mean-squared end-to-end distance, R_e in a homogeneous solution scales like a self-avoiding walk, $R_e \sim N^{\nu_{SAW}}$ with $\nu_{SAW} \approx 0.588$, where N denotes the number of repeating units. At the Θ -point, the pairwise interactions between polymer and solvent balance, and a long linear polymer adopts a random-walk behavior, $R \approx N^{\nu_{RW}}$ with $\nu_{RW} = 1/2$; i.e., the conformations obey Kuhn's law of a "random-flight chain". In good solvents or under Θ -condition, dilute polymer solutions can be analyzed by static light scattering to obtain the weight-averaged molecular weight, the z -average of the radius of gyration, and the second-order virial coefficient. Osmometry can be used to determine the number-averaged molecular weight and the second virial-order coefficient, ν , or the related Flory–Huggins interaction parameter.⁹⁵ If the polymer density increases to the semidilute or concentrated regime, polymer chains will overlap, and the effective repulsion, $\nu > 0$, between polymer segments in a good solvent will be screened by the presence of the neighboring chains; i.e., stretching no longer reduces the number of repulsive polymer–polymer contacts. As light scattering cannot resolve individual chains in a melt, the Θ -condition was proven by SANS using a deuterated chain in a nondeuterated chain matrix.⁹⁷

If the solvent is poor, in turn, an individual macromolecule collapses into a droplet, whose interior has a finite density, i.e., $R_e \sim N^{1/d}$, where $d = 3$ denotes the dimension of space. In a multichain system, the polymers will aggregate with other chains and precipitate; i.e., they form a polymer-rich phase that coexists with a solvent-rich phase. A typical phase diagram is shown in Figure 1, where we have assumed that the effective pairwise interaction, ν , between polymer segments, measured in units of the thermal energy $k_B T$, decreases with temperature. The phase diagram depicts the densities of the polymer-rich and solvent-rich phases (binodals) as well as the stability limits of the homogeneous states (spinodal). The interior of an individual, collapsed, infinitely long macromolecule resembles this polymer-rich phase.

A popular description of the thermodynamics of an incompressible polymer-(non)solvent mixture within mean-field theory is provided by the Flory–Huggins excess free energy of mixing^{98,99}

$$\frac{\Delta F(\phi_p)}{\rho V k_B T} = \frac{\phi_p \ln \phi_p}{N} + \phi_N \ln \phi_N + \chi_{PN} \phi_p \phi_N$$

with $\phi_p + \phi_N = 1$ (1)

where V is the volume of the system and ρ stands for the segment density. In the case of phase separation, the solvent is poor, and therefore we denote its density by ϕ_N (nonsolvent). Here, we have assumed for simplicity that the specific volumes of polymer

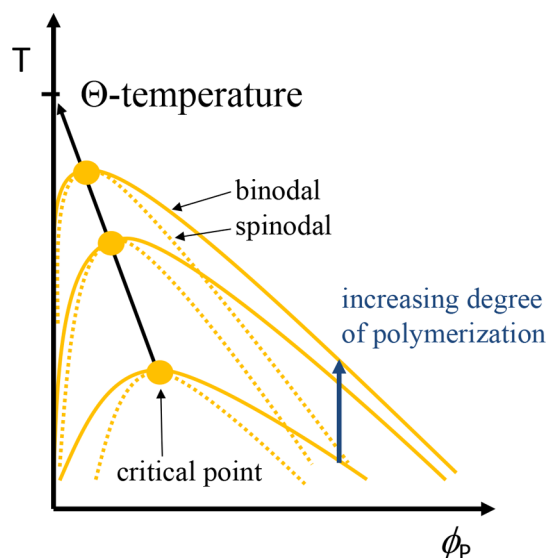


Figure 1. Sketch of the phase diagram of a polymer–solvent mixture with an upper critical solution temperature (UCST), for different degrees of polymerization, N . Binodals (solid lines) denote the densities of the coexisting, polymer-rich, and solvent-rich phases, whereas (mean-field) spinodals (dotted lines) indicate the stability limits of the homogeneous polymer-rich and solvent-rich domains.

and nonsolvent are N/ρ and $1/\rho$, respectively. This also allows us not to distinguish between concentration and density. The first two terms denote the entropy of mixing polymer and solvent, and the second term accounts for the incompatibility, χ_{PN} , between polymer and nonsolvent. To a first crude approximation, the second-order virial coefficient and the Flory–Huggins parameter are related by $\chi_{PN} \approx 1/2 - \nu$.

Within mean-field approximation, the phase diagram features a critical point at the incompatibility $\chi_{PN}^c = \frac{1}{2}(1 + 1/\sqrt{N})^2$, and the critical polymer density decreases with increasing chain length, $\phi_p^c = 1/(1 + \sqrt{N})$. Thus, for $N \gg 1$, the phase diagram is highly asymmetric. In the limit $N \rightarrow \infty$, the critical point converges to the Θ -point. In contrast to the mean-field description of the phase behavior of dense binary polymer blends, density fluctuations have a rather pronounced effect on the phase behavior of the polymer–nonsolvent mixture, and we refer the reader to refs 95 and 100–104 for further discussion. Using standard thermodynamic relations, one can calculate the chemical potential, μ , and pressure, p , of a spatially homogeneous system. Requiring that the two coexisting phases—polymer-rich and nonsolvent-rich—have the same pressure and chemical potential for a given temperature T , one obtains the binodals. The homogeneous system becomes unstable at the spinodal density, given by the requirement, $d^2 F/d\phi_p^2 = 0$. The phase diagram including binodals, spinodals, and the critical point is depicted in Figure 1.

The nonequilibrium formation of porous polymer membranes from solutions involves phase separation between polymer and (non)solvent(s). In the case of a binary polymer–(non)solvent mixture, the miscibility gap can be entered either (i) via a change of temperature (or effective polymer interaction, $\nu < 0$) or (ii) by a variation of the polymer density, ϕ_p .

Case (i) corresponds to thermally induced phase separation (TIPS). This method is mainly used to produce membranes from polymers that are difficult to dissolve and soluble only at

elevated temperatures, like polyolefins such as, e.g., polypropylene, polyethylene, or poly(vinylidene fluoride) (PVDF).¹⁰⁵ The phase separation upon cooling is coupled with crystallization in the case of these polymers. However, TIPS can also be applied to other polymers such as polystyrene¹⁰⁶ and poly(2,5-dimethyl-1,4-phenylene ether),¹⁰⁷ when dissolved in cyclohexanol. A special type of TIPS was observed for a solution of PVDF with cellulose acetate in a mixture of a good solvent (dimethylformamide) and a nonsolvent (nonane). The solvent–nonsolvent mixture itself shows an upper critical solution temperature below the temperature of the initial polymer solution. Therefore, the solution phase separates upon cooling, resulting in a highly surface-porous polymer film, where the pore size is dictated by the length scale of spinodal decomposition.¹⁰⁸ The subsequent phase separation, which leads to an increase of the pore size with time, is then stopped by quenching the whole system in a cold coagulant. The pore-size distribution of such membranes, however, is less regular as compared to block copolymer membranes.

The latter case (ii) corresponds, e.g., to the (slow) evaporation of a moderately poor solvent from an initially very dilute solution of collapsed coils. Then, upon decreasing the solvent density, the polymer precipitates when the binodal is crossed via the nucleation and growth of individual droplets of the polymer-rich phase. Since the binodal of the polymer-lean phase occurs at rather small polymer density, the precipitated polymer droplets do not connect well. Thus, the evaporation of a poor solvent from a dilute solution will hardly lead to a useful membrane, and membrane formation often involves a mixture of a polymer and multiple solvents, which differ in volatility and miscibility with the polymer.^a

3.1.1. Ternary Mixtures of Polymer, Solvent, and Nonsolvent. The phase diagram of an incompressible three-component system—polymer, solvent, and nonsolvent—or, equivalently, of a compressible, two-component system can already be fairly complex. In fact, such a system may exhibit six qualitatively different types of phase diagrams according to the classification of van Konynenburg and Scott.¹⁰⁹ Thus, accurate equation-of-state data are an indispensable prerequisite for modeling. In the following, we will consider the typical case where one solvent is compatible with the polymer, whereas the other—nonsolvent—is a poor solvent for the polymer; the two solvents, however, remain miscible in the range of thermodynamic conditions of interest. An incompressible system is described by two thermodynamically independent order parameters, e.g., the normalized density, ϕ_P , of the polymer and the normalized density, ϕ_N , of the nonsolvent—because the densities of polymer, solvent, and nonsolvent add up to unity, $\phi_P + \phi_S + \phi_N = 1$, at each point in space. These two order parameters suffice to describe the macrophase separation between polymer and nonsolvent as the solvent is exchanged in the course of NIPS.

To a crude, first approximation, we can restrict the discussion to the phase separation between polymer and nonsolvent; i.e., one lumps the polymer and the miscible solvent together. In the final equilibrium state, the density of the solvent is vanishingly small, and such an effective two-component description becomes appropriate. The thermodynamic incompatibility between polymer and nonsolvent or between two components of an AB block copolymer is described by a Flory–Huggins parameter, χ_{PN} or χ_{AB} , respectively. Since the solvent dilutes the pairwise repulsion between polymer and nonsolvent or the different segments of the copolymer, the thermodynamic

incompatibility depends on the local solvent density, i.e., $\chi_{\text{eff}} = \chi_{PN}(\phi_S)$. Within the dilution approximation, one simply obtains¹¹⁰

$$\chi_{\text{eff}} \sim (1 - \phi_S) \quad (2)$$

If the solvent locally swells the polymer (i.e., semidilute solution), short-range correlations of polymer contacts result in a nontrivial dependence of the solvent density^{111–115}

$$\chi_{PN}(\phi_S) \sim (1 - \phi_S)^{(1 + \nu_{\text{SAW}}\omega_{12}) / (3\nu_{\text{SAW}} - 1)} \approx (1 - \phi_S)^{0.616} \quad (3)$$

where $\nu_{\text{SAW}} = 0.588$ is the scaling exponent of the extension of a self-avoiding random walk and $\omega_{12} \approx 0.4$ denotes the correction-to-scaling exponent that characterizes the contacts of two mutually interdigitating self-avoiding walks. Within this effective two-component description, the solvent density plays a similar role as temperature in Figure 1.

The Flory–Huggins description^{98,99} can be straightforwardly generalized to an incompressible polymer–solvent–nonsolvent system and takes the form

$$\frac{\Delta F(\phi_P, \phi_S, \phi_N)}{\rho V k_B T} = \frac{\phi_P \ln \phi_P}{N} + \phi_S \ln \phi_S + \phi_N \ln \phi_N + \chi_{PN} \phi_P \phi_N + \chi_{PS} \phi_P \phi_S + \chi_{NS} \phi_N \phi_S \quad (4)$$

$$\text{with } \phi_P + \phi_S + \phi_N = 1 \quad (5)$$

i.e., there are only two independent densities. In addition to the entropy of mixing, the excess free energy accounts for the three pairwise interactions, each being quantified by a Flory–Huggins parameter. In order to describe NIPS, polymer and nonsolvent are incompatible, $\chi_{PN} > 1/2$, whereas polymer and solvent as well as solvent and nonsolvent are miscible; i.e., $\chi_{PS} < 1/2$ and $\chi_{NS} < 2$. Note that this simple form ignores contact correlations mediated by the connectivity along the polymer backbone that give rise to the nontrivial dependence in eq 3, changes of the liquid packing as a function of density, as well as free-energy contributions due to a density dependence of macromolecular conformations in a homogeneous system. All these effects give rise to an additional density dependence of the interaction parameters.

An alternative to the Flory–Huggins free energy can be obtained by employing a third-order virial expansion, i.e.,

$$\frac{\Delta F(\phi_P, \phi_N)}{\rho V k_B T} = \frac{\phi_P \ln \phi_P}{N} + \phi_S \ln \phi_S + \phi_N \ln \phi_N + \sum_{\alpha\beta} \frac{v_{\alpha\beta}}{2} \phi_\alpha \phi_\beta + \sum_{\alpha\beta\gamma} \frac{w_{\alpha\beta\gamma}}{3} \phi_\alpha \phi_\beta \phi_\gamma \quad (6)$$

where the Greek indices run over all components of the system—polymer, solvent, and nonsolvent. Again, in the case of incompressibility, $\phi_P + \phi_S + \phi_N = 1$, the system is characterized by only two independent densities. In this case, the free-energy function requires three second-order virial coefficients and four third-order coefficients.

Higher-order density terms could be straightforwardly included if experimental data on the thermodynamics of the mixture were available. The third-order form, however, suffices to describe the qualitative aspects of the different types of phase diagrams that compressible binary mixtures exhibit. If the coefficients are not conceived as virial coefficients, resulting from a systematic small-fugacity expansion, but rather as effective parameters of an equation of state, the validity of the model is significantly extended. In addition to liquid–liquid

demixing such a free energy can also account for liquid–vapor phase equilibria.¹⁰⁹

These two bulk free-energy functions are simple top-down descriptions of the thermodynamics of the homogeneous system. They capture the ideal free energy of mixing and quantify the interactions between the species by a simple excess free energy. These free-energy functions predict the thermodynamics of a spatially homogeneous system. The parameters of the free-energy functional are identified by comparison to experiment, such as, e.g., equation-of-state data or scattering data.

Because of the incompressibility, $\phi_p + \phi_s + \phi_N = 1$, the phase diagram at a fixed temperature is typically represented in a phase triangle. Such a phase triangle (as shown in Figure 6 for a polymer–solvent–nonsolvent mixture, where the latter two components are miscible) provides an overview of the basic thermodynamic behavior of a spatially homogeneous system. Depending on the densities (which can be changed, e.g., by exchanging nonsolvent vs solvent), an incompressible ternary mixture remains homogeneous, or it undergoes macrophase separation into two coexisting phases, whose densities are given by the binodal. Tie lines connect the points on the binodals that represent the densities of the coexisting phases (i.e., the densities, where the chemical potentials of the two independent components and pressure are equal in both phases). Importantly, the bulk free energy also determines where, in the course of processing, spontaneous phase separation spontaneously sets in—the spinodal. This limit of metastability of a spatially homogeneous state is given by the condition that the matrix of second derivatives of ΔF with respect to the two independent densities has a vanishing eigenvalue or, equivalently, the determinant of the matrix vanishes. The corresponding eigenvector indicates the linear combination of densities that, initially, will exponentially grow over time.

Typically, polymer and solvent as well as solvent and nonsolvent are miscible at the thermodynamic states of interest. Macroscopic phase separation occurs between a polymer-rich and a polymer-lean phase. The latter phase predominantly consists of nonsolvent.

To a first approximation, the solvent, being miscible with both polymer and nonsolvent, dilutes the incompatibility between polymer and nonsolvent. As the solvent evaporates from the polymer film and the nonsolvent enters the film, polymer and nonsolvent densities increase. The critical point at which macrophase separation commences is located at small polymer density because of the small translational entropy of the long macromolecules. In the case of polymer membranes, the solvent almost completely evaporates, and polymer and nonsolvent are highly incompatible. Thus, the final equilibrium state often corresponds to the coexistence of an almost pure polymer, $\phi_p \approx 1$, and an almost pure nonsolvent, $\phi_N \approx 1$. Thus, if true thermodynamic equilibrium were to be achieved, a macroscopic, spatially homogeneous, dense polymer film would coexist with a nonsolvent.

Additionally, other properties that are relevant for the processing—in particular, the dynamic arrest of structure formation, such as vitrification or crystallization—are often indicated in the phase triangle. These effects cannot be predicted by the free-energy function, but they occur at specific thermodynamic conditions that are characterized by the two independent densities and temperature. This arrest of structure formation is essential for fixing the morphology of the membrane in a nonequilibrium state, instead of collapsing into

a dense, unstructured polymer film. Assuming that the dynamic arrest occurs rapidly compared to the time evolution of the domain morphology, one can estimate the local density of the polymer-rich domain by its value when this polymer-rich phase dynamically arrests. Likewise, the morphology of the membrane resembles the stage when the mobility of the polymer becomes vanishingly small.

A more quantitative description has to account for at least three additional aspects: (i) the spatial inhomogeneity of the system, (ii) the change of densities in the polymer film, as the solvent evaporates and the film thickness shrinks, as well as (iii) viscoelastic effects on the kinetics of phase separation.

3.2. Self-Assembly of Block Copolymer in Solutions and Melts

In comparison with homopolymers or random copolymers, the thermodynamic behavior of block copolymer solutions is quite different as the chemically different blocks typically differ in their mutual interactions and their interaction with the solvent(s).^b If the solvent is selective, i.e., it exhibits a better compatibility with one block than with the other, this favored block will be well dissolved and swell, whereas the other block will swell less or, in the case of a poor solvent for that block, even tend to segregate from the solution. Because of the connectivity between the blocks, this results in a “local microphase separation”; i.e., the less solvated blocks of multiple chains aggregate together and form the core of a micelle, whereas the other, more soluble blocks form the micelle’s corona and keep the self-assembled, finite-sized aggregate in solution. Depending on the volume ratio of the two blocks, micelles may adopt different shapes, which can be spherical, worm-like cylindrical, or lamellar vesicles. A way to form such self-assembled structures in solution is to slowly replace a good solvent for the different blocks by a very selective solvent, which is even a nonsolvent for one of the blocks. This can be achieved by dialysis of a block copolymer in a good solvent against a nonsolvent.¹¹⁶

If these self-assembled aggregates form a disordered solution, this micellar fluid is thermodynamically considered as a single, disordered phase. Upon an increase of the micellar density, the micellar system can transform into an ordered phase, where the different micellar aggregates are separated from each other by the steric repulsion of the swollen outer blocks and condense onto a crystal lattice.

The removal of the solvent from a block copolymer solution will lead to bulk structures, which would be independent of the initially chosen solvent, if thermodynamic equilibrium was achieved. Long chain molecules, however, do not rapidly equilibrate and can be trapped in different nonequilibrium states because of large single-chain relaxation times, e.g., associated with the exchange of block copolymers between aggregates and significant collective free-energy barriers that must be overcome by thermal fluctuations for larger structural rearrangements. Solvent exchange in triblock terpolymers was used to generate a large variety of aggregated structures,¹¹⁷ which also can form supramolecular polymers.¹¹⁸ Examples of nonequilibrium structures are hexagonally perforated lamellae in diblock copolymers, which irreversibly transform into a double-gyroid structure upon thermal annealing¹¹⁹ or the “knitting pattern” structure, found in a triblock terpolymer, where the middle block shows a poor solubility and the other blocks exhibit a good solubility in one solvent, while in another solvent all blocks show a comparable solubility, resulting in a lamellar structure after solvent evaporation.¹²⁰ In the following, we mostly restrict the

discussion to diblock copolymers, as block copolymers with more blocks or consisting of more than two types of monomers will significantly increase the complexity.⁸⁶

The structure formation in block copolymer membranes not only involves the macrophase coexistence between polymer, solvent, and nonsolvent but additionally the microphase separation between the two components—A and B—of the block copolymer into a spatially modulated structure, whose length scale is set by the molecular extension, R_e , of the macromolecule. In order to describe this microphase separation, an additional order parameter is required, $\varphi = \phi_A/\phi_P$ with ϕ_A and $\phi_P = \phi_A + \phi_B$ denoting the density of polymer block A and the total polymer density, respectively.

Since this microphase separation occurs on smaller length and time scales than the macrophase separation between polymer and nonsolvent, discussed in the previous subsection, a first, crude approximation consists of decoupling the fast microphase separation and the slow macrophase separation. To this end, one replaces the homogeneous polymer domain of the previous subsection by a spatially structured one. Self-assembly or microphase separation will occur, if the thermodynamic incompatibility between the blocks of the copolymer, quantified by the interaction parameter $\chi_{AB}N$, is sufficiently large. Note that the effective incompatibility between the blocks is modulated by the presence of a common solvent, similar to eqs 2 or 3. Thus, self-assembly or microphase separation can be induced by temperature jumps, solvent evaporation, or solvent–nonsolvent exchange. The latter two processes reduce the solvent density, ϕ_S .

If the block copolymer density, ϕ_P , is small, the block copolymer will aggregate into micelles (as described above). Note that in case of slow solvent evaporation from a polymer film or slow solvent–nonsolvent exchange in NIPS, the initial self-assembly into micelles is quite expected, although theoretical approaches often consider only the structure formation at high polymer density starting from a homogeneous distribution of the two components, A and B.

At higher block copolymer densities, periodic microphases will form. For a pure, symmetric diblock copolymer, the mean-field prediction of the order–disorder transition (ODT) is $\chi_{AB}N \approx 10.5$.⁸⁵ A solvent, ϕ_S , dilutes the effective thermodynamic repulsion between A and B species, cf., eq 2. In the microphase-separated state, additionally, the solvent will preferentially be enriched at the internal AB interfaces in order to mitigate the unfavorable interactions between A and B segments.¹¹⁰ Moreover, the solvent tends to swell the characteristic periodicity of the spatially modulated structure. This swelling may affect the different domains of the block copolymer to a different extent because (i) the solvent has a preference to one of the two domains, or (ii) the stretching of a distinct block in an asymmetric copolymer is affected differently by the incorporation of solvent. Thus, the volume fraction of the A domain depends on the solvent density, and a variation of the solvent density may induce an order–order transition between spatially modulated phases with different symmetries.^{121,122}

Self-consistent field theory (SCFT) provides a quantitative description of micellar self-assembly and microphase separation in melts at the mean-field level.^{123–132} Qualitatively, the periodic, spatially modulated structure arises from a balance between the free-energy costs of the internal AB interfaces that favor large domains and the stretching of the macromolecular conformations as they fill space uniformly. This approach has been successfully applied to study the phase behavior as a

function of solvent density and selectivity,^{110,121,122} copolymer composition,^{126,133} and copolymer architecture.¹³⁴

In the ultimate vicinity of the ODT, the amplitude of φ -variations in a pure diblock copolymer melt is small, and the free energy of a system, characterized by a spatially varying $\varphi(r)$, is given by the random-phase approximation (RPA).⁸⁵ To lowest order, the free energy as a function of the Fourier transform of $\varphi(r)$ takes the quadratic form

$$\frac{F}{\rho V k_B T / N} = \frac{1}{2} \sum_{\mathbf{q} \neq 0} \left(\frac{N}{S_{\mathbf{q}}^{(0)}} - 2\chi_{AB}N \right) |\varphi_{\mathbf{q}}|^2$$

$$\text{with } S_{\mathbf{q}}^{(0)} = \frac{S_{AA,\mathbf{q}}^{(0)} S_{BB,\mathbf{q}}^{(0)} - (S_{AB,\mathbf{q}}^{(0)})^2}{S_{AA,\mathbf{q}}^{(0)} + 2S_{AB,\mathbf{q}}^{(0)} + S_{BB,\mathbf{q}}^{(0)}} \quad (7)$$

where $S_{\alpha\beta,\mathbf{q}}^{(0)}$ denote the single-chain structure factors of the blocks α and β in the disordered melt. The spinodal stability limit of the spatially homogeneous state is marked by the condition $\chi_{AB}^{\text{spin}} = \min_{\mathbf{q}} \frac{1}{2S_{\mathbf{q}}^{(0)}}$. In order to describe microphase separation, third- and fourth-order terms have to be included. RPA provides a systematic way of calculating the coefficients of these terms from the single-chain properties in the disordered phase.⁸⁵ This expansion is valid in the ultimate vicinity of the ODT, but, unfortunately, it already fails to provide a quantitative description for $\chi_{AB}N > 13$. Treating the expansion coefficients as phenomenological parameters and adjusting them to match the periodicity, the scale of the free energy, and the range of the A density, one can significantly expand the range of application.^{135,136}

In the strong-segregation limit, in turn, the free energy can be quantified by the Ohta–Kawasaki free-energy functional¹³⁷

$$\frac{\mathcal{F}_{\text{OK}}[\varphi]}{\rho k_B T / N}$$

$$\approx \int d\mathbf{r} \left(\frac{1}{2} \varphi \left\{ -\Delta - 1 + \tilde{\alpha} \int d\mathbf{r}' G(\mathbf{r}, \mathbf{r}') \right\} \varphi + \frac{\tilde{\gamma}}{3} \varphi^3 + \frac{1}{4} \varphi^4 \right)$$

$$= \int d\mathbf{r} \left(-\frac{1}{2} \varphi^2 + \frac{\tilde{\gamma}}{3} \varphi^3 + \frac{1}{4} \varphi^4 + \frac{1}{2} [\nabla \varphi]^2 \right)$$

$$+ \frac{\tilde{\alpha}}{2} \iint d\mathbf{r} d\mathbf{r}' \varphi(\mathbf{r}) G(\mathbf{r}, \mathbf{r}') \varphi(\mathbf{r}') \quad (8)$$

where the long-range kernel, $G(r, r')$, obeys the Poisson equation

$$-\Delta G(\mathbf{r}, \mathbf{r}') = \delta(\mathbf{r} - \mathbf{r}') + \text{const} \quad (9)$$

and the periodicity as well as the scales of the free energy and of the A density have been rescaled. This Ohta–Kawasaki free-energy functional captures the asymptotic wavevector dependence of the collective structure factor for $q \rightarrow 0$ and $q \rightarrow \infty$ and is also appropriate for $\chi_{AB}N \gg 1$.¹³⁷

Uneyama and Doi have adopted this approach to copolymer–solvent mixtures.¹³⁸ Their generalization of the free-energy functional, eq 8, can describe both macrophase separation between polymer, solvent, and nonsolvent as well as microphase separation between the blocks of the copolymer. An alternative form of a free-energy functional for amphiphilic solutions is given in ref 139.

4. HOMOPOLYMER MEMBRANES

4.1. Phase-Inversion Membranes

As mentioned in the introduction, NIPS is a common strategy to produce membranes with a thin selective top layer on a more open, porous substructure. The process is illustrated by the time evolution of the densities of the different components, schematically depicted in Figure 2. After some evaporation

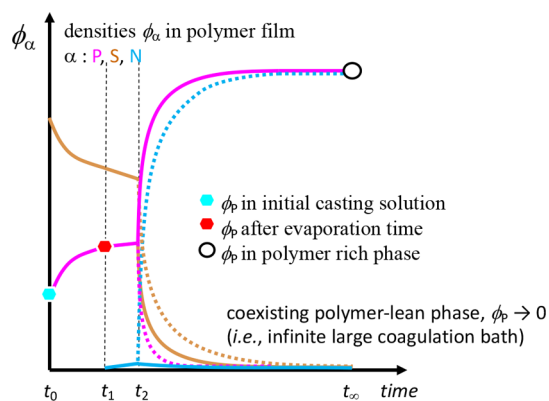


Figure 2. Sketch of the time evolution of the averaged densities, ϕ_{α} , in an incompressible ternary system, composed of polymer P, solvent S, and nonsolvent N. The density of the polymer in the initially cast, solvent-swollen polymer film at t_0 is marked with a cyan hexagon. Until t_1 , the solvent evaporates, and the polymer density increases. At t_1 , the solution is immersed into an infinitely large nonsolvent (coagulant) bath, and phase separation into a polymer-rich and a polymer-lean phase occurs within the film after sufficient penetration of nonsolvent into the film at t_2 . If the polymer-rich phase was not kinetically trapped, phase separation would proceed until equilibrium, t_{∞} .

time, t_1 , the solvent-swollen polymer film is immersed into an infinitely large nonsolvent reservoir—the coagulation bath. In Figure 2, we have assumed that the density of polymer and solvent in the coagulation bath is vanishingly small. The nonsolvent reservoir withdraws the solvent from the polymer film, whereas only a smaller amount of nonsolvent diffuses into the polymer film. In response to this solvent–nonsolvent exchange across the film surface, the densities in the polymer film continuously change. If the nonsolvent density becomes high enough, the polymer will begin to precipitate at time t_2 , into a polymer-rich phase (solid lines in Figure 2) that coexists with a polymer-lean phase (dotted lines, mainly composed of nonsolvent). The spatial average densities, however, cannot reveal that the plane where the polymer solution starts to phase separate—the phase-separation front—moves from the film surface toward the substrate.

Depending on the initial densities and the rate of the solvent–nonsolvent exchange, the phase separation occurs via spinodal decomposition—in particular, if the system enters the miscibility gap in the vicinity of the critical point—or a nucleation-and-growth mechanism. Not only does the position of the phase-separation front vary with time, but also the profile changes with time. These spatiotemporal changes may potentially alter the mechanism of phase separation or, in the case of spinodal decomposition, the characteristic length scale of density variations in the early stage of phase separation, resulting in an integral-asymmetric structure.

In order to stabilize such an integral-asymmetric structure, phase separation and coarsening must be dynamically arrested. Such a dynamic arrest in the polymer-rich phase can occur, e.g.,

by a glass transition or crystallization at sufficiently increased polymer density.

Using this NIPS approach, Loeb and Sourirajan²⁵ were the first to develop an integral-asymmetric membrane. It was a cellulose acetate membrane for reverse osmosis that displayed a good salt rejection combined with high flux. A lot of work has been carried out since then on integral-asymmetric membranes from many polymers. These membranes display a rather dense (and thus selective) surface layer on top of a more open, porous (and thus less resistive) substructure. The substructure can be spongy or display finger-like macrovoids. Also a combination of these structural features can occur. The substructure is relevant for the final membrane properties because it also influences the mechanical properties and thus the membrane stability with respect to applied transmembrane pressure in operation conditions. Many experimental studies have been carried out in order to obtain more insight into the processes that lead to different cross-sectional structures and the relevant parameters. Macrovoid formation has been a topic of debate for several decades. Strathmann et al. presented experimental data on polyamide membranes, which were prepared by casting a polyamide solution film into a mixture of the solvent with water (nonsolvent).¹⁴⁰ In this way, the effective incompatibility between polymer and precipitant was varied, and the resulting membranes showed macrovoids when precipitated in pure water and a sponge structure in water mixed with 75% of solvent. The formation of macrovoids was explained by the fast precipitation of a polymer-rich skin layer at the film surface in case of a strongly incompatible precipitant (in this case, pure water) and the concomitant mechanical stresses in this top layer, which lead to defects at the surface. Across these defects, a fast penetration of precipitant into the polymer film occurs, resulting in finger-like macrovoids. In the case of a weak precipitant, in contrast, phase separation occurs slower; i.e., the phase-separation front slowly moves across the polymer film, resulting in a cocontinuous sponge structure. The similar effect of creating or suppressing macrovoids can be achieved by adding an appropriate cononsolvent to the casting solution, in order to decrease the effective solvent quality for the polymer. While in the absence of the cononsolvent, macrovoids are formed, their formation is suppressed in the presence of a cononsolvent in the casting solution by reducing the thermodynamic gradient between the one-phase casting solution and coagulant.¹⁴¹

Smolder et al. also explained the occurrence of macrovoids as a result of instantaneous demixing at the surface of the cast film after immersion into a precipitation bath, which occurs unless the polymer density in the casting solution is too large, or the casting solution is already close to precipitation due to the presence of a cononsolvent.¹⁴² In these latter cases, no macrovoids are generated. According to their reasoning, macrovoids are not a result of a mechanical weakness in the top layer but are generated by formed nuclei of the polymer-lean phase right underneath the surface and grow by diffusive transport.

While in this work the authors excluded viscosity as a parameter that could be important for the formation of macrovoids, the viscosity or viscoelasticity of the casting solution is discussed as an important property in the work of Hung et al.⁸³ Especially entanglements of the polymer chains are considered to be relevant. The number of entanglements increases with polymer density, making the solution more viscoelastic, which hinders the formation of macrovoids. In a more diluted or better dissolved state, in turn, the viscosity is

smaller, and macrovoids can form more easily, cf., Figure 3. This work agrees with the previous ones by stating that the macrovoid

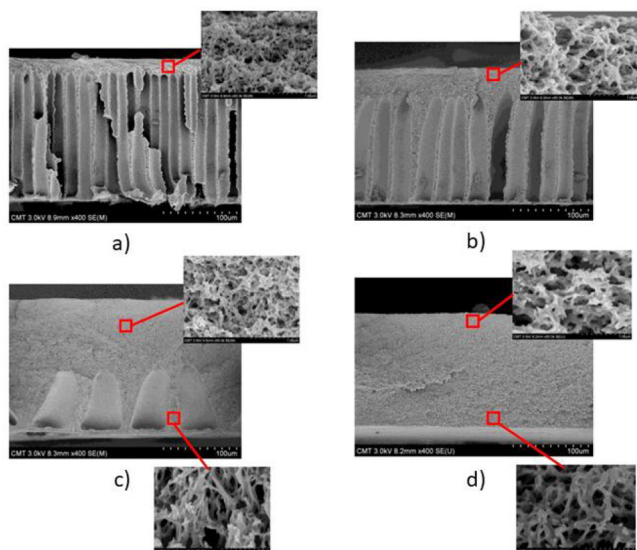


Figure 3. Cross-sections of membranes cast from solutions of polysulfone and precipitated in water. The polymer densities are 12% (a, c) and 18% (b, d). The solvent is 2-methylpyrrolidinone (a, c) and 2-methylpyrrolidinone with 0.5 wt % water (b, d). Comparison of (a) with (c) and (b) with (d) shows the influence of polymer density, while comparison of (a) with (b) and (c) with (d) illustrates the influence of the solvent quality, as the addition of water decreases the solubility of the polymer. Increasing the polymer density leads to an increase of the distance, L , between membrane surface and onset of macrovoids. Adapted with permission from ref 83. Copyright 2016 Elsevier.

formation is suppressed at locations where instantaneous phase separation occurs when the polymer solution gets into contact with the coagulant; however, it also explains the formation of macrovoids at some distance, ΔL , below the film surface. In these locations, the polymer is still well dissolved, and the chains can still relax in the homogeneous phase, while the miscibility decreases by a sufficiently slowly increasing coagulant density. Macrovoids form in these less entangled regions, where the relaxation time of the chains is shorter than the time scale to initiate phase separation. This time scale of initiating phase separation is characterized by the moving speed of the phase-separation front across the membrane during phase inversion.

This work also suggested two master curves: The observed distance, ΔL , between the membrane surface and the onset of macrovoids is related to polymer density or viscosity via

$$\frac{\Delta L^2}{D_e} \approx 0.2s \left(\frac{\phi}{\phi_e} \right)^{6.8} \quad \text{or} \quad \frac{\Delta L^2}{D_e} \approx 0.5s \frac{\eta}{\eta_e} \quad (10)$$

where D_e denotes the collective diffusivity of coagulant transport, and ϕ and ϕ_e stand for the polymer density in the casting solution and the entanglement density, respectively (see Figure 4). Moreover, the experimental data also correlate linearly with the viscosity, η , of the casting solution, when normalized by the viscosity, η_e , at which the influence of entanglements starts to become visible.

4.2. Scope and Goals of Modeling

Modeling and simulation of membrane formation aims at understanding and predicting the salient features of the

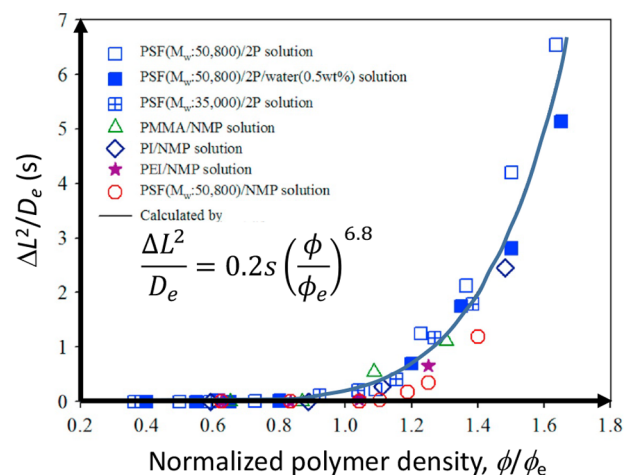


Figure 4. Master plot of the ratio between the squared distance, ΔL^2 , and the effective diffusivity, D_e , of the transport of coagulant, as a function of the polymer density, ϕ , in the casting solution normalized by the entanglement density, ϕ_e . Adapted with permission from ref 83. Copyright 2016 Elsevier.

formation process, and different levels of abstraction have been employed. In addition to the bulk equilibrium thermodynamics, the different modeling approaches address (i) the role of spatial inhomogeneities such as the surface of the solvent-swollen polymer film in contact with a nonsolvent and (ii) the kinetics of phase separation, as well as (iii) the arrest of the structure formation by vitrification, crystallization, or gelation. There is a complex interplay between these different ingredients that makes modeling membrane formation a challenge. In this section, we will discuss the different modeling approaches and highlight their scope and insights, chiefly focusing on the NIPS process for homopolymer membranes. Copolymer membranes will be discussed in the following section, chiefly placing emphasis on experiments.

Membrane formation involves a variety of thermodynamic phenomena—e.g., macrophase separation between polymer and nonsolvent, microphase separation inside the copolymer-rich domains, crystallization—and kinetic processes—such as diffusive or hydrodynamic transport, surface-directed spinodal structure formation vs. nucleation phenomena, or intrinsically slow exchange of molecules between copolymer micelles—that operate on different time and length scales. For instance, the strength of incompatibility between polymer and nonsolvent or between the segment species of a copolymer is dictated by atomic-scale interactions. These properties on the atomic scale determine the phase behavior (e.g., via the Flory–Huggins miscibility parameter), the properties of surfaces and interfaces (e.g., via the range of interactions and the statistical segment length), as well as the segmental friction (e.g., via fluid-like packing). The length scale and geometry of microphase separation or dynamic properties such as viscosity or viscoelasticity due to entanglements are influenced by characteristics on the scale of the macromolecule. The large-scale morphology, such as e.g., property gradients in asymmetric membranes, in turn, involve even larger scales of length and time, i.e., multiple micrometers and seconds.

Because of the challenges above, there exists no single, overarching model of membrane formation; instead, different modeling strategies are required. Each model provides a rather accurate description of a particular vignette of the overall process, and significant progress has been achieved in specific

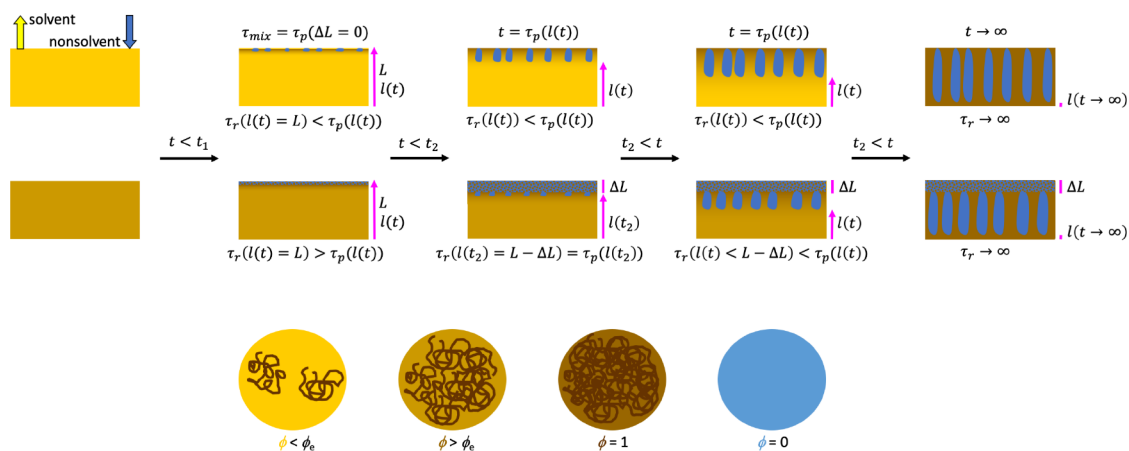


Figure 5. Illustration of the formation of macrovoids in the course of NIPS as a function of the polymer density, ϕ , in the polymer solution. When coagulating a polymer solution with a density below ϕ_e (top row), the chains with relaxation time, τ_r , are fully relaxed when phase separation starts at τ_p , and macrovoids form at the top of the film at a time, t_1 . If the polymer density is above ϕ_e (bottom row), however, phase separation starts before the chains are relaxed (disentangled). Thus, no macrovoids are initially formed, but a rather dense network structure is built up by spinodal decomposition. The distance, ΔL , between film surface and macrovoid formation increases with a higher polymer density and a with higher collective diffusivity of the coagulant, D_e . The scaling relation, eq 10, is applicable to a variety of polymer–solvent–nonsolvent systems. Inspired by a similar drawing in ref 83.

aspects. The systematic coupling of descriptions that address properties on different scales, however, remains a challenge. In the following section, we review this progress by introducing a selection of models that have been used to investigate membrane formation, focusing on continuum models and coarse-grained particle models.

To set the stage, we consider two prototypical processes:

- Solvent evaporation (dry-casting) or evaporation-induced self-assembly (EISA)—a solvent evaporates from a solvent-swollen polymer or copolymer film into air (nonsolvent), and the film thickness, h , decreases in turn. As the solvent evaporates into the vapor phase, the local polymer density increases and potentially gives rise to the formation of a dense polymer layer (skin) at the film surface,^{143–147} resulting in a density gradient across the film. Additionally, because of the local change in composition, the polymer–solvent mixture may enter the miscibility gap and phase separate. In the case of a copolymer film, the copolymer may form micelles in the solvent-rich interior of the film or microphase separate in the regions of high polymer density.
- Nonsolvent-induced phase separation (NIPS)—a mixed film of polymer and solvent is brought into contact with a nonsolvent bath (coagulation bath). Solvent and nonsolvent are exchanged across the surface between polymer film and coagulation bath. Typically, the solvent leaves the film faster than the nonsolvent enters the film in turn. Thus, the film thickness, h , shrinks. The interplay between the thermodynamics of the ternary mixtures, the dynamic asymmetry of the constituents, and the kinetics of solvent and nonsolvent transport across the film surface may, however, give rise to a complex time evolution of the film thickness, $h(t)$.¹⁴⁸ As the nonsolvent enters the film via the film surface, the ternary mixture inside the film becomes unstable, and macrophase separation commences. If the polymer is a copolymer, additionally, microphase separation will occur inside the polymer-rich domains.

From the modeling perspective, these two processes share many common features. Both solvent evaporation as well as

NIPS consider the kinetics of phase separation of a ternary system of polymer, solvent, and nonsolvent. In the case of solvent evaporation, however, (i) the nonsolvent (air) typically does not enter the film, (ii) the nonsolvent can often be described by a simple ideal-gas equation of state, and (iii) polymer and solvent must not be completely miscible to allow for phase separation inside the film.

As an example of the complexity found in the morphology of homopolymer membranes prepared by NIPS, the cross-section of a homopolymer membrane is schematically presented in Figure 5 at different times during the formation and for different polymer densities.⁸³ This work studied the formation of a spongy or macrovoid substructure and found that entanglements of high-molecular-weight polymers, occurring at larger polymer densities, suppress macrovoid formation. Macrovoid structures, however, are formed at lower densities; see Figure 3. Decreasing the solvent quality results in a faster occurrence of phase separation during the NIPS process, favoring a sponge-like phase-separated structure, and suppresses macrovoid formation, as can be seen by comparing the different panels in Figure 3. The scaling relation, eq 10, indicates that the distance between the membrane surface and the onset of macrovoid formation, ΔL , is a function of the collective diffusivity, D_e , of the nonsolvent and the polymer density, ϕ_p .⁸³

Additionally, alternate kinetic processes, e.g., adsorption^{149,150} or wetting^{151–153} phenomena due to the preferential interactions with the supporting substrate or the film surface, or polymerization-induced phase separation (PIPS),^{72,154,155} as well as the role of additives such as, e.g., nanoparticles or inorganic building blocks,^{156–159} give rise to additional effects that are, however, not considered in the following.

The aim of this section is rather to provide a tutorial description of the basic modeling approaches that provide a starting point for addressing specific applications. The goal of theory and simulation is to investigate and understand the role of the different factors that influence membrane formation, such as physicochemical properties of polymer, solvent, and nonsolvent, and the processing conditions, such as initial composition of the solvent-swollen polymer film and coagulation bath or the dynamic asymmetry of the components. Within a modeling framework, these different thermodynamic and kinetic proper-

ties are simultaneously accessible and can be varied systematically and independently. Thereby, modeling and simulation contribute to disentangling their roles. Additionally, simulations provide insights into the ordering kinetics with high spatial and temporal resolution that might be difficult to obtain by experiments. This holds true *a fortiori* in the course of the early stages of phase separation that template the structure that emerges at later times.

4.3. Continuum Models

4.3.1. General Considerations. The basic bulk thermodynamics has already been introduced in the section, clarifying the different equilibrium structures, e.g., macrophase separation between polymer and nonsolvent, and microphase separation of the distinct components of the block copolymer in polymer-rich domains—and the concomitant order parameters—density profiles, and spatial modulation of the AB composition.

In order to describe membrane formation, however, three additional aspects need to be addressed: (i) spatial inhomogeneities, (ii) mass transport into and out of the solvent-swollen polymer film, and (iii) phase separation with dynamic asymmetry. The distinct aspects can already be captured by continuum models, which make direct contact to the equilibrium phase behavior. Correlating these effects with molecular properties of the constituents, however, requires a more microscopic description.

4.3.2. Free-Energy Functional for Spatially Inhomogeneous Systems. The aim of continuum models is a description of the thermodynamics of a spatially inhomogeneous system and the concomitant kinetics of structure formation. To this end, the system configuration is described by spatially varying density fields of the polymer, ϕ_P , solvent, ϕ_S , and nonsolvent, ϕ_N .

Often the system can be treated as locally incompressible

$$\phi_P(\mathbf{r}) + \phi_S(\mathbf{r}) + \phi_N(\mathbf{r}) = 1 \text{ for all points in space} \quad (11)$$

Then, two density fields, e.g., $\phi_S(r)$ and $\phi_N(r)$, suffice to completely specify the system configuration. In the case of an AB diblock copolymer, the local composition, $\varphi(r)$, that quantifies the local ratio of the A density to the density A and B segments of the copolymer is additionally required.

In order to incorporate the free-energy costs of spatial inhomogeneities, one can supplement the free energy of a spatially homogeneous system, $F(\phi_P, \phi_S, \phi_N)$, see eq 5 or eq 6, by gradient terms. Often, one only considers the lowest-order terms permitted by symmetry, i.e., square-gradient theories, that also allow for an analytic calculation of the surface tension¹⁶⁰ or the wetting behavior.¹⁵¹ An example of the generalization of the free-energy function, eq 5, to a free-energy functional takes the following form.^c

$$\frac{\mathcal{F}[\phi_P(\mathbf{r}), \phi_S(\mathbf{r}), \phi_N(\mathbf{r})]}{k_B T} = \rho \int d\mathbf{r} \left\{ \frac{F(\phi_P, \phi_S, \phi_N)}{\rho V k_B T} + \frac{b^2}{2} \sum_{\alpha, \beta = P, S, N} c_{\alpha\beta} \nabla \phi_\alpha \nabla \phi_\beta \right\} \quad (12)$$

The coefficients, $c_{\alpha\beta}$ where the Greek indices run over all components, polymer, solvent, and nonsolvent, form a symmetric, positive matrix and can be functions of the densities. b is a length scale that characterizes the width of the interfaces. Such a low-order gradient theory can be systematically derived by a perturbation expansion around a spatially homogeneous

system (RPA)¹⁶¹ or from strong-segregation theory.¹⁶² b is on the order of the statistical segment length of the polymer or the range of nonbonded interactions between the constituents. Like eq 6, however, the range of application is significantly larger if the coefficients, $c_{\alpha\beta}$, are treated as phenomenological model parameters. Such a square-gradient theory provides a basic, qualitative model of the thermodynamics of spatially inhomogeneous polymer–solvent–nonsolvent mixtures. A more accurate description of spatial inhomogeneities is provided by SCFT^{123–132} or polymer density functional theory (DFT).^{163–168} [In DFT, the order parameter is the distribution function of single-molecule conformations rather than the collective density of segment species.] These more microscopic approaches can be employed to parametrize continuum models. They can also be extended to study the dynamics of structure formation, but they are computationally much more demanding and have not yet been applied to NIPS.

The planar, supporting substrate interacts with the constituents of the polymer film, giving rise to an additional contribution to the free energy¹⁵¹

$$\frac{\Delta \mathcal{F}_w}{\rho A k_B T} = - \int dz \delta(z) \left\{ \sum_{\alpha} \mu_{w\alpha} \phi_{\alpha} + \frac{1}{2} \sum_{\alpha\beta} \chi_{w\alpha\beta} \phi_{\alpha} \phi_{\beta} \right\} \quad (13)$$

where A stands for the substrate area. In this limit of zero-range (contact) interaction with the substrate, only the densities at the substrate position, $z = 0$, matter. $\mu_{w\alpha}$ characterizes the attraction of the substrate for the species α , whereas $\chi_{w\alpha\beta}$ denotes the modification of the pairwise interaction between species α and β due to the presence of the wall (“missing neighbor” effect). The short-range interactions between the ternary mixture and the substrate can be complemented by long-range van-der-Waals interactions. Polymer-DFT^{163–168} will provide a more accurate description, including the layering at the substrate.

Such a free-energy functional, $\mathcal{F}[\phi_P, \phi_S, \phi_N]$, associates with each spatially varying density distribution, $\phi_P(r)$, $\phi_S(r)$, and $\phi_N(r)$, a free energy. The value of the free energy depends on the thermodynamic state point via the coefficients in the bulk free-energy density and in front of the square-gradient terms, cf., eq 12, or the parameters of the substrate free energy, eq 13.

The equilibrium density distribution is obtained by minimizing the grand-canonical free-energy functional, \mathcal{G} , for a given thermodynamic state characterized by temperature, T , volume, V , and chemical potentials, $\mu_{\alpha}^{(0)}$, of the different species, α

$$\mathcal{G} = \mathcal{F} - \sum_{\alpha = P, S, N} \mu_{\alpha}^{(0)} \int d\mathbf{r} \rho \phi_{\alpha}(\mathbf{r}) \quad (14)$$

Minimizing the free-energy functional, \mathcal{G} , one obtains the equilibrium density distribution, i.e.,

$$\frac{\delta \mathcal{G}}{\rho \delta \phi_{\alpha}(\mathbf{r})} = \frac{\delta \mathcal{F}}{\rho \delta \phi_{\alpha}(\mathbf{r})} - \mu_{\alpha}^{(0)} = 0 \text{ for } \alpha = P, S, N \quad (15)$$

This condition in conjunction with appropriate boundary conditions yields bulk phase equilibria and the profile across the interface between the coexisting phases. The substrate contribution to the free energy, eq 13, does not alter eq 14 but provides a boundary condition.^{151,169}

$$-b^2 \sum_{\beta} c_{\alpha\beta} \frac{\partial \phi_{\alpha}}{\partial z} \Big|_{z=0} = \mu_{w\alpha} + \sum_{\beta} \chi_{w\alpha\beta} \phi_{\beta}(0) \quad (16)$$

Often, equilibrium is achieved when the solvent density, ϕ_s is vanishingly small in the polymer film and the nonsolvent bath, and the system can be approximated by an incompressible, binary mixture of polymer and nonsolvent. In this limit, the profile of the interface between the coexisting polymer-rich and nonsolvent-rich phases as well as the profile at the substrate can be graphically obtained by the Cahn construction.¹⁵¹

In a nonequilibrium situation, we define the local chemical potential

$$\mu_{\alpha}(\mathbf{r}) \equiv \frac{\delta \mathcal{F}}{\rho \delta \phi_{\alpha}(\mathbf{r})} \quad (17)$$

Equation 15 asserts that this local chemical potential is constant and equals the thermodynamic chemical potential in equilibrium. Out of equilibrium, a gradient of this chemical potential acts as a thermodynamic driving force for the kinetics of structure formation. Several dynamic continuum models have been developed to describe the kinetics of structure formation and phase separation that is driven by gradients of the chemical potential. Here we introduce the most common models but refer the reader for treatments of more complex processes to the literature.^{170,171} The goal of studying the kinetics of structure formation in the framework of continuum models consists of (qualitatively) exploring the role of thermodynamic and kinetic parameters, such as the virial coefficients, self-diffusion coefficients, and viscoelasticity, and providing insights into the general mechanisms of nonequilibrium processes in polymer membrane formation.

4.3.2.1. Model B. In order to describe the mass transport across the film surface and the phase separation, a description of the kinetics of the collective density is required. A classification of kinetic equations for phase separation has been provided by Hohenberg and Halperin¹⁷² on the basis of the type of order parameter that distinguishes the coexisting phases and the conserved quantities in the course of structure formation. In the continuum model, the local scalar densities are the order parameters that are locally conserved and obey continuity equations.

$$\frac{\partial \phi_{\alpha}(\mathbf{r}, t)}{\partial t} + \nabla \cdot \mathbf{j}_{\alpha} = 0 \quad (18)$$

Linear response theory provides a relation between the currents, $\mathbf{j}_{\alpha} = \phi_{\alpha} \mathbf{u}_{\alpha}$, where \mathbf{u}_{α} denotes the velocity of species α , and the thermodynamic driving forces, $\nabla \mu_{\beta}$.

$$\mathbf{j}_{\alpha}(\mathbf{r}) = - \sum_{\beta} \Lambda_{\alpha\beta} \nabla \mu_{\beta} \quad (19)$$

where the matrix $\Lambda_{\beta\alpha}$ is positive-definite and symmetric due to Onsager's reciprocal relations. In the simplest case, the Onsager coefficient, $\Lambda_{\alpha\alpha} \sim D_{\alpha} \phi_{\alpha}$ is taken to be proportional to the product of self-diffusion coefficient, D_{α} of species α and its density, so that one recovers the diffusion equation for an ideal gas. The Onsager coefficient, $\Lambda_{\alpha\alpha}$ has to vanish for $\phi_{\alpha} \rightarrow 0$ because there cannot exist a flux of species α without its presence. The Onsager coefficient establishes a quantitative relation between the single-chain dynamics and the kinetics of the collective density—this is how the underlying molecular motion enters the continuum description. For instance, using the dependence of the self-diffusion coefficient, D_{α} on the local

densities, one can account for the slowing down of the polymers at high densities, i.e., vitrification, that results in the arrest of structure formation.¹⁴⁶ More generally, the Onsager coefficients can be nonlocal in space and time such that eq 19 generalizes to^{173–175}

$$\mathbf{j}_{\alpha}(\mathbf{r}, t) = - \int_{-\infty}^t dt' \int d\mathbf{r}' \sum_{\beta} \{ \Lambda_{\alpha\beta}(\mathbf{r} - \mathbf{r}', t - t') \nabla' \mu_{\beta}(\mathbf{r}', t') \} \quad (20)$$

Such nonlocalities can be obtained by the dynamic random-phase approximation (D-RPA)^{173,176–178} and are particularly important on length scales comparable to the polymer extension, R_{α} , and time scales of the polymer relaxation time, τ_{α} .

By virtue of the incompressibility constraint, eq 11, there are only two independent densities and only two independent chemical potentials for a three-component system. Moreover, all fluxes have to cancel at each point in space for all times. In order to enforce incompressibility, one incorporates the constraint into the free-energy functional, eq 12, via a pressure-like Lagrange field, $\Pi(\mathbf{r})$ ¹⁷⁹

$$\mathcal{F}' = \mathcal{F}[\phi_p, \phi_s, \phi_N] + \rho \int d\mathbf{r} \Pi(\mathbf{r}) \{ \phi_p(\mathbf{r}) + \phi_s(\mathbf{r}) + \phi_N(\mathbf{r}) - 1 \} \quad (21)$$

where $\Pi(\mathbf{r})$ is chosen as to enforce incompressibility. The additional term in \mathcal{F}' yields an additive contribution to all chemical potentials

$$\mu'_{\alpha}(\mathbf{r}) \equiv \frac{\delta \mathcal{F}'}{\rho \delta \phi_{\alpha}(\mathbf{r})} = \mu_{\alpha}(\mathbf{r}) + \Pi(\mathbf{r}) \quad (22)$$

The condition that all fluxes have to cancel at each point in space, $\sum_{\alpha} \mathbf{j}_{\alpha}' = 0$, in conjunction with eq 19 determines the gradient of the pressure-like field.

$$\nabla \Pi = - \frac{\sum_{\alpha\beta} \Lambda_{\alpha\beta} \nabla \mu_{\beta}}{\sum_{\alpha\beta} \Lambda_{\alpha\beta}} \quad (23)$$

Thus, the model B dynamics of the incompressible system takes the form

$$-\frac{\partial \phi_{\alpha}(\mathbf{r})}{\partial t} = \nabla \cdot \mathbf{j}'_{\alpha} = \nabla \cdot \left\{ \sum_{\beta} \Lambda_{\alpha\beta} \left(\nabla \mu_{\beta} - \frac{\sum_{\gamma\delta} \Lambda_{\gamma\delta} \nabla \mu_{\delta}}{\sum_{\gamma\delta} \Lambda_{\gamma\delta}} \right) \right\} \quad (24)$$

$$= \nabla \cdot \left\{ \frac{\sum_{\beta\gamma\delta} \Lambda_{\alpha\beta} \Lambda_{\gamma\delta} \nabla (\mu_{\beta} - \mu_{\delta})}{\sum_{\gamma\delta} \Lambda_{\gamma\delta}} \right\} \quad (25)$$

$$= \nabla \cdot \left\{ \frac{(\Lambda_{\alpha\alpha} \sum_{\gamma \neq \alpha} \Lambda_{\gamma\gamma}) \nabla \mu_{\alpha} - \Lambda_{\alpha\alpha} \sum_{\gamma \neq \alpha} \Lambda_{\gamma\gamma} \nabla \mu_{\gamma}}{\sum_{\gamma} \Lambda_{\gamma\gamma}} \right\} \quad (26)$$

if $\Lambda_{\alpha\beta} = 0$ for $\alpha \neq \beta$

where, in the last equation, we have assumed that $\Lambda_{\alpha\beta}$ is diagonal. Only two of these kinetic equations for ϕ_{α} are independent.

In the presence of a barycentric, ϕ_{α} -averaged velocity field, $\mathbf{u} = \sum_{\alpha} \phi_{\alpha} \mathbf{u}_{\alpha}$ with \mathbf{u}_{α} being the velocity of species α or a moving reference frame, the mass balance equation takes the form

$$\begin{aligned} \frac{\partial \phi_\alpha}{\partial t} + \nabla(\phi_\alpha \mathbf{u}_\alpha) &= \frac{\partial \phi_\alpha}{\partial t} + \nabla(\phi_\alpha \mathbf{u}) + \nabla \mathbf{j}'_\alpha \\ &= \frac{D \phi_\alpha}{Dt} + \nabla \mathbf{j}'_\alpha = 0 \end{aligned} \quad (27)$$

with the material derivative $\frac{D}{Dt} = \frac{\partial}{\partial t} + \mathbf{u} \cdot \nabla$. Here $\mathbf{j}'_\alpha \equiv \phi_\alpha(\mathbf{u}_\alpha - \mathbf{u})$ denotes the flux of species α relative to the ϕ_α -averaged \mathbf{u} , and $\sum_\alpha \mathbf{j}'_\alpha = 0$. An incompressible system is described by $\nabla \cdot \mathbf{u} = 0$. Such a formulation is useful to employ to a reference frame, where the nonvolatile polymer component is at rest, $\mathbf{u}_p = 0$,⁹⁴ or to study the effect of a control-parameter front propagating with velocity, \mathbf{u} , through the system.^{180–182} The formulation is also the basis to include hydrodynamics (*vide infra*).¹⁸³

A one-dimensional description allows one to obtain some analytic insights and facilitates the numerical solution. Such a description has been employed to study the initial mixing of the solvent-swollen polymer film and the coagulation bath. The three-dimensional model has been used to study the evolution of structure that proceeds via nucleation and growth after the system enters the miscibility gap and then gradually crosses over to spontaneous phase separation in the vicinity of the mean-field spinodal, where the nucleation barrier is on the order of the thermal energy scale, $k_B T$.

The former is a thermally activated process and requires the addition of noise to the kinetic equations, eq 27. This strategy results in a set of stochastic partial differential equations that pose a significant numerical challenge.¹⁸⁴ Thermal fluctuations also shift the phase boundaries of the continuum model away from their simple mean-field estimates. It remains an important task to investigate the nucleation barriers in ternary polymer–solvent–nonsolvent mixtures. Assuming that the system is locally homogeneous, nucleation barriers in macrophase-separating systems can be efficiently computed by assuming that the new, stable phase emerges in a spherical volume, using the sphere's radius as a reaction coordinate.¹⁸⁵ In the case of block copolymer films, the new, stable phase is spatially structured, and the anisotropy of its surface tension will give rise to deviations of the nucleus from a spherical shape.^{186,187} In this case, more sophisticated techniques, e.g., calculations of the minimum free-energy path,¹⁸⁸ are required. It also remains to be explored to what extent the nucleation is heterogeneous because of the property gradient across the film thickness.

Assuming that the nucleation barrier in these mixtures containing polymers significantly exceeds $k_B T$ except in the ultimate vicinity of the spinodal and that the concomitant rate of nucleation is small compared to the kinetics of NIPS, one often considers that phase separation sets in the vicinity of the spinodal. In this case, the square-gradient theory predicts a spontaneous, exponential growth of a density mode with a wavevector-dependent growth rate.^{179,189,190} The fastest growing mode dominates the initial structure formation and templates the subsequent kinetics of structure formation. This spinodal decomposition is captured by the linear stability analysis of the homogeneous state. The free-energy costs of small fluctuations around the homogeneous state of the incompressible system are described by the collective structure factor, $S_{\alpha\beta\mathbf{q}}$ ¹⁶¹

$$\frac{F}{\rho V k_B T} = \frac{1}{2} \sum_{\mathbf{q}} \sum_{\alpha\beta} \phi_{\alpha\mathbf{q}} (S_{\mathbf{q}}^{-1})_{\alpha\beta} \phi_{\beta\mathbf{q}} \quad (28)$$

in Fourier space. The chemical potential and the linearized kinetic equation take the form

$$\frac{\mu_{\alpha\mathbf{q}}}{k_B T} = \sum_{\beta} (S_{\mathbf{q}}^{-1})_{\alpha\beta} \phi_{\beta\mathbf{q}} \quad (29)$$

$$\frac{\partial \phi_{\alpha\mathbf{q}}}{\partial t} = -\mathbf{q}^2 \Lambda_{\alpha\alpha} \frac{\sum_{\beta} \Lambda_{\beta\beta} (\mu_{\alpha\mathbf{q}} - \mu_{\beta\mathbf{q}})}{\sum_{\beta} \Lambda_{\beta\beta}} \equiv -\mathbf{q}^2 \sum_{\beta} D_{\alpha\beta\mathbf{q}} \phi_{\beta\mathbf{q}} \quad (30)$$

where we have assumed that the matrix of Onsager coefficients, Λ , is diagonal. The collective diffusion matrix is a combination of the collective structure factors and Onsager coefficients. If an eigenvalue, $\lambda_{\mathbf{q}}$, of the matrix $D_{\mathbf{q}}$ is negative, the corresponding eigenvector, $\varphi_{\mathbf{q}} = \sum_{\alpha} c_{\alpha} \phi_{\alpha\mathbf{q}}$, with c_{α} being the components of the eigenvector, will exponentially grow in time. For macrophase separation, the eigenvalue first changes sign for $|\mathbf{q}| = 0$. In accord with the square-gradient form of the free-energy functional or the Ornstein–Zernike form of the structure factor, the wavevector dependence of the eigenvalue can be approximated by $\lambda_{\mathbf{q}} \approx \lambda_0 (1 + \text{sign}(\lambda_0) [\xi \mathbf{q}]^2) < 0$ for small $|\mathbf{q}|$. Here ξ denotes the correlation length of fluctuations of the density mode $\varphi_{\mathbf{q}}$. An unstable density mode grows like

$$\varphi_{\mathbf{q}}(t) = \varphi_{\mathbf{q}}(0) \exp(R_{\mathbf{q}} t) \text{ with } R_{\mathbf{q}} = |\lambda_0| \mathbf{q}^2 (1 - [\xi \mathbf{q}]^2) \quad (31)$$

for $\lambda_0 < 0$. The growth rate is positive for $|\mathbf{q}| < 1/\xi$, and the maximal growth rate is obtained for $|\mathbf{q}^*| = 1/(\sqrt{2} \xi)$. This length scale of spinodal structure formation dominates the incipient morphology.

4.3.2.2. Model H. The effect of a barycentric, ϕ_α -averaged velocity field, \mathbf{u} , on the mass balance equation has already been introduced in eq 27. In model H, this mass balance is complemented by a kinetic equation for the velocity field, \mathbf{u} . Since such a description is most relevant at the later stages of structure formation, when the solvent density is rather small inside the film, we approximate the ternary system by an effective, incompressible two-component system, lumping the polymer and solvent density in the polymer-rich phase into $\phi \equiv \phi_{\bar{p}}(\mathbf{r})$. Incompressibility asserts that the complementary, effective nonsolvent density is $\phi_{\bar{n}} = 1 - \phi_{\bar{p}}(\mathbf{r})$; i.e., the system is described by a single order parameter, ϕ .¹⁸²

A kinetic equation for the velocity field, \mathbf{u} , can be constructed via a variational principle, where the Rayleighian, $\mathcal{R} = \dot{F} + \Phi/2$, is minimized with respect to the velocity field.¹⁷⁰ The change of free energy is given by

$$\begin{aligned} \dot{F} &= \int d\mathbf{r} \left(\frac{\delta \mathcal{F}}{\delta \phi_{\bar{p}}} \frac{\partial \phi_{\bar{p}}}{\partial t} + \frac{\delta \mathcal{F}}{\delta \phi_{\bar{n}}} \frac{\partial \phi_{\bar{n}}}{\partial t} \right) = -\rho \int d\mathbf{r} \mu \nabla(\phi \mathbf{u}_{\bar{p}}) \\ &= \rho \int d\mathbf{r} \mu (\nabla(\phi \mathbf{u}) - \nabla \mathbf{j}') \end{aligned} \quad (32)$$

where $\mu = \mu_{\bar{p}} - \mu_{\bar{n}}$ is the exchange potential, the continuity equation for ϕ , eq 27, has been used, and $\mathbf{j}' = \mathbf{j}_{\bar{p}} = -\mathbf{j}_{\bar{n}} = -\Lambda \nabla \mu$ with $\Lambda = \Lambda_{\bar{p}\bar{p}} \Lambda_{\bar{n}\bar{n}} / (\Lambda_{\bar{p}\bar{p}} + \Lambda_{\bar{n}\bar{n}})$ for a diagonal matrix of Onsager coefficients. The dissipation rate of the viscous flow is quantified by

$$\Phi_{\text{visc}} = \int d\mathbf{r} \frac{\eta}{2} \sum_{ij} (\Delta_i u_j + \Delta_j u_i)^2 \quad (33)$$

where η denotes the shear viscosity. The incompressibility of the fluid flow, $\nabla \cdot \mathbf{u} = 0$, can be enforced by a Lagrange multiplier, $\mathcal{R}' = \mathcal{R} - \int d\mathbf{r} p(\mathbf{r}) \nabla \cdot \mathbf{u}$, where p is identified with the pressure. Minimization of \mathcal{R}' yields

$$-\frac{\delta \mathcal{R}'}{\delta \mathbf{u}} = -\rho \phi \nabla \mu + \nabla \cdot (\eta [\nabla \mathbf{u} + (\nabla \mathbf{u})^T]) - \nabla p \quad (34)$$

$$= \mathbf{f}_\phi + \nabla \cdot (-p \mathbb{I} + \mathbf{t}) \stackrel{!}{=} 0 \quad (35)$$

i.e., Stokes' equation, where $\mathbf{t} = \eta [\nabla \mathbf{u} + (\nabla \mathbf{u})^T]$ is the shear stress and $\mathbf{f}_\phi = -\rho \phi \nabla \mu = -\nabla \Pi$ represents the thermodynamic force density that composition variations exert on the fluid, with Π being the osmotic stress tensor. This force density describes *inter alia* the Laplace pressure that curved interfaces between polymer/solvent and nonsolvent exert on the fluid. Special care has to be exerted to collocate the concomitant stress on a lattice when using finite-difference techniques.¹⁹¹

4.3.2.3. Two-Fluid Model. To account for the fact that the polymer/solvent and nonsolvent flow past each other in the course of structure formation, one explicitly distinguishes between their velocities, $\mathbf{u}_{\bar{p}}$ and $\mathbf{u}_{\bar{N}}$ in the two-fluid model.^{170,192} [Here we only illustrate the formalism for the effective two-component model. The description has been generalized to three-component mixtures by Tree and co-workers.¹⁸³] The barycentric velocity is given by $\mathbf{u} = \phi \mathbf{u}_{\bar{p}} + (1 - \phi) \mathbf{u}_{\bar{N}}$, and the mass balance of the incompressible system reads^{170,171}

$$\begin{aligned} \frac{\partial \phi}{\partial t} &= -\nabla \cdot (\phi \mathbf{u}_{\bar{p}}) = \nabla \cdot ((1 - \phi) \mathbf{u}_{\bar{N}}) \\ &= -\nabla \cdot (\phi \mathbf{u}) - \nabla \cdot (\phi(1 - \phi)(\mathbf{u}_{\bar{p}} - \mathbf{u}_{\bar{N}})) \end{aligned} \quad (36)$$

$$\Phi_{\text{fric}} = \int d\mathbf{r} \zeta (\mathbf{u}_{\bar{p}} - \mathbf{u}_{\bar{N}})^2 \quad (37)$$

where ζ stands for the friction constant per unit volume. The variation of the Rayleighian yields

$$-\frac{\delta \mathcal{R}'}{\delta \mathbf{u}_{\bar{p}}} = -\rho \phi \nabla \mu + \nabla \cdot \mathbf{t}_{\bar{p}} - \phi \nabla p + \zeta (\mathbf{u}_{\bar{p}} - \mathbf{u}_{\bar{N}}) \stackrel{!}{=} 0 \quad (38)$$

$$-\frac{\delta \mathcal{R}'}{\delta \mathbf{u}_{\bar{N}}} = \nabla \cdot \mathbf{t}_{\bar{N}} - (1 - \phi) \nabla p - \zeta (\mathbf{u}_{\bar{p}} - \mathbf{u}_{\bar{N}}) \stackrel{!}{=} 0 \quad (39)$$

where the pressure, p , is chosen to enforce the incompressibility constraint $\nabla \cdot [\phi \mathbf{u}_{\bar{p}} + (1 - \phi) \mathbf{u}_{\bar{N}}] = 0$. The sum of these two equations yields the Stokes' stress balance

$$-\rho \phi \nabla \mu + \nabla \cdot (-p \mathbb{I} + \mathbf{t}_{\bar{p}} + \mathbf{t}_{\bar{N}}) = 0 \quad (40)$$

whereas the weighted difference results in

$$\begin{aligned} -\rho(1 - \phi) \phi \nabla \mu + (1 - \phi) \nabla \cdot \mathbf{t}_{\bar{p}} - \phi \nabla \cdot \mathbf{t}_{\bar{N}} + \zeta (\mathbf{u}_{\bar{p}} - \mathbf{u}_{\bar{N}}) \\ = 0 \end{aligned} \quad (41)$$

Such a two-fluid description can account for the viscosity difference between the nonsolvent and polymer that may lead to a viscous fingering instability.^{193,194}

4.3.2.4. Viscoelastic Model. The mass balance equation, eq 36, as well as Stokes' equation, eq 40, and the kinetic eq 41 for the relative velocity between polymer and solvent also hold for viscoelastic fluids. Viscoelasticity accounts for internal degrees of freedom, that are not described by the hydrodynamic variables, densities ϕ_a , and velocities, \mathbf{u}_a . Such internal degrees of freedom may equilibrate on a time scale comparable to the time, on which the hydrodynamic variables evolve. To generalize these expressions from incompressible Newtonian to viscoelastic fluids, constitutive equations that link the stresses, $\mathbf{t}_{\bar{p}}$ and

$\mathbf{t}_{\bar{N}}$, to the velocity gradients, are needed. Within a linear response, the latter equations take the form¹⁷¹

$$\mathbf{t}_\alpha = \int_{-\infty}^t dt' \{ G_\alpha^S(t - t') \kappa_\alpha + G_\alpha^B(t - t') (\nabla \mathbf{u}_\alpha) \mathbb{I} \} \quad (42)$$

where $\alpha = \bar{P}$ or \bar{N} stands for the different components. $G_\alpha^S(t)$ and $G_\alpha^B(t)$ represent the shear and bulk relaxation moduli of the materials, and κ_α is the symmetric, traceless, velocity-gradient tensor.

Alternatively, one can explicitly incorporate the slow, collective variables both in the free-energy functional as well as in the kinetic equation.¹⁹⁵ For instance, the symmetric conformational tensor, \mathbb{X}^2 of molecular conformations of the entire chain or on the length scale of entanglements can serve to quantify the nonequilibrium conformations.

$$\mathbb{X}^2(\mathbf{r}) \sim \sum_{i \in \Delta V(\mathbf{r})} \mathbf{R}_i \mathbf{R}_i^T \quad (43)$$

where \mathbf{R}_i may denote the end-to-end distance, the first Rouse mode, or the tube-segment vector of a macromolecule, i , inside a volume element ΔV around the position, r . The proportionality constant is chosen such that in a spatially homogeneous system in equilibrium, $\langle \mathbb{X}^2(\mathbf{r}) \rangle = \mathbb{I}$, holds.

The constraint on the molecular conformations increases the free energy of a spatially homogeneous system by^{195–200}

$$\begin{aligned} \frac{\Delta F_{\text{el}}(\mathbb{X}^2)}{\rho V k_B T / N} &\sim -\frac{1}{2} \ln \det(\mathbb{X}_1^2) + \frac{1}{2} \text{tr}(\mathbb{X}_1^2 - \mathbb{I}) \\ &\approx \frac{1}{4} \text{tr}([\mathbb{X}^2 - \mathbb{I}]^2) \end{aligned} \quad (44)$$

where, in the last term, we have assumed that the deviation of \mathbb{X}^2 from its equilibrium value \mathbb{I} is small. The free-energy cost in a phase-separated system can be computed by SCFT.²⁰¹ To a first approximation, the elastic contribution to the free-energy functional becomes¹⁹⁵

$$\frac{\Delta \mathcal{F}_{\text{el}}[\mathbb{X}^2]}{\rho k_B T / N} = \int d\mathbf{r} \frac{G_0 \phi_p^3}{4} \text{tr}([\mathbb{X}^2(\mathbf{r}) - \mathbb{I}]^2) \quad (45)$$

where G_0 is a constant and the ϕ_p dependence corresponds to an entangled polymer solution.¹⁹⁵

Since there is no conservation law associated with the conformational tensor, \mathbb{X}^2 is convected and affinely deformed by the flow and relaxes toward its equilibrium value on the time scale τ_{visc} according to¹⁹⁵

$$\begin{aligned} \frac{D}{D_{\bar{p}} t} \mathbb{X}^2 &= \left(\frac{\partial}{\partial t} + \mathbf{u}_{\bar{p}} \cdot \nabla \right) \mathbb{X}^2 \\ &= \mathbb{K}_{\bar{p}} \mathbb{X}^2 + \mathbb{X}^2 \mathbb{K}_{\bar{p}}^T - \frac{1}{\tau_{\text{visc}}} (\mathbb{X}^2 - \mathbb{I}) \end{aligned} \quad (46)$$

where $\mathbb{K}_{\bar{p}}$ denotes the velocity-gradient tensor. The stress, in turn, is given by

$$\mathbf{t}_{\bar{p}} \sim \mathbb{X}^2 [\mathbb{X}^2 - \mathbb{I}] \quad (47)$$

Accounting for the viscoelasticity of the polymer material is important to account for entanglement effects (cf., Figure 5) and, additionally, the glassy slowing down of the dynamics as the polymer vitrifies. In the early stages of spinodal phase separation,^{171,202} viscoelastic phase separation resembles diffusive macrophase separation according to model B with an Onsager coefficient that is nonlocal in time, cf., eq 20^{173–175} or

alternate forms.²⁰³ In the intermediate stages, however, the morphology differs significantly. In particular, the viscoelastic component can form a bicontinuous network structure even if it is the minority phase (see also Figure 10).¹⁹⁵ Some effects of viscoelastic phase separation can also be phenomenologically captured by a density dependence of the friction or Onsager coefficients, although the physical mechanisms differ.¹⁷¹

4.3.2.5. Dynamic Slowing Down. In the course of phase separation the polymer-rich phase arrests and becomes a solid on the experimental time scale. Such a slowing down can be caused by (i) vitrification, (ii) crystallization, or (iii) gelation.

All three cases involve structural properties that are not covered by the above-mentioned continuum description in terms of density and velocity. In the case of vitrification, the density in the polymer-rich domain increases, and the segmental mobility rapidly drops in a narrow density range because of correlations in the fluid-like packing structure (cage formation). Whereas these packing correlations are not captured by the collective density fields, ϕ_w the threshold to vitrification is directly related to the local ϕ_p . Therefore, this slowing down can be effectively incorporated via a density dependence of the Onsager coefficients^{144,146,204–206} or more accurately by the density dependence of the dynamic-mechanical moduli in eq 42.¹⁷¹ A glassy material is characterized by shear or bulk moduli that do not decay to zero but retain an elastic component even in the limit of long times. The interplay of phase separation and vitrification has attracted abiding interest,^{171,204,205,207–209} resulting in a gel-like structure (see also Figure 10).

Alternatively, the kinetics of structure formation can be arrested by the formation of a permanent percolating polymer network (gel), giving rise to a permanent elastic response. This is particularly relevant in the case of interpenetrating polymer networks (IPNs), semi-interpenetrating polymer networks (semi-IPNs), or polymerization-induced phase separation (PIPS).^{72,154} The concomitant topological constraints that hinder large-scale structure formation are most difficult to describe,^{210–217} and the equilibrium phase behavior of multi-component networks is only incompletely understood.

The dynamics in the polymer-rich domains can also be arrested by a phase transition to a crystalline phase.^{218–224} Again, the crystalline solid is characterized by an order parameter that differs from the density fields and gives rise to an elastic response. In contrast to vitrification, however, the material inside a crystallite is not isotropic, the chain connectivity plays an important role, and the kinetics of crystallization via nucleation and growth may occur on a time scale comparable to that of evaporation-induced structure formation.²²⁴

4.4. Particle Simulations

Molecular simulations describe the system via the explicit coordinates and momenta of the constituents. Such a particle-based description can overcome some of the limitations of continuum models. Most notably, particle simulations naturally account for different macromolecular architectures, additional slow conformational degrees of freedom, \mathbb{X}^2 , like the macromolecular orientations and the dynamic asymmetry of the constituents that may, additionally, depend on the local environment. Since the explicit particle degrees of freedom are propagated in time by molecular dynamics, Brownian dynamics, or a Monte Carlo (MC) algorithm, particle simulations provide direct insights into the kinetics of phase separation or self-assembly and capture the dynamic correlation between the

single-molecule motion, the relaxation of macromolecular conformations, and the kinetics of the collective densities. These correlations are quantified in the Onsager coefficients, $\Lambda_{\alpha\beta}$ for model B and H or in the viscoelastic relaxation moduli in the case of viscoelastic phase separation. Often, however, accurate and detailed expressions for these constitutive relations of continuum models are not available for inhomogeneous systems or complex macromolecular architectures. For instance, a particle-based description naturally accounts for entanglement effects in a spatially inhomogeneous, phase-separating system. Moreover, particle simulations always include thermal fluctuations. Additionally, particle simulations may also capture the density-dependent slowing down or additional phenomena, such as, e.g., gelation or crystallization, that eventually lead to the arrest of structure formation.

The major difficulties of particle simulations, however, are the time and length scales of NIPS. Typical films have a thickness of multiple micrometers, and solvent–nonsolvent exchange occurs on time scales of seconds to minutes. These scales greatly exceed the characteristic time and length scales of solvent–molecule motion. In order to partially narrow this scale gap, highly coarse-grained models are employed that do not account for all atomic details of the constituents of the ternary mixture but rather lump a small number of atoms into a coarse-grained segment.^{82,225–230}

Simulation techniques appropriate for studying NIPS are similar to those employed to study solvent evaporation from thin films of homopolymers.^{145–147,231–233} Since the structure formation involves time and length scales that greatly exceed the scales of a monomeric repeating unit, a highly coarse-grained description is often adopted. In this case, a large number of monomeric repeating units along the polymer backbone are lumped into an effective interaction center or segment.^{82,225–230} Such models can be derived by systematic coarse-graining from an atomically realistic model,^{225–230} or a top-down approach is adopted where only the relevant interactions—such as, e.g., macromolecular connectivity, repulsion between polymer and nonsolvent or the different blocks of the copolymer, and near-incompressibility of the mixtures—are incorporated, and their strengths are determined by comparison to atomic simulations or experiments.²²⁷

In order to treat the solvent/nonsolvent and the polymer on the same footing, it is tempting to also lump a small number of solvent molecules into one coarse-grained solvent particle. For example, in the popular MARTINI model,²³⁴ four water molecules are represented by one coarse-grained solvent molecule, and such an approach has also been used for dissipative particle dynamics (DPD) simulations of NIPS.²³⁵ In the case of spatially inhomogeneous systems, such as phase-separating mixtures, however, special care has to be exerted to account for the loss of translational entropy, resulting from the decimation of the number of indistinguishable molecules, which gives rise to density-dependent interactions.²³⁶

Alternatively, one can entirely integrate out the solvent and represent the incompressible polymer–solvent–nonsolvent mixtures by a compressible mixture of polymer and nonsolvent. Also, in this case, density-dependent interactions that describe three- and higher-order multibody interactions have to be included to capture the complex thermodynamics of the mixtures,^{237,238} in analogy to eq 6.

Systematic coarse-graining^{225–230} asserts that the interactions between particles that represent a large number of atoms are soft because the center of mass of a collection of atoms can overlap

even if the individual constituents cannot. DPD simulation models account for this property by using soft, nonbonded interactions. Moreover, they employ a thermostat that locally conserves momentum. The latter results in hydrodynamics on large scales.^{239–242} Both the decimation of the number of degrees of freedom and the softness and simplicity of the interactions, allowing, e.g., for a larger time step, contribute to the significant computational speed-up.

The softness of the interaction, however, affects the dynamics. For example, the softness of the coarse-grained particles does not enforce the noncrossability of polymers in the course of their motion that gives rise to entanglements and reptation dynamics, although techniques to effectively mimic entanglement effects in soft, coarse-grained polymer models are available via explicit prevention of bond crossing,²⁴³ spring–spring repulsion,²⁴⁴ modification of interaction parameters,^{245–247} pseudocontinuous molecular contours,²⁴⁸ or slip-springs.^{249–253} Such effects dictate the viscoelastic behavior and are relevant to NIPS (see below).

Moreover, the soft interactions often do not result in a realistic slowing down of the dynamics upon an increase of the local density; i.e., the soft model does not vitrify or crystallize upon increase of density. Since in highly coarse-grained particle models, friction does not chiefly stem from the (ultra)soft, nonbonded interactions but rather from the thermostat, there are opportunities to account for a specific, experimentally informed dependence of the mobility on the local environment by a composition-dependent particle friction coefficient of the thermostat.¹⁴⁶

These issues exemplify that the softness of the nonbonded interactions has a pronounced effect on the single-chain dynamics and the concomitant collective kinetics. On the one hand, specific modifications of the simulation model are required to account for these effects. On the other hand, however, such modifications permit one to tailor the dynamics of the coarse-grained model without altering the thermodynamics. This allows for an independent variation of thermodynamic and dynamic properties and results in a clear separation between both properties, facilitating the representation of a specific experimental system by the coarse-grained model.²⁵³

Such coarse-grained models can be studied by molecular dynamics in conjunction with the DPD thermostat, whose local conservation of momentum results in hydrodynamic behavior on large scales.^{239–242} Alternatively, the nonbonded interactions can be collocated on a grid.^{227,254} This strategy allows for a very efficient calculation of the nonbonded interactions but prevents the investigation of hydrodynamic flow and significantly complicates the calculation of the pressure.

The scale separation between the strong bonded interactions along the polymer backbone and the weak but computationally costly nonbonded interactions can be accounted for by the single-chain-in-mean-field (SCMF) algorithm.^{146,227,254} In the case of macromolecular systems with a large invariant degree, \bar{N} , of polymerization, this algorithm allows for a very efficient calculation of nonbonded interaction and a massive parallelization of the simulation.²⁵⁵

In general, particle simulations are computationally more expensive than studies of continuum models. They can, however, more naturally account for additional microscopic aspects such as, e.g., molecular architecture or the interplay between chain conformations, stress, and flow in spatially inhomogeneous systems. These aspects typically become important on short or moderate length and time scales.

Therefore, insights from particle simulations may inform the effective parameters of continuum models via parameter passing or, ideally, concurrent techniques such as, e.g., the heterogeneous multiscale method (HMM), could be employed.²⁵⁶

4.5. Applications to Nonsolvent-Induced Phase Separation (NIPS)

4.5.1. Continuum Models. **4.5.1.1. Model B – One-Dimensional Process Paths.** The first model of NIPS that incorporated the thermodynamics of the ternary film and the diffusive kinetics was devised by Cohen, Tanny, and Prager⁹⁴ as early as 1978. The authors considered the time evolution of the one-dimensional density variation perpendicular to the film surface during the early stages, after the solvent-swollen polymer film is brought in contact with the coagulation bath—the initial mixing phase. The film is assumed to be transversely uniform. As the solvent leaves the film (and partly exchanges with the nonsolvent), the film thickness, $h(t)$, i.e., the distance between the supporting substrate and the film surface, decreases. The authors chose the density of the solvent, ϕ_S , and of the nonsolvent, ϕ_N , as independent density fields. By virtue of incompressibility, the polymer density is given by $\phi_P = 1 - \phi_S - \phi_N$.

Considering that variations of the density only depend on the distance, z , from the substrate that supports the solvent-swollen polymer film, using $\phi_S(z)$ and $\phi_N(z)$ as independent variables, and assuming that the matrix of Onsager coefficients is diagonal, one obtains

$$\frac{\partial \phi_S(z, t)}{\partial t} = \frac{\partial}{\partial z} \left\{ \frac{\Lambda_{SS}\Lambda_{PP}\frac{\partial}{\partial z}(\mu_S - \mu_P) + \Lambda_{SS}\Lambda_{NN}\frac{\partial}{\partial z}(\mu_S - \mu_N)}{\Lambda_{PP} + \Lambda_{SS} + \Lambda_{NN}} \right\} \quad (48)$$

$$\frac{\partial \phi_N(z, t)}{\partial t} = \frac{\partial}{\partial z} \left\{ \frac{\Lambda_{NN}\Lambda_{PP}\frac{\partial}{\partial z}(\mu_N - \mu_P) + \Lambda_{NN}\Lambda_{SS}\frac{\partial}{\partial z}(\mu_N - \mu_S)}{\Lambda_{PP} + \Lambda_{SS} + \Lambda_{NN}} \right\} \quad (49)$$

This is a set of partial differential equations (PDEs) of first order in time and fourth order in space. Therefore, one needs the initial density profiles and four boundary conditions. There is no flux through the supporting substrate; i.e., a von Neumann boundary condition is applied, $j'_{z\alpha} = 0$ at $z = 0$, cf., eq 24. Additionally, the substrate may locally prefer one component of the mixtures, and the corresponding local equilibrium condition determines the gradient of the densities at the substrate according to eq 16.

The square-gradient free-energy functional may not accurately describe the disparate scales of both the intrinsic width, b , of the narrow film surface (cf., eq 12), on the order of a nanometer, and density variation inside the film, whose thickness may exceed micrometers. Moreover, local equilibrium at the film surface is quickly established on a time scale $\tau_{fs} \sim b^2/D$ (where D denotes a typical value of the diffusion constant) that is significantly shorter than all other characteristic times of structure formation.^{169,257} Therefore, the rapid density variation at the film surface is not explicitly considered, and a “sharp-interface” approach^{257–259} is adopted.

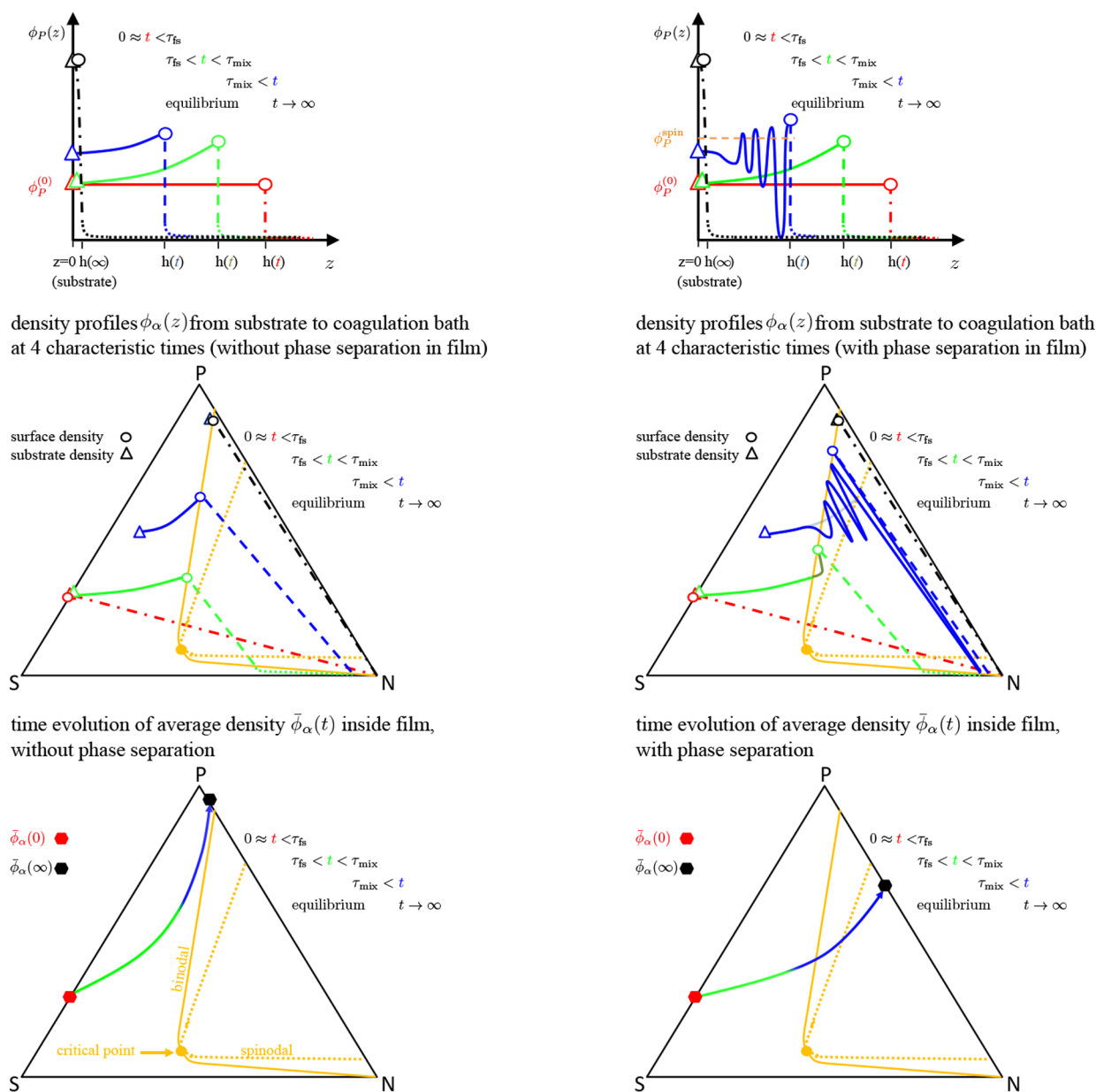


Figure 6. Schematic representation of NIPS. Top-row panels show the time evolution of the density profile, $\phi_P(z)$, across the system. The left column refers to a process where the film surface recedes upon solvent–nonsolvent exchange, but no phase separation occurs inside the film, whereas right panels illustrate a NIPS process with surface-directed spinodal decomposition. The red color corresponds to the initial contact between polymer film and coagulation bath, $0 \approx t < \tau_{fs}$, whereas the black color corresponds to the equilibrium, assuming that the polymer wets the substrate. The green color illustrates profiles in the mixing regime, $\tau_{fs} < t < \tau_{mix}$, while the blue color shows profiles for $t > \tau_{mix}$. Solid green and blue lines represent the profile inside the polymer film (process path), dashed lines represent the density variation across the film surface, and dotted lines illustrate the density profile in the coagulation bath. Triangles denote the densities at the substrate, whereas open circles mark the densities at the film surface. Lower panels depict NIPS on the phase triangle. Yellow solid lines indicate binodals, whereas yellow dashed lines represent spinodals. The yellow, solid circle denotes the critical point or plait point. Panels in the middle row depict the density profiles, $\phi_\alpha(z)$, across the entire system. Different colors correspond to distinct times. The distance, z , is a parameter along the curves and varies from $z = 0$ left to $z = L$ right, bottom. Bottom panels present the film-averaged densities, $\bar{\phi}_\alpha^{film}$, in the course of NIPS. Time, t , is a parameter along the curves and varies from $t = 0$ (left, red hexagon, $\bar{\phi}_\alpha^{(0)}$), to the equilibrium (right, black hexagon). The color shading along the line indicates the mixing region (green) and later times (blue), $t > \tau_{mix}$.

Specifically, Cohen, Tanny, and Prager⁹⁴ assume that the film surface is in local equilibrium with a coagulation bath and that the densities of the latter do not vary in time; i.e., the coagulation bath is represented by an infinite, “well stirred” reservoir. Technically, this assumption corresponds to modeling an open system. At the surface of the film, $z = h$, in contact with the coagulation bath, local equilibrium between the inside of the film and the coagulation bath is established if the chemical potentials

of all species across the film surface are equal. This does not necessarily mean that the density profile remains continuous in this sharp-interface limit.²⁶⁰ Alternatively, one can prescribe a relation between the flux at the film surface and the surface densities,^{261,262} which is often done to describe solvent evaporation.^{143,144,263–265}

The model has been improved and refined in various aspects, e.g., by modifying the boundary condition at the film surface or

including the spatiotemporal variation of the density in the coagulation bath.^{260,261,266–271}

The flux of the solvent out of the film and the flux of nonsolvent into the film dictate the time evolution of the film thickness, $h(t)$. Assuming that the polymer is insoluble in the coagulation bath, the conservation of the total amount of polymer in the film yields

$$\begin{aligned} \{1 - \phi_S(h, t) - \phi_N(h, t)\} \frac{dh}{dt} &= \phi_P(h, t) \frac{dh}{dt} = j'_P(h, t) \\ &= -[j'_S(h, t) + j'_N(h, t)] \end{aligned} \quad (50)$$

i.e., this jump condition asserts that the velocity of the polymer at the surface $u_p = j'_P(h, t)/\phi_P(h, t)$ coincides with the velocity, dh/dt , of the film surface.

The boundary condition, derived from a jump condition of the fluxes at the sharp film surface, is modified if the kinetics inside the film and the coagulation bath are simultaneously considered.^{260,261,271} In order to describe the mass transfer across the film surface, the coagulation bath must be large enough to act as a reservoir.

The moving-boundary condition at the film surface can be avoided by explicitly resolving the rapid density variation across the film surface.¹⁶⁹ The mismatch between the narrow film surface and the large coagulation reservoir, however, considerably increases the computational cost. This corresponds to the boundary condition

$$\phi_\alpha(z, t) = \phi_\alpha^{\text{bath}} \text{ and } \frac{\partial \phi_\alpha}{\partial z} = 0 \text{ for } z \rightarrow \infty \text{ and all times, } t \quad (51)$$

Applying this boundary condition at a finite system size, $z = L$, allows for a flux at the system boundary; i.e., the system is open and the densities of the coagulation bath, $\phi_\alpha^{\text{bath}}$, dictates the equilibrium chemical potentials, μ_α^{bath} , and the concomitant equilibrium density profile.

Instead of using the spatial distance, z , from the supporting substrate, Cohen, Tanny, and Prager⁹⁴ found it convenient to define a distance-like material variable $\zeta(z)$

$$\begin{aligned} \zeta(z) &= \int_z^{h(t)} dz' \frac{\phi_P(z')}{\phi_P^{(0)}} \\ &= \int_z^{h(t)} dz' \frac{1 - \phi_S(z') - \phi_N(z')}{\phi_P^{(0)}} \end{aligned} \quad (52)$$

where $\phi_P^{(0)}$ denotes the initial density of the polymer in the solvent-swollen film. The quantity $\zeta(z)/h(0)$ measures the fraction of polymer between z and the moving film surface, $h(t)$. Initially, $\zeta(z) = h(0) - z$ for $z \leq h(0)$ at time $t = 0$. Moreover, $\zeta(z)$ monotonously decreases with z and $\zeta(h(t)) = 0$ because the solubility of the polymer in the coagulation bath is assumed to be vanishingly small, $\zeta(0) = h(0)$ for all times. Replacing the gradients along the z direction by $\frac{\partial}{\partial z} = -[1 - \phi_S - \phi_N]/\phi_P^{(0)} \frac{\partial}{\partial \zeta}$ in eq 48 and eq 49, one maps the moving-boundary problem onto a fixed interval, $0 \leq \zeta \leq h(0)$.

Typically, the initial condition at time $t = 0$ is a homogeneous solvent-swollen film, $\phi_N(\zeta) = 0$ and $\phi_S(\zeta) = 1 - \phi_P^{(0)}$. In an idealized situation, the coagulation bath does not contain solvent, $\phi_S^{\text{bath}} \ll 1$, the polymer is insoluble in the coagulation bath, $\phi_P^{\text{bath}} \ll 1$, and the coagulation bath coexists with a

polymer-rich film of density ϕ_P^{coex} . Often, the polymer density at the film surface rapidly increases toward ϕ_P^{coex} , and a polymer skin or separation layer is formed.^{140,260,272} As time progresses, the thickness, Δh , of this enrichment zone at the film surface increases diffusively in time, $\Delta h^2 \sim t$. For short times and/or thick films, the density at the substrate remains unaltered, and the density profiles depend on position and time only via the scaling variable ζ/\sqrt{t} as long as Δh remains much smaller than the film thickness, h .^{94,169,257} If diffusive transport dominates, i.e., the Péclet number $\text{Pe} = \frac{dh}{dt} / \frac{\Lambda}{h}$, which quantifies the ratio between the velocity of the receding film surface and the diffusive current, is of order unity or smaller,¹⁴⁴ this self-similar mixing extends up to time $\tau_{\text{mix}} \sim h^2(0)/\Lambda$, where $h(0)$ denotes the initial film thickness and Λ the scale of the Onsager coefficients in eq 24. The same scaling of the spatiotemporal dependence also holds for the profiles inside the coagulation bath.

At any time, $t < \tau_{\text{mix}}$, density profiles will continuously vary in space from the initial values, $\phi_\alpha^{(0)}$, of the film, which are attained at the supporting substrate, to the values, $\phi_\alpha^{\text{bath}}$, in the coagulation bath. Initially, $t < \tau_{\text{fs}}$, the profiles will sharply interpolate between $\phi_\alpha^{(0)}$ and $\phi_\alpha^{\text{bath}}$, as illustrated by the red profile in the upper-row panels of Figure 6. Once the local equilibrium at the film surface is reached, $t > \tau_{\text{fs}}$, a narrow surface between solvent-swollen polymer film and coagulation bath has been established, and often an enrichment layer of polymer is formed at the film surface.¹⁴³ The densities on both sides of the narrow surface approximately correspond to the densities, at which a solvent-swollen polymer film coexists with the coagulation bath; i.e., they are connected close to the tie lines in the phase triangle.^d Such a density profile is depicted by the green density profiles in the top row of Figure 6.^e Since the solvent leaves the film, its local density also decreases at the surface, and the tie line that describes the rapid density variation across the surface shifts to smaller solvent densities. Additionally, the density at the substrate will change for $t > \tau_{\text{mix}}$. Such a late-stage profile is shown by the blue density profile.

If the portion of the density profile inside the film—the process path²⁶¹—will remain inside the one-phase region in the course of solvent–nonsolvent exchange (see left column of Figure 6), the film will remain homogeneous, and a one-dimensional description suffices. This situation occurs *inter alia* in the course of solvent evaporation, when polymer and solvent are miscible at all densities, and the nonsolvent (e.g., air) does not significantly enter the film because χ_{SN} is significant and the density of the solvent in the nonsolvent is negligibly small.^f Ultimately, the system will equilibrate; i.e., the fluxes vanish and the chemical potentials adopt their equilibrium value, μ_α^{bath} , throughout the system. The corresponding density profile is illustrated by the black line in Figure 6. In equilibrium, the polymer film will either condense into a dense layer at the substrate or dissolve in the coagulation bath. In both cases, the densities in the coagulation bath, $\phi_\alpha^{\text{bath}}$, and the interaction with the substrate, $\mu_{w\alpha}$ and $\chi_{w\alpha\beta}$, become important because the equilibrium corresponds to the wetting of the polymer on the substrate.^{151,273} In the limiting case, $\phi_S^{\text{bath}} = 0$, all solvent leaves the system through the boundary at $z = L$, and the system effectively becomes an incompressible, binary mixture of polymer and nonsolvent; i.e., only the exchange chemical potential $\mu^{\text{bath}} = \mu_N^{\text{bath}} - \mu_S^{\text{bath}}$ is relevant, and phase coexistence between a polymer-rich and a nonsolvent-rich phase occurs at a specific value, μ^{coex} . The polymer density in the thermodynamically

cally stable coagulation bath is small so that $\mu^{\text{bath}} \leq \mu^{\text{coex}}$; otherwise, polymer droplets would nucleate in the coagulation bath. If the preference of the substrate for the polymer is sufficiently large, such that the polymer-rich phase wets the substrate, the polymer-rich phase will form a film on the substrate, whose thickness, h^{eq} , will increase logarithmically with the distance from phase coexistence (complete wetting), $h^{\text{eq}} \sim -b \ln(\mu^{\text{coex}} - \mu^{\text{bath}})$ (complete wetting).^{273 g} In the case that the substrate preference is insufficient to make the polymer-rich phase wet, the polymer will dissolve in the coagulation bath, and only a minuscule excess of polymer will remain on the substrate. In an experiment, however, this thermodynamic equilibrium may not be accessible because of dynamic arrest.

There are various possibilities of representing the one-dimensional, spatiotemporal density profiles in the phase triangle of the incompressible ternary mixture. In the middle, left panel of Figure 6, we transfer the density profiles of the top, left panel onto the phase triangle. Different colored lines correspond to the four characteristic times—initial contact (red), mixing regime (green), late stage (blue), and equilibrium (black). The portions of the density profile inside the film are marked by solid lines—these correspond to the process paths.²⁶¹ The rapid variation of the density across the narrow film surface, close to the tie lines, is illustrated by dashed lines, whereas the density profiles inside the coagulation bath are shown by dotted lines.

Alternatively, one can consider the average densities, $\bar{\phi}_\alpha^{\text{film}} = \frac{1}{h} \int_0^h dz \phi_\alpha$, inside the film as a function of time. If the process path remains in the one-phase region, no structure formation occurs inside the polymer film, and $\bar{\phi}_\alpha^{\text{film}}$ will gradually move from its initial value $\bar{\phi}_\alpha^{\text{film}} = \phi_\alpha^{(0)}$ at $t = 0$ to the equilibrium densities at the substrate in contact with the coagulation bath. This time evolution of the average densities on the phase triangle is depicted in the lower, left panel of Figure 6. At no time or position inside the film do the density profiles enter the miscibility gap, and therefore $\bar{\phi}_\alpha^{\text{film}}$ also remains outside the miscibility gap. In addition to tie lines and spinodal stability limits, density regions, in which the ternary system vitrifies or gels can be indicated on the phase triangle, signaling where the system will dynamically arrest.

If the portion of the density profile inside the polymer film bulges inside the miscibility gap in the course of NIPS, phase separation occurs via nucleation and growth. If it even reaches beyond the spinodal, the (nearly) homogeneous state becomes unstable and will spontaneously phase separate. Both effects involve transversal structure formation and cannot be described by a one-dimensional model. The one-dimensional model, however, predicts its limit of validity, and the density profiles inside the film in the course of solvent–nonsolvent exchange are important because their “hypothetical” location inside the miscibility gap provides information about the mechanism of NIPS—nucleation and growth or spinodal decomposition—and yields important additional insights, e.g., into the length scale of the incipient structure formation (see eq 31). This interplay between equilibrium phase behavior and one-dimensional spatiotemporal density variation across the film surface is discussed in detail in refs 169 and 261. The corresponding density profiles as a function of the distance, z from the substrate and on the phase triangle for four characteristic times as well as the time evolution of the film-averaged densities are sketched in the right column of Figure 6.

As long as the process path remains outside the region of spinodal instability, metastable profiles can be obtained and drawn on the phase triangle. Once the process path, however, crossed the spinodal, even the one-dimensional profile will become unstable, and layers will form. To some extent, the layering is an artifact of the one-dimensional model, and surface-directed spinodal decomposition^{169,274} will ensue in a two- or three-dimensional system (*vide infra* Figure 7 and Figure 8),

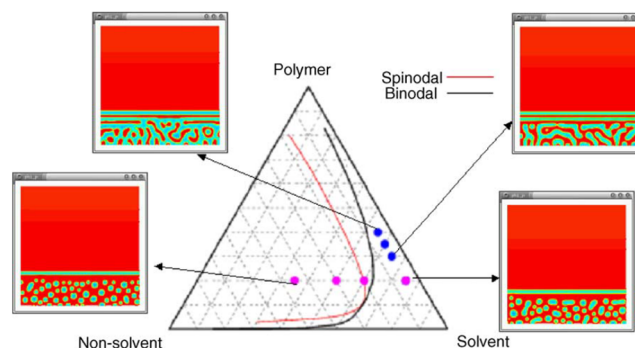


Figure 7. 2D Cahn–Hilliard study of the morphologies that are formed by bringing a polymer–solvent–nonsolvent mixture in contact with a nonsolvent-rich coagulation bath. The initial densities of the polymer film are indicated in the phase triangle by circles, and the two-dimensional plot depicts the polymer density. Red indicates vanishingly small polymer density, $\phi_p \approx 0$, while blue marks regions of high ϕ_p . Reprinted with permission from ref 274. Copyright 2006 Elsevier.

provided that the width of the zone, in which the system is unstable, exceeds the characteristic length scale of the spontaneous phase separation. Nevertheless, this layering can also be appreciated in Figure 7 and Figure 8, and it gives rise to a snaking path on the phase triangle. With the same caveat as before, the profile across the layers will approximately follow the tie lines, giving rise to a process path that goes forth and back in the vicinity of the tie line.

Representing the time evolution of a phase-separating system by its film-averaged densities, $\bar{\phi}_\alpha^{\text{film}}$, is more complicated because the profile inside the film exhibits a nontrivial shape for $t < \tau_{\text{mix}}$. For thick films, a portion of the film close to the surface may already enter the miscibility gap or the region of spinodal instability, whereas the densities close to the substrate may remain close to their initial values, $\phi_\alpha^{(0)}$. Therefore, the film may undergo phase separation at the film surface even if the film-averaged densities, $\bar{\phi}_\alpha^{\text{film}}$, are still in the one-phase region. If phase separation occurs on long time scales, $t > \tau_{\text{mix}}$ however, diffusion across the entire film establishes more uniform density profiles that is faithfully characterized by $\bar{\phi}_\alpha^{\text{film}}$. In this case, plotting the film-averaged densities on the phase triangle identifies the point where the entire film enters the miscibility gap or the region of spinodal instability. When phase separation sets in, domains that are rich in polymer or accumulate nonsolvent will form. The local densities inside these domains are close to the coexistence values at the ends of the tie line. This $\bar{\phi}_\alpha^{\text{film}}$ denotes their volume-weighted average according to the “lever rule”.

4.5.1.2. Surface-Directed Spinodal Decomposition and Hydrodynamic Flow. Zhou and Powell²⁷⁴ used a Cahn–Hilliard approach to investigate the demixing in a ternary polymer–solvent–nonsolvent mixture in contact with a coagulation bath. They investigated the influence of the initial compositions, the role of dynamic asymmetry and gradient

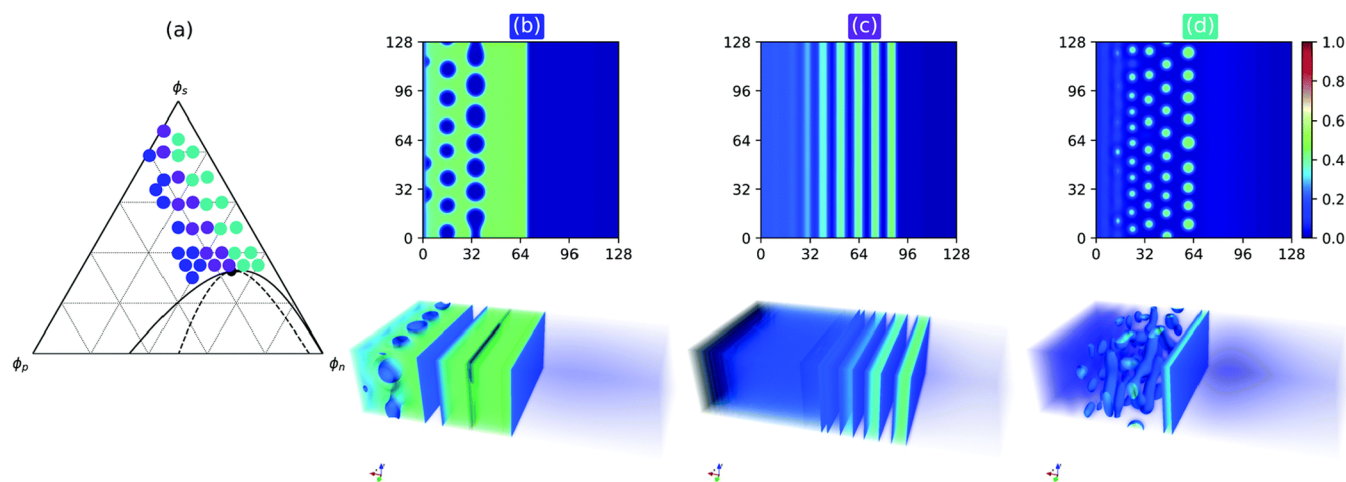


Figure 8. Surface-directed spinodal decomposition in two and three dimensions as a function of the initial polymer density, indicated in the phase triangle in panel a. Panels b–d present the polymer density at long times according to the color bar on the right. Upon decreasing the initial polymer density, $\phi_p^{(0)}$, from panel b to d, Tree and co-workers observed a transition from nonsolvent droplets, via alternating layers of nonsolvent and polymer, to polymer droplets. Republished with permission of the Royal Society of Chemistry (Great Britain), from ref 169. Permission conveyed through Copyright Clearance Center, Inc.

terms (or interface tensions), as well as the role of hydrodynamics.

Figure 7 illustrates how the morphology can be controlled by the initial densities, $\phi_\alpha^{(0)}$, inside the polymer film. Upon increasing the initial polymer density, Zhou and Powell observed a crossover from polymer droplets to sponge pores. The initial solvent density appeared to have only a minor effect on the morphology. Also note the lamellar morphology at the surface of the polymer film.²⁷⁴ Overall, the morphology resembles structures observed in surface-directed spinodal decomposition.^{275,276}

Whereas the Cahn–Hilliard modeling explicitly accounts for the surface of the polymer–solvent mixture with a coagulation bath and allows for transversal phase separation, it ignores hydrodynamic effects. Zhou and Powell extended their study to model H dynamics in three dimensions, finding that hydrodynamic effects tend to destabilize the dense polymer layer at the film surface.²⁷⁴ Wagner and co-workers²⁷⁷ employed two-dimensional multiphase multicomponent Lattice Boltzmann simulations to investigate asymmetric membrane formation via NIPS. Wagner et al. observed (i) that a thicker polymer skin at the film surface is formed if the viscosity contrast between polymer and nonsolvent increases and (ii) that an increase of incompatibility, χ_{PN} , between polymer and nonsolvent results in more porous structures. The study, however, only observed a little gradation of the pore sizes and attributed this effect to missing of composition-dependent mobility and dynamic arrest.

The role of hydrodynamics and dynamic asymmetry has also been explored in a sequence of papers by Tree and co-workers.^{169,183,206,278} They extended Doi and Onuki’s two-fluid model,¹⁷⁰ see section 4.3.2.3, to a ternary polymer–solvent–nonsolvent mixture, and efficiently solved the resulting PDEs by a pseudospectral technique with semi-implicit, adaptive time stepping. They studied the phase separation in the bulk, observing three characteristic growth laws of the domain size as a function of time, in agreement with the kinetics of structure formation of an unstable mixture: (i) At early times, the mixture is linearly unstable, and initial composition fluctuations with a wavevector $q < q_c$ exponentially grow in time (early stage of spinodal decomposition, cf., eq 31). The maximal growth rate

dictates the initial, characteristic length scale. In the course of spinodal decomposition, the densities saturate toward their equilibrium values in the coexisting phases, and interfaces between the polymer-rich and nonsolvent-rich phases build up. (ii) If hydrodynamics is included, the different curvatures of the interfaces give rise to differences in the Laplace pressure and, in turn, result in a power-law coarsening of the domain size, $L \approx t^\alpha$. According to Siggia,²⁷⁹ the domain growth exponent is $\alpha = 1$, and this value is compatible with the numerical data. (iii) At later times, the compositional asymmetry results in spherical domains, which coarsen according to the Lifshitz–Slyozov–Wagner theory^{280,281} with the asymptotic growth exponent, $\alpha = 1/3$. The numerical data in this intermediate regime rather yield a somewhat smaller value, $\alpha \approx 0.29$, for the regime of length and time scales accessible. Additionally, the phase separation that ensues after the mixture is brought into contact with a nonsolvent bath has been studied. The surface-directed spinodal decomposition, however, did not result in a spatially inhomogeneous domain-size distribution.¹⁸³

The same model has been employed to test the hypothesis by Matz,²⁸² and Frommer and Messalem²⁸³ that a Marangoni instability²⁸⁴ is responsible for initiating the formation of macrovoids.²⁷⁸ While the calculations did observe roll cells in the near-surface velocity field, their strength and lifetime appear to be insufficient to cause the formation of macrovoids.²⁷⁸ This finding qualitatively agrees with linear stability analysis.²⁸⁵ The calculations, however, exemplify that the interplay between fluid flow and phase separation is particularly pronounced if the initial composition of the polymer film is nearly critical.²⁷⁸ Then, the polymer film begins to immediately demix upon solvent–nonsolvent exchange.

In the opposite limit,¹⁶⁹ that the initial composition of the polymer film is well inside the one-phase region, a significant exchange of solvent and nonsolvent across the surface of the film is required to initiate phase separation; i.e., NIPS is “delayed”. In the case that the spinodal is crossed at late times, $t > \tau_{\text{mix}}$ and therefore the density profiles inside the film do not strongly vary in space, or that the initial composition is close to the critical point, a significant portion of the film becomes unstable. In three-dimensional systems, Tree and co-workers¹⁶⁹ observed

that, for initial polymer-film conditions indicated in Figure 8, phase separation proceeds as a surface-directed traveling wave, typically giving rise to a thin enrichment layer of polymer at the film surface. This is illustrated in Figure 8, additionally indicating that the microstructure is chiefly dictated by the initial polymer density, $\phi_{\text{p}}^{(0)}$. In this case, preferences at the film surface break translational and rotational symmetry and give rise to surface-directed spinodal decomposition,^{275,276} where the order propagates from the surface into the film. Without thermal fluctuations this surface-directed spinodal decomposition gives rise to alternating polymer-rich and nonsolvent-rich layers. If thermal fluctuations are included, this anisotropic surface structure competes with bulk-like spinodal decomposition and coarsening farther away from the film surface.²⁰⁶ Their simulations, however, could not provide a rationale for the formation of macrovoids or the formation of domains, whose size distribution varies perpendicular to the film surface. The authors highlighted the need to consider nucleation and growth as well as the dynamic arrest.¹⁶⁹

4.5.1.3. Moving Phase-Separation Front. Phase separation ensues in response to the exchange of solvent and nonsolvent across the film surface and the concomitant retraction of the film surface. Since the solvent is miscible with the polymer and the nonsolvent, it dilutes the incompatibility between polymer and nonsolvent. The time-dependent solvent profile, in turn, gives rise to a spatiotemporal variation of the effective incompatibility between polymer and nonsolvent (see eq 3).

Thus, Hopp-Hirschler and Nieken¹⁸² have proposed to approximately model the structure formation process by the phase separation of an effective, binary system, comprised of a polymer-rich domain, $\tilde{\text{P}}$, and a nonsolvent-rich domain, $\tilde{\text{N}}$, in a reference frame, cf., eq 27 that moves with the velocity, \mathbf{u}_{ps} , of the phase-separation front. This phase-separation front is the position at which the homogeneously mixed polymer film phase separates. The concomitant kinetic equation with a moving phase-separation front can be numerically studied via Lattice Boltzmann simulations,^{180,181,277} and Hopp-Hirschler and Nieken used smoothed particle hydrodynamics.¹⁸² Such a moving phase-separation front gives rise to structures that physically resemble Liesegang patterns.^{180,181}

A diagram of morphologies between the moving phase-separation front and the film surface as a function of the velocity, u_{ps} , of the phase-separation front and the initial composition $\phi_{\text{p}}^{(0)}$ in the polymer film has been obtained by two-dimensional calculations and is depicted in Figure 9. The results are in accord with those observed in the wake of an enslaved phase-separation front of a Cahn–Hilliard square-gradient model.¹⁸¹

Different morphologies can be distinguished: (i) Sponge pores occur by macrophase separation at rather large polymer density and small speed, u_{ps} , of the phase-separation front. These unconnected, polymer-poor domains (pores) are created by nucleation and growth (or spinodal decomposition). An increase of the speed of the phase-separation front tends to decrease the initial pore size. Eventually, a pore-size distribution is established by Ostwald ripening. In a model that accounts for the arrest of the phase-separation kinetics, e.g., by density-dependent Onsager coefficients, the growth of the pores will be stopped. (ii) If the polymer density is smaller, pores tend to elongate perpendicular to the phase-separation front and do not detach from the moving front. This gives rise to morphologies that resemble finger pores or macrovoids, as illustrated in Figure 9. (iii) If the speed of the phase-separation front is large and $\phi_{\text{p}}^{(0)}$ is not too close to unity, lamellar structures are observed, where

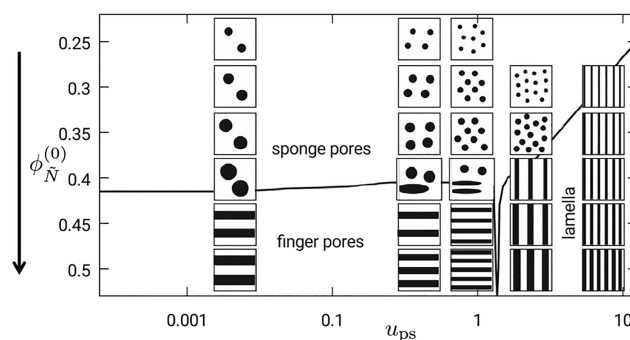


Figure 9. Diagram of morphologies as a function of the speed, u_{ps} , of the phase-separation front and the initial composition, $\phi_{\text{p}}^{(0)} = \phi_{\text{N}}^{(0)} + \phi_{\text{S}}^{(0)}/2$, of the homogeneous polymer film. Black domains stand for nonsolvent-rich pores, whereas white domains represent the polymer-rich phase. Adapted with permission from ref 182. Copyright 2018 Elsevier.

elongated pores parallel to the phase-separation front are formed. The latter structure—layers—exhibits a one-dimensional variation of the density and has been analytically analyzed by Foard and Wagner.¹⁸⁰ The latter study demonstrates that the front velocity, u_{ps} , should be compared to the wavelength and inverse of the maximal growth rate of spinodal phase separation (see eq 31). For a discussion of the general aspects of front propagation into unstable systems, we refer the reader to the review of van Saarloos.²⁸⁶

4.5.1.4. Viscoelastic Phase Separation and Dynamic Arrest. One possibility to address dynamic asymmetry between components and the dynamic arrest of structure formation consists of modeling NIPS as viscoelastic phase separation. The importance of viscoelasticity on macrovoid formation⁸³ has also been emphasized by experiments, cf. Figure 5. Viscoelastic phase separation does not assume that the elementary molecular dynamics is much faster than the kinetics of the morphology and explicitly accounts for the slowly relaxing polymer conformations. The latter is particular important for polymers of high molecular weight that are entangled. In Figure 10, we illustrate

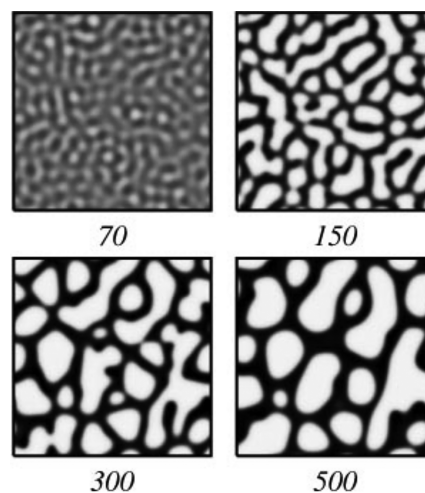


Figure 10. Gel-like morphologies in the course of viscoelastic phase separation in a binary polymer–solvent mixture. The average volume fraction of the polymer exceeds the polymer fraction at the critical point by a factor 2.5. Polymer domains are colored dark, whereas solvent-rich domains are depicted in white. The numbers denote the time after the quench into the miscibility gap. Reprinted figure with permission from ref 195. Copyright 1996 by the American Physical Society.

the qualitative consequences of viscoelasticity for a binary mixture in the bulk. The two-dimensional calculations show that the viscoelastic component (polymer) may form a continuous matrix, although it is the minority component by volume fraction. Such a gel-like morphology is rather typical for membranes formed by NIPS. This viscoelastic model has recently been generalized to ternary mixtures of polymer, solvent, and nonsolvent.²⁸⁷

An alternative strategy to account for the slowing down of the kinetics of structure formation in regions of high polymer density consists of employing density-dependent Onsager coefficients. Tree and co-workers²⁰⁶ employed this technique to model the dynamic arrest upon increase of the polymer density. In this case, there are two time-dependent characteristic positions: (i) the phase-separation front, at which the homogeneous state starts to phase-separate and, additionally, (ii) a glass-transition front, at which the polymer density becomes so high that the structural evolution arrests. Thermal fluctuations introduce perforations in the dense polymer skin, through which the nonsolvent enters the film, whereas the dense portions of the film surface act as a barrier to nonsolvent entry.²⁰⁶ Thus, the phase-separation front moves faster than the glass-transition front, and the morphology in the region next to the film surface has less time to phase-separate and coarsen than the morphology deeper inside the polymer film. The gradient in the coarsening time from the film surface toward the substrate gives rise to an asymmetric pore-size distribution; i.e., smaller pores are formed close to the film surface, whereas slightly larger pore sizes occur closer to the substrate.²⁰⁶

4.5.2. Particle Simulations. One of the first simulation studies of NIPS employed kinetic MC simulations of a two-dimensional lattice model. A lattice site corresponds to a volume element with a linear extent of about 20 nm that can be either occupied by polymer, solvent, or nonsolvent.^{288–290} A spatially extended coagulation bath is represented by “alchemically mutating” solvent particles into nonsolvent ones, if they have diffused a predetermined distance into the coagulation bath. Termonia observed that the fast solvent–nonsolvent exchange at the film surface results in a formation of a polymer skin at the film surface. This skin is transversely inhomogeneous in thickness, and these inhomogeneities will initiate the formation of finger-like pores. The fingers diffusively grow into the polymer film because the solvent can leave the film faster through the finger-like pore than across the dense polymer skin. The mechanism resembles the viscous fingering instability of a low-viscosity fluid (nonsolvent) injected into a high-viscosity fluid (polymer–solvent film).^{193,194} Upon increasing the solvent–nonsolvent immiscibility, χ_{SN} , Termonia observed a decrease of diffusive motion of the phase-separation front and a crossover from droplet-like polymer precipitates (dust-like structures), via finger-like pores, to sponge-like structures (spherical pores), as illustrated in Figure 11. A decrease of incompatibility between polymer and nonsolvent or the addition of solvent to the coagulation bath, in turn, slows down the phase-separation front, disfavors the formation of a polymer skin, and adverts finger-like pores.²⁸⁹ A similar model has also been applied to the process of wet spinning,²⁹¹ and it has additionally been employed to study the role of initial dispersion of the polymer in the solvent, indicating that formation of polymer clusters in the solvent-swollen film results in a faster coagulation rate and a more uniform, cellular-like structure.²⁹²

He and co-workers used the two-dimensional, single-site, bond-fluctuation model to study immersion precipitation.²⁹³

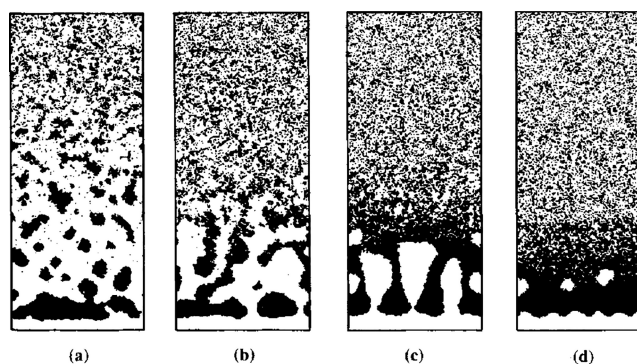


Figure 11. (a–d) Effect of solvent–nonsolvent incompatibility, χ_{SN} , on the morphology obtained by lattice simulation of NIPS. As χ_{SN} increases from left to right, the morphology changes from droplet-like polymer precipitates to finger-like pores to sponge-like structures. Reprinted from ref 289 with permission of John Wiley and Sons.

The model affords a somewhat more detailed description of the polymer than the lattice model of Termonia.²⁸⁸ Their study suggests that phase separation at the surface of the polymer film predominantly proceeds via spinodal decomposition, whereas nucleation and growth become important deeper inside the polymer film.

Soft, highly coarse-grained models have been employed to study membrane formation by TIPS²⁹⁴ and NIPS.^{235,295–297} The DPD simulations show the formation of a thick, dense surface layer (polymer skin) in NIPS.²⁹⁶ As solvent and nonsolvent become more miscible, i.e., χ_{SN} decreases, the rate of mass exchange across the film surface increases, and a thicker and denser surface layer is initially formed. The change of morphology, however, is much less pronounced than in the study of Termonia²⁸⁸ possibly because the variation of χ_{SN} is smaller. This study also observed an increase of the average polymer domain size with the initial polymer density in the film.²⁹⁶ This observation is corroborated in ref 235 that additionally shows that pore sizes differ in the dense polymer skin and farther inside the polymer film and that the pore-size distribution becomes narrower upon an increase of the initial polymer density. An increase of the polymer length (at fixed polymer volume fraction) slightly increases the polymer density in the skin layer and leads to a somewhat larger average pore size.

5. BLOCK COPOLYMER MEMBRANES

Because of their self-assembly into regularly ordered microphase-separated structures, tailor-made block copolymers have been considered to be useful candidates for membrane applications for a long time. The first successful attempt to combine block copolymer self-assembly into a regularly ordered morphology and formation of an integral-asymmetric structure was reported as the example of a polystyrene-*block*-poly(4-vinylpyridine) (PS-*block*-P4VP) diblock copolymer,²⁶ which formed P4VP spheres in a PS matrix in the bulk state, when cast from a rather nonselective solvent (chloroform).

Membrane preparation followed a two-step procedure: First, the diblock copolymer was cast from solution in a mixed solvent of tetrahydrofuran (THF, very volatile and more selective for PS) and dimethylformamide (DMF, less volatile and more selective for P4VP). After casting, mainly THF evaporates and induces microphase separation with a more concentrated PS matrix around very swollen P4VP domains, as DMF has a low volatility. The partial solvent evaporation results in the

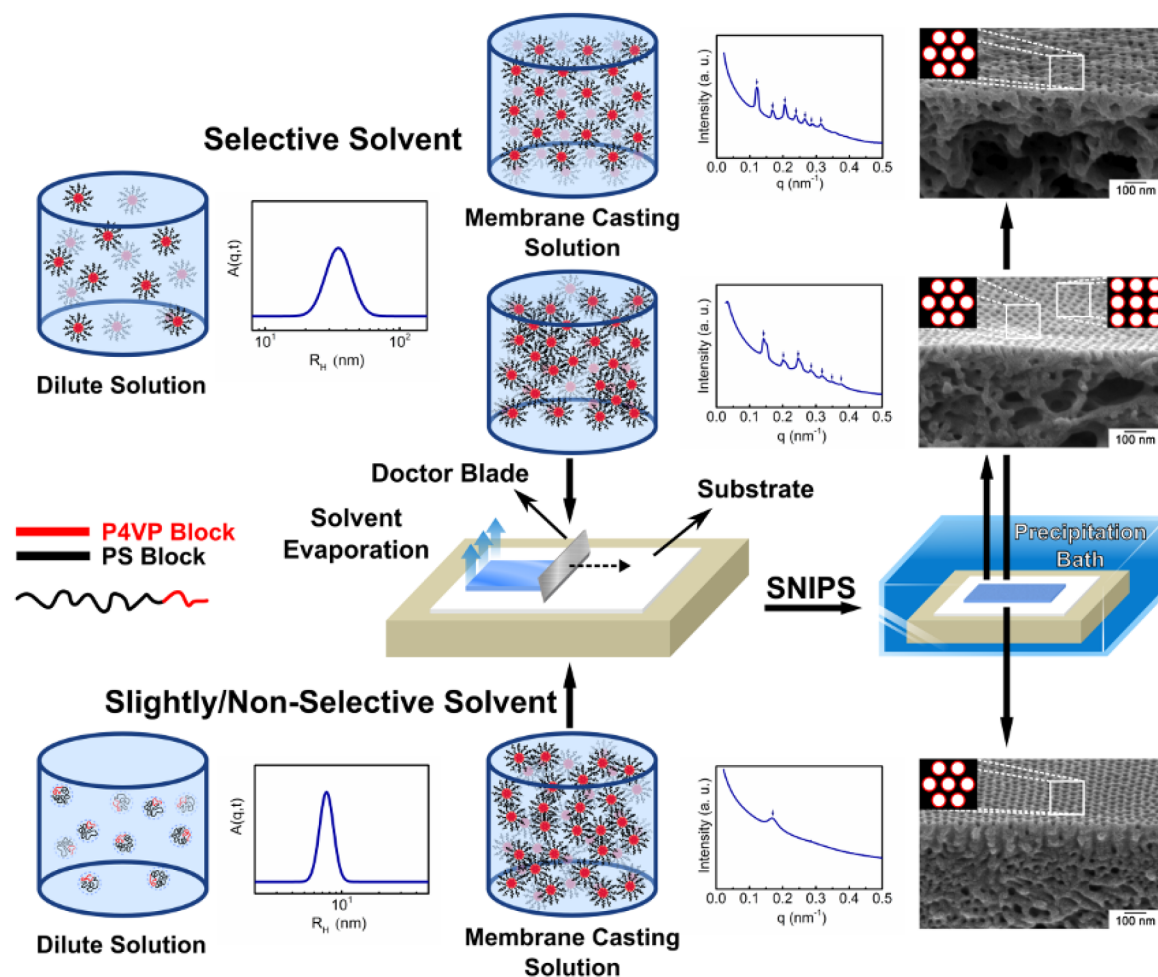


Figure 12. Schematics of the structure formation of a polystyrene-*block*-poly(4-vinylpyridine) block copolymer in a selective (top) or less/nonselective solvent (bottom). In dilute solution, the block copolymer dissolves as micelles (top) or unimers (bottom), as indicated by dynamic light scattering measurements, measuring the hydrodynamic radius. At higher density, these micelles order into a superlattice in the case of a selective solvent (top) or weakly ordered micelles (bottom), as shown by SAXS measurements. After precipitation, integral-asymmetric membranes are obtained with an isoporous surface but different cross-sectional structures. Reprinted with permission from ref 84. Copyright 2017 American Chemical Society.

formation of cylindrical pores at the membranes surface on top of a spongy substructure.

The subsequent exchange of solvent by nonsolvent occurs largely through these highly swollen P4VP domains, and thus leads to an open porous structure. In the depth of the membrane, there is no long-range ordered microphase-separated structure, as the precipitation of the block copolymer happens before the microphase separation occurs,^{26,84,298} as shown in Figure 12. This initial result stimulated many more works on this type of isoporous, integral-asymmetric block copolymer membrane in the following decade. Most of the papers deal with PS-*block*-P4VP. Besides the successful preparation of flat-sheet membranes by casting, spraying was successfully demonstrated, too,²⁹⁹ and also hollow-fiber membranes could be successfully spun, both with the isoporous structure outside^{300–304} and inside the fiber.³⁰⁵ Even coating the inside of a porous fiber with a PS-*block*-P4VP solution followed by evaporation and NIPS can be done.³⁰⁶ The reason to choose this diblock copolymer is the very strong segmental incompatibility between PS and P4VP, without any complications due to specific interactions or crystallization.²⁹⁸ The first systematic study of the influence of molecular weight, composition of the block copolymer, and its density in the casting solution was published seven years after

the first discovery.³⁰⁷ The main result of that work is a linear relationship between pore size and molecular weight of the diblock copolymer, indicating the possibility that the pore size can be designed by tailoring the molecular weight. This strategy was confirmed by another experimental result that showed the possibility to tailor the pore size by blending two PS-*block*-P4VP copolymers with different molecular weights or compositions.³⁰⁸ Besides the amphiphilic PS-*block*-P4VP diblock copolymer, integral-asymmetric membranes with rather isoporous surfaces were also prepared from a number of other diblock and triblock copolymers.^{27,28}

In addition to these characteristics—incompatibility, χ_{AB} , between the blocks and molecular weight, N , of the polymer—that dictate the equilibrium morphology, the fabrication process that directs the kinetics of structure formation is important in block copolymer membranes. In the previous section, we presented theoretical concepts to model various aspects of structure formation in homopolymer membranes. Much less theoretical work has been done in the area of block copolymer membranes, where in addition to macrophase separation between polymer and nonsolvent also microphase separation within the block copolymer must be considered. Experiments, however, suggest that to a first, crude approximation, micro-

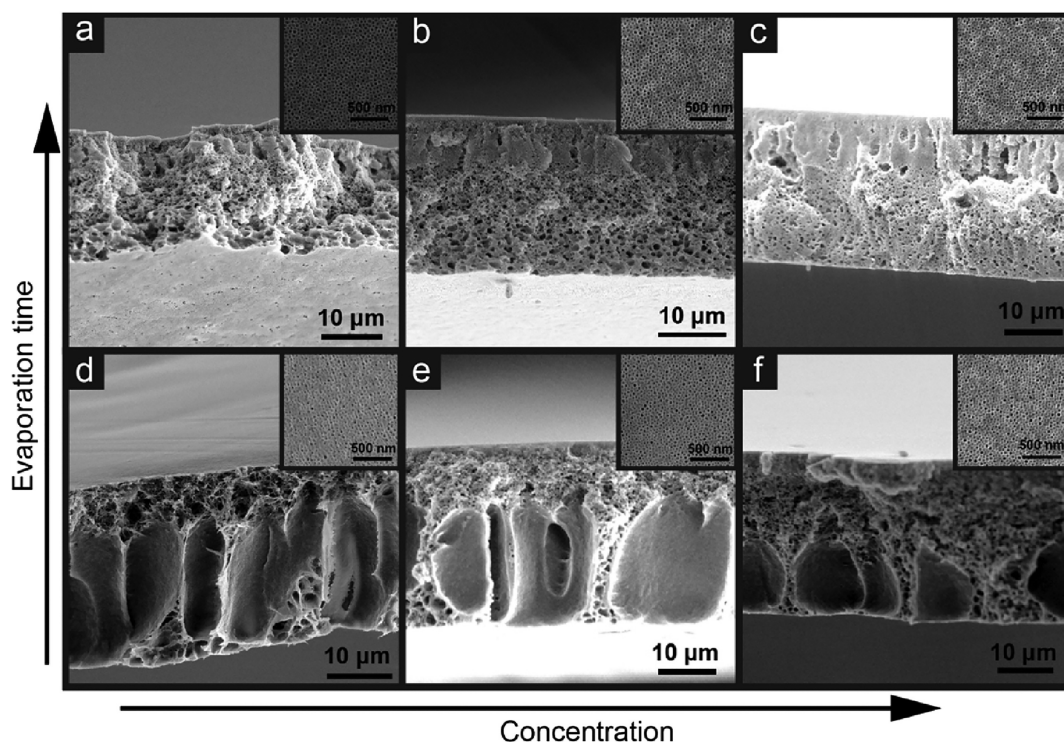


Figure 13. SEM images of cross-sections and top surfaces (inset images) of polyisoprene-*block*-polystyrene-*block*-poly(4-vinylpyridine) membranes cast from a solution in DOX/THF (5/5). (a, d) 9 wt %, (b, e) 10 wt %, and (c, f) 11 wt %. Evaporation times of (a–c) are 60 s and of (d–f) are 45 s, before immersion into water. Short evaporation times lead to macrovoid formation, and higher densities hinder the formation of macrovoids. As the block copolymer has a molecular weight above the entanglement molecular weight of the matrix-forming blocks (polyisoprene-*block*-polystyrene), macrovoid formation is hindered above a certain density, as discussed before for homopolymers (compare with Figure 3). The longer evaporation time gives rise to an increase of polymer density, leading also to the suppression of macrovoids. Reprinted with permission from ref 309. Copyright 2016 Elsevier.

phase separation of the copolymer blocks into an ordered structure and macrophase separation between the (co)polymer and the nonsolvent can be considered as decoupled phenomena. The former is typically initiated during the evaporation step, whereas the latter ensues after the immersion into the coagulation bath as discussed in section 4. The microphase separation, which is most relevant for the final membrane structure, occurs at the film surface or top layer of the membrane, whereas the structure underneath can be approximately treated as a block copolymer without forming a long-range ordered microphase structure during solvent–nonsolvent exchange. We first report on investigations of the substructure in integral-asymmetric block copolymer membranes, before we consider the parameters influencing the microphase-separated surface structure.

5.1. Substructure of Isoporous Integral-Asymmetric Membranes

Two main features are observed in the cross-sectional morphology of phase-inversion membranes: sponge-like pores or finger-like macrovoids. A sponge-like substructure may be mechanically more robust, whereas a substructure with finger-like pores (macrovoids) may allow for higher membrane fluxes. For NIPS membranes prepared from homopolymers, experimental results are shown in Figure 3 in section 4.

Zhang et al. studied polyisoprene-*block*-polystyrene-*block*-poly(4-vinylpyridine) (PI-*block*-PS-*block*-P4VP) triblock terpolymers with molecular weights above 100 kDa in 1,4-dioxane (DOX)/THF mixtures and found that small polymer densities and short evaporation times predominantly resulted in a

substructure with macrovoids, whereas an increase of evaporation time leads to a more sponge-like substructure, as shown in Figure 13. At higher densities of the casting solution, sponge-like structures are more favored compared to lower densities of the casting solution at similar evaporation times.³⁰⁹ For a given polymer density and a given evaporation time prior to precipitation, increasing the amount of the lower-volatile solvent increased macrovoid formation. This effect may be attributed to a faster phase-separation front, progressing into the solvent-swollen polymer film because a lower polymer density at the surface facilitates the solvent–nonsolvent exchange, cf. Figure 13. This seems to be in line with the observations of integral-asymmetric homopolymer membranes, indicating that the microphase separation in the block copolymer does not (or only weakly) influence the substructure formation. The latter appears to be chiefly driven by the macrophase separation due to the solvent–nonsolvent exchange and viscoelastic effects of the (entangled) polymer.

Therefore, in the next subsections, we focus on the parameters influencing the self-assembled microphase-separated surface morphology.

5.2. Influence of Solvent Quality and Selectivity on the Formation of an Isoporous Film Surface

For successful preparation of block copolymer membranes, a careful choice of solvents is required. Mostly mixtures of two and sometimes more solvents with appropriate selectivities for the different blocks were required to obtain an open porous membrane surface. Beneficial is a low volatility of the solvent more selective for the pore-forming block compared to the

solvents that are selective for the matrix-forming block. The main challenge in phase-inversion membranes obtained from block copolymers is the formation of the regular isoporous surface morphology, and therefore many works address the question of which parameters are controlling the surface structure. As the choice of solvent or solvent mixtures is very important, Sutisna et al. studied several polystyrene-*block*-poly(2-vinylpyridine) (PS-*block*-P2VP) and polystyrene-*block*-poly(2-vinylpyridine)-*block*-poly(ethylene oxide) (PS-*block*-P2VP-*block*-PEO) block copolymers in different solvents and solvent mixtures.³¹⁰ They calculated the product of the interaction parameter of a block with the solvent, $\chi_{SA}N_A$ and $\chi_{BS}N_B$, with $N_A = fN$ and $N_B = (1 - f)N$ being the degree of polymerization of the respective blocks, using tabled solubility parameters. The difference of this product for the less soluble block and the more soluble block (the latter one being the minority block, envisioned to form the pores) was normalized to the $\chi_{AB}N$ of the block copolymer in the bulk melt to quantify the preference of the film surface for one of the blocks. For the investigated membrane systems with the desired surface structure, the normalized values turned out to follow a third-order polynomial of the volume ratio $V_A/V_B = f/(1 - f)$; see Figure 14. If another solvent was chosen leading to another

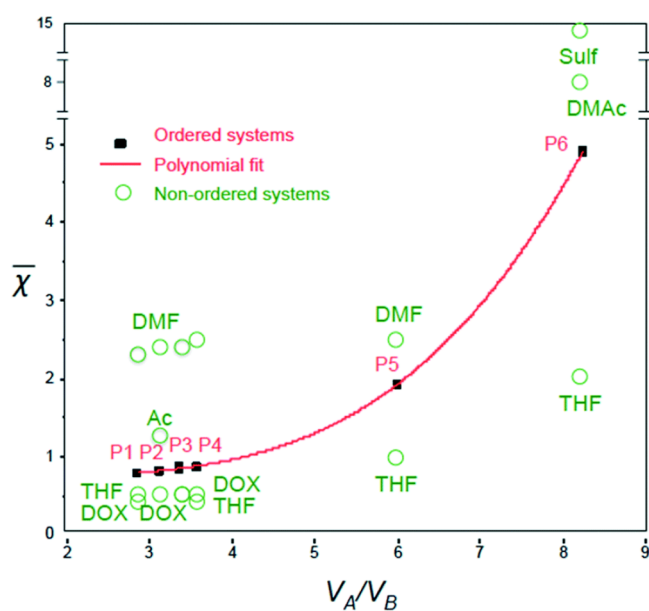


Figure 14. Trend line (following a third-order polynomial) showing a normalized segmental interaction contrast, $\bar{\chi} \equiv \frac{\chi_{AS}N_A - \chi_{BS}N_B}{\chi_{AB}N}$, between the A and B blocks of a diblock copolymer and the solvent as a function of the ratio of the volumes of the less soluble block A to the more soluble block B. Republished with permission of the Royal Society of Chemistry (Great Britain), from ref 310. Permission conveyed through Copyright Clearance Center, Inc.

normalized interaction parameter, no membranes with the desired isoporous structure could be obtained.³¹⁰ In this approach, however, the effects of polymer density and evaporation time prior to precipitation of the cast film are not considered. As the different solvents evaporate at different rates, the actual solvent composition at the onset of structure formation is unknown in this study.

5.3. Influence of Solvent Evaporation Rate and Time

From many experiments, it is known that the time of evaporation prior to freezing the solution film by precipitation in the coagulant is an important parameter. Russell and co-workers reported on thin films of cylinder-forming polystyrene-*block*-poly(ethylene oxide) (PS-*block*-PEO) block copolymer, where the PEO cylinders were oriented perpendicular to the substrate. This orientation was explained by the density gradient built up during the evaporation of the solvent, as the microphase separation started at the top of the film surface. The solvent gradually left the polymer film during evaporation, and, thus, an ordering front moved downward into the film as the polymer density of the disordered block copolymer solution reached the threshold, where microphase separation occurs due to lack of the screening of AB repulsion by the solvent, as illustrated in Figure 15.⁹²

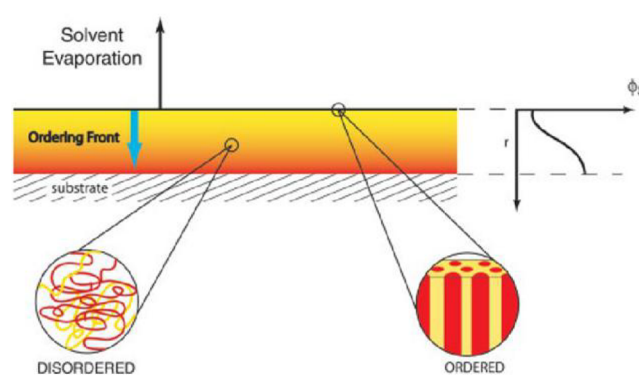


Figure 15. Schematic diagram of solvent evaporation from a thin block copolymer film. At the surface, the solvent density is lowest, and the copolymer undergoes microphase separation. A gradient in the solvent density, as a function of depth, r , is established normal to the film surface with the solvent density increasing with depth. This increase in solvent density leaves the copolymer disordered in the interior of the film. As the solvent evaporates, an ordering front propagates through the film, akin to zone refinement, producing a highly ordered and oriented array of cylindrical microdomains in the film. Reprinted from ref 92 with permission by John Wiley and Sons.

Additionally, the evaporation speed of the solvent plays a crucial role in the orientation of the microdomains, as was shown on the example of polystyrene-*block*-poly(lactide) (PS-*block*-PLA) dissolved in toluene. Figure 16 shows that a slow evaporation led to a parallel alignment of the cylindrical microdomains at the surface, whereas a fast removal of the solvent resulted in a perpendicular orientation.⁸⁸ As in this case the film thickness was several micrometers, the order at the surface transformed into a sponge-like substructure.

For a given mixture of a highly volatile, PS-matrix-selective solvent, tetrahydrofuran (THF), and a very low volatile solvent, dimethylformamide (DMF), that is selective for the pore-forming P2VP block, the evaporation-driven density change in a solution film was calculated from evaporation experiments by Stegelmeier et al.²⁶⁵ Plotting the volume fractions of all components, i.e., block copolymer and the two different solvents, as a function of the logarithm of time in Figure 17, it was found that the appropriate time when the system should be quenched into the coagulation bath is the region where a strong decrease of the THF density and therefore strong increase of the densities of the other components are observed.

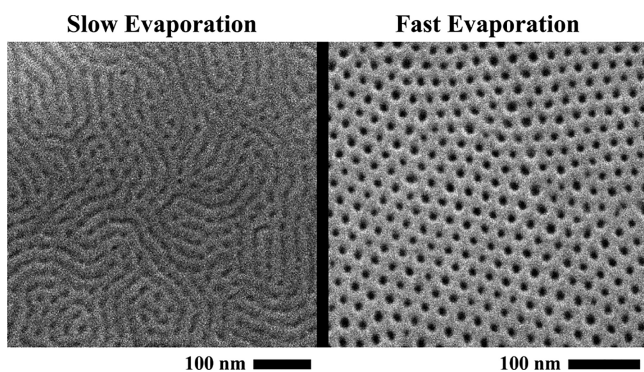


Figure 16. SEM micrographs of the top surface of polystyrene-*block*-poly(lactide) thin films obtained by casting an 8 wt % solution on a porous support and letting it dry slowly (2 h), leading to parallel alignment of the PLA cylinders, or fast (5 min), resulting in perpendicularly aligned cylinders. The final membrane thickness of the block copolymer layer is 4 μm . Reprinted with permission from ref 88. Copyright 2010 American Chemical Society.

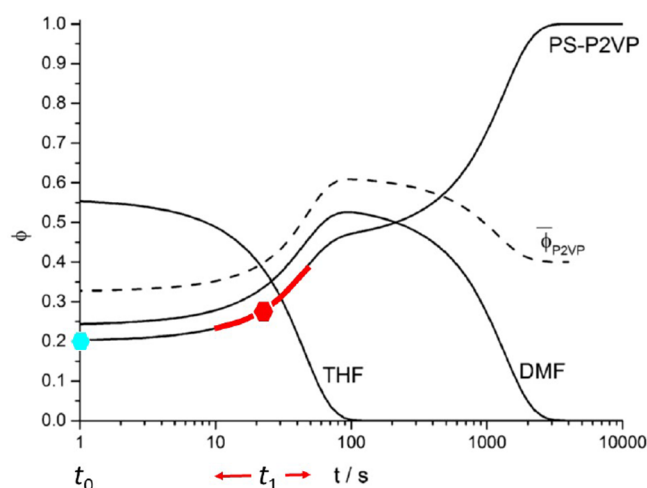


Figure 17. Time evolution of a polystyrene-*block*-poly(2-vinylpyridine) diblock copolymer and solvent densities during the evaporation. The cyan hexagon indicates the block copolymer density in the initial casting solution, and the red hexagon indicates the composition at the time, t_1 , when the cast film should be brought in contact with the coagulant to achieve the desired membrane structure with an isoporous surface. The red line and arrow indicate the suitable range of block copolymer density and evaporation time. Adapted with permission from ref 265. Copyright 2014 American Chemical Society.

In that work also trajectories of the effective volume fractions of the pore-forming block and the whole block copolymer were calculated as a function of evaporation time, using swelling ratios calculated from the intrinsic viscosities of the individual blocks in the different pure solvents. These swelling ratios change with the solvent composition due to the different evaporation rates of THF and DMF. The cast solvent-swollen polymer films were quenched in water after different times, and the film surfaces were investigated by AFM. Starting from a THF-rich solution, a too short evaporation time led to a loose spinodal network, whereas a too long evaporation time (high DMF and polymer density) led to a cylindrical structure at the film surface. An intermediate evaporation time before quenching led to the desired structure of standing pores. This corresponds to the time region where a significant reduction of THF density is observed on the logarithmic time scale. Using a controlled flow of nitrogen

above cast solutions of PS-*block*-P4VP, it was shown that the range of polymer density and the range of evaporation time can be significantly enlarged to lower polymer densities and shorter evaporation times compared to normal conditions, without affecting the pore size and order of the resulting membranes.³¹¹

5.4. Self-Assembly in the Casting Solution

Changes of solvent composition and density in the casting solution also modulate the self-assembly of the block copolymer, leading from dissolved unimers in dilute solution via micelles in a less dilute solution to a microphase-separated bulk-like structure in a semidilute or concentrated solution. This leads to the important question if a block copolymer should already self-assemble into an ordered structure in the casting solution or if the block copolymer should still remain in the disordered state when being quenched in the coagulation bath. In several studies, it was stated that the casting solution already exhibits a significant level of self-assembly into ordered structures before the quenching process in order to achieve the desired, well-organized pore structure at the film surface after precipitation.^{35,312} In these studies, self-assembly into ordered structures of the casting block copolymer solution was observed by SAXS, such as a hexagonal structure for PS-*block*-P4VP and a cubic structure for PI-*block*-PS-*block*-P4VP.^{35,312} The presence of additives in PS-*block*-P4VP solutions, such as copper or magnesium salts, which may selectively interact with the P4VP units by forming complexes between the cation and the nitrogen atom,^{313,314} and organic molecules offering hydrogen bonds to the basic 4VP units, was shown to support the formation of the desired membrane morphology.^{315,316} The effect of additives is already observed in the casting solutions by an increase of viscosity, and it allows the use of lower densities of the block copolymer in the casting solution, thereby reducing the required amount of block copolymer for membrane formation.

Using different solvents and solvent mixtures as well as varying the density of PS-*block*-P4VP led to the conclusion that membranes with an isoporous surface structure can be obtained from rather strongly ordered solutions, but better structures are obtained from weakly ordered or disordered solutions.⁸⁴ This follows from SAXS studies of the casting solutions, shown in Figure 18, and SEM images of finally obtained membranes, presented in Figure 19. Also a study of the formation of integral-asymmetric PS-*block*-PEO block copolymer membranes led to the conclusion that a solvent mixture close to the transition, where micelles are formed, is beneficial for the successful formation of a membrane with a well-organized surface structure.³¹⁷

The question of whether micelles are already formed in the casting solution, or not, or there are only weakly organized micelles in the casting solution was mostly studied for PS-*block*-P4VP block copolymers. The formation of micelles in this system seems to largely depend on the presence of DOX as one of the cosolvents in the solvent mixture of the casting solutions. It was observed that PS-*block*-P4VP block copolymers self-assemble already at very low polymer densities (a few %) in DOX and form a highly organized structure in solution, as shown in Figure 18.³⁴ Also previous SAXS studies clearly showed that the block copolymer solutions with DOX as a cosolvent displayed a very well-defined structure.³¹⁸ This agrees with the observation that very low densities of PS-*block*-P4VP copolymer in DOX are sufficient to prepare isoporous integral-asymmetric membrane, although viscosity is low.^{299,306,319}

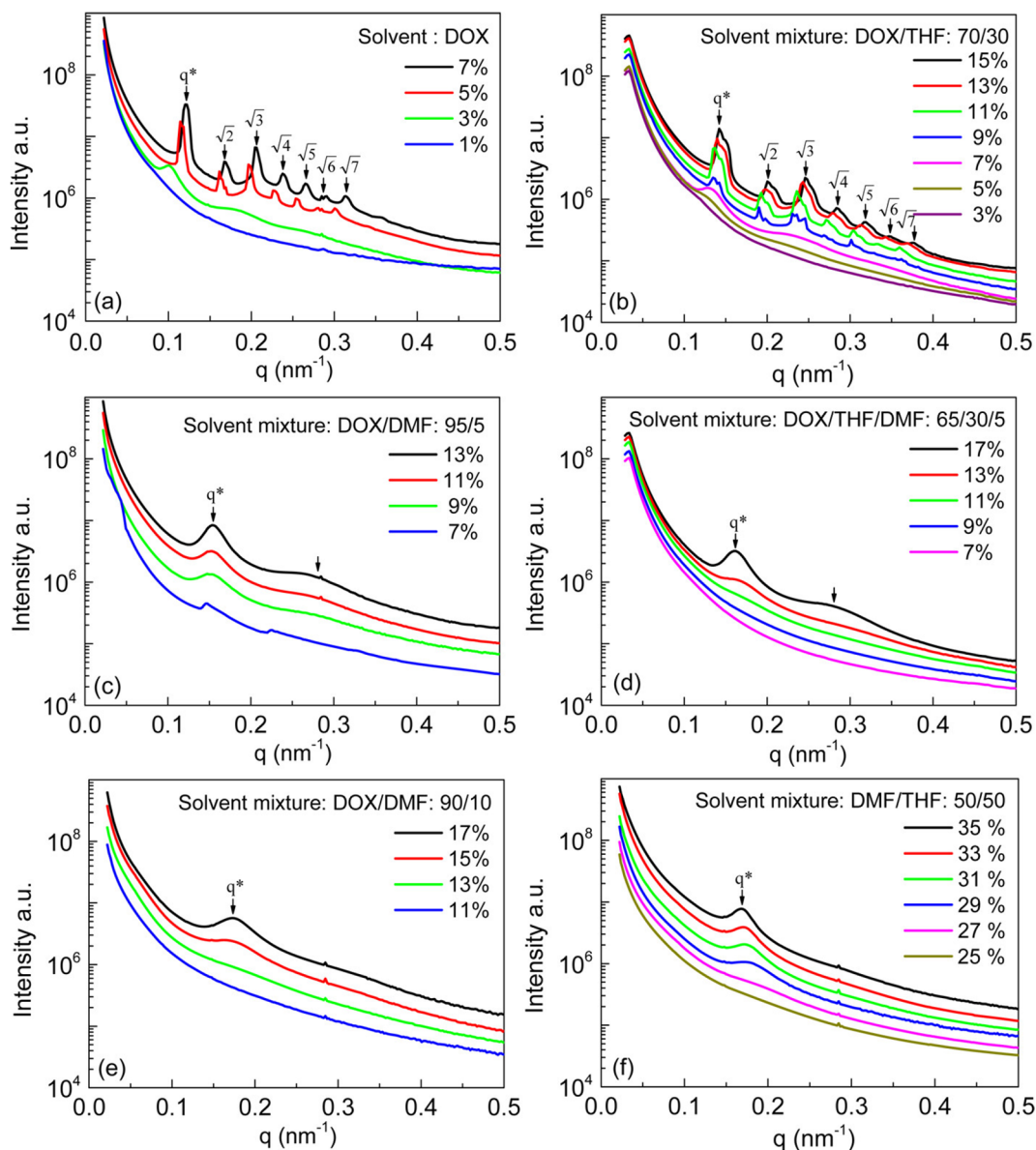


Figure 18. SAXS patterns of polystyrene-*block*-poly(4-vinylpyridine) solutions at varying concentrations in (a) DOX, (b) DOX/THF: 70/30 (w/w), (c) DOX/DMF: 95/5 (w/w), (d) DOX/THF/DMF: 65/30/5 (w/w/w), (e) DOX/DMF: 90/10 (w/w), and (f) DMF/THF: 50/50 (w/w). The intensity curves are vertically shifted to avoid overlapping. The arrows correspond to the peak positions $(q/q^*)^2 = 1, 2, 3, 4, 5, 6,$ and 7 present a BCC lattice. Reprinted with permission from ref 84. Copyright 2017 American Chemical Society.

In some studies, it was argued that crew-cut micelles are formed in the casting solution, where the short block that finally builds the pore interior forms the micelle corona, and the finally matrix-forming block forms the micelle core. This interpretation was mainly based on studies by SAXS and electron microscopy^{312,313} as well as on DPD simulations in conjunction with SAXS.³¹⁸ Opposite interpretations were given on comparable systems, mainly PS-*block*-P4VP, based on SANS, cryo-TEM, and cryo-SEM²⁹ and also dynamic light scattering and SAXS.⁸⁴ These studies show that the finally pore-forming block also forms the core of weakly organized micelles, as depicted in Figure 12. Oss-Ronen et al. carefully analyzed cryo-TEM data and took advantage of the different sensitivities of the P4VP and PS blocks toward electron-beam damage, concluding that P4VP forms the core of micelles in the casting solution. The same conclusion was reached by a SANS study of block copolymer micelles in more dilute, mixed DMF/THF solutions

that took advantage of contrast matching.²⁹ In a more recent study, this question was addressed also with NMR-relaxation spectroscopy, and it was concluded that P4VP blocks form the core of micelles in mixed solvents of DMF and DOX, as DMF preferentially swells the P4VP cores.³²⁰ The interpretation of normal (hairy) micelles, in which the longer block forms the corona, also appears to be in less conflict with the often observed, hexagonal packing of pores. In the case of crew-cut micelles being in the casting solution, the formation of the final membrane structure with the short blocks forming pores would necessitate an inversion of the curvature of the internal AB interface from convex to concave.²⁹⁸

5.5. Time-Resolved Studies of the Membrane-Structure Formation

To provide information about the kinetics of structure formation in the course of solvent evaporation from copolymer

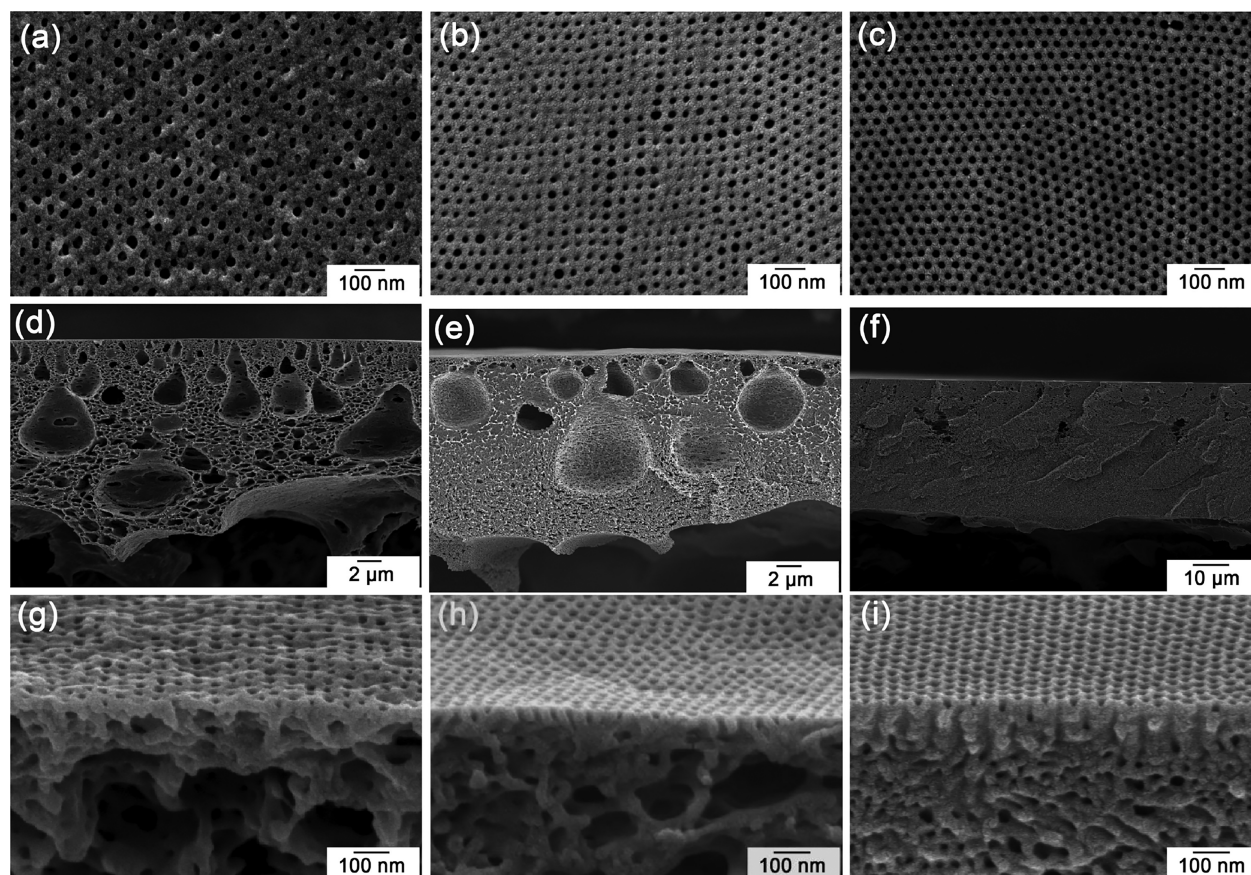


Figure 19. SEM micrographs of the top surface (top row), cross-section (middle row), and cross-section close to the top surface (bottom row) of polystyrene-*block*-poly(4-vinylpyridine) membranes cast from different solutions at different evaporation times; (a, d, g) 9 wt % in DOX 40 s, (b, e, h) 15 wt % in DOX/THF: 70/30 (w/w) 10 s, and (c, f, i) 33 wt % in DMF/THF: 50/50 (w/w) 5 s. Reprinted with permission from ref 84. Copyright 2017 American Chemical Society.

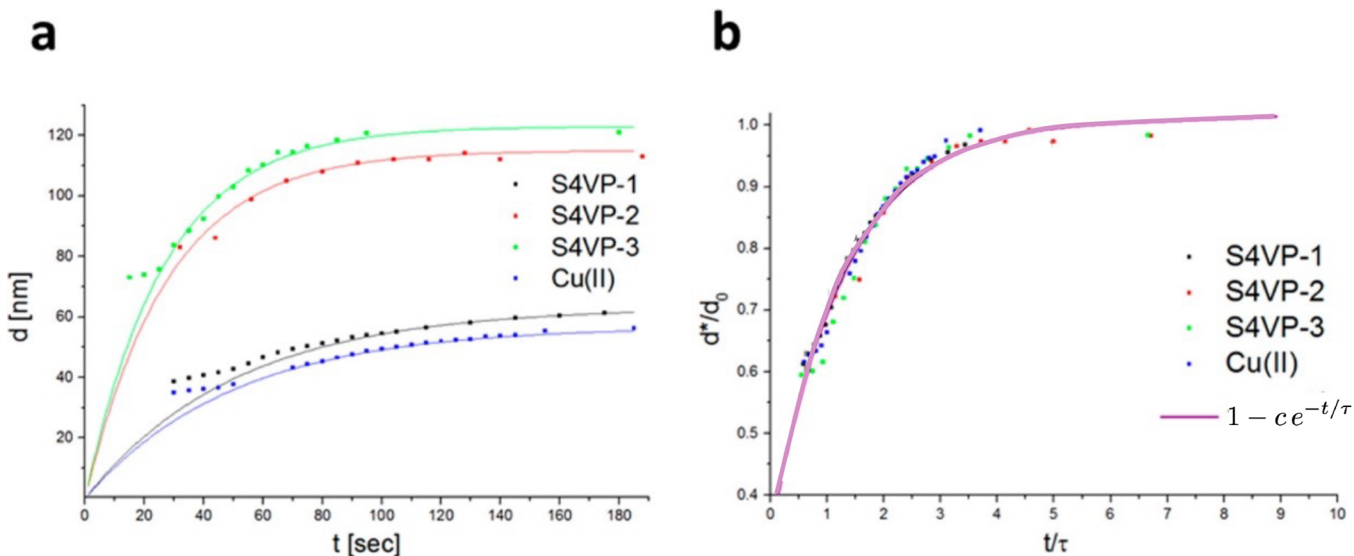


Figure 20. (a) Characteristic length scales during evaporation as a function of time for the three polystyrene-*block*-poly(4-vinylpyridine) block copolymers S4VP-1, S4VP-2, S4VP-3, and a block copolymer/salt-system S4VP-1/Cu(II). Solid lines indicate fits to a simple exponential saturation curve, (b) the same data, rescaled to a reduced time and a reduced length scale showing the common behavior of all investigated block copolymer systems. Adapted with permission from ref 321. Copyright 2015 American Chemical Society.

films, time-resolved studies were carried out. Using GISAXS, Marques et al. detected hexagonal order at the surface of a PS-*block*-P4VP solution in mixed solvents containing dioxane.³¹

Extending the study to PI-*block*-PS-*block*-P4VP triblock terpolymers of different molecular weights and densities, the authors observed a sequence of morphologies during solvent

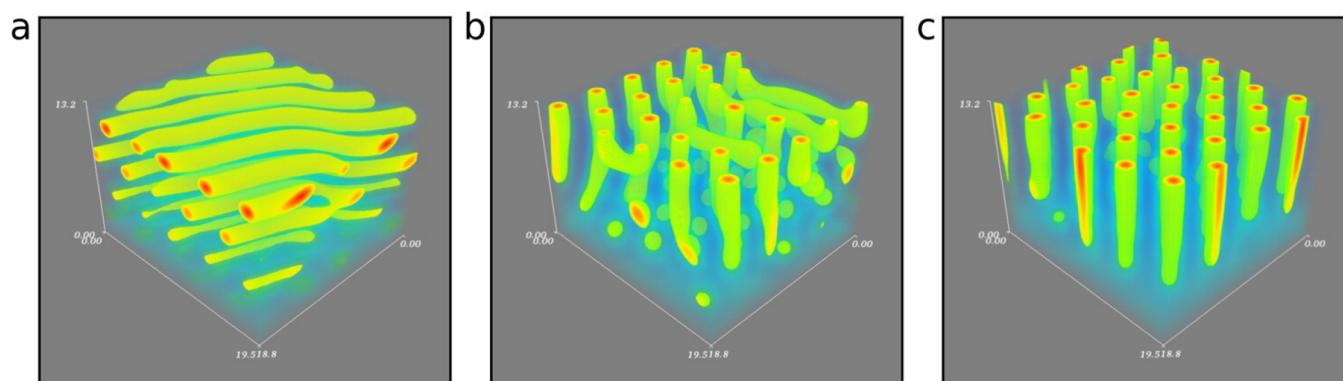


Figure 21. (a–c) D-SCFT of solvent evaporation from a solvent-swollen asymmetric diblock copolymer film, $f = 0.3$. The initial solvent fraction is $\phi_S^{(0)} = 0.9$. The solvent quality for the majority block B increases from left to right, $\Delta\chi_S N = \chi_{AS} N - \chi_{BS} N = -7, 0,$ and 7 , and results in a transition from parallel to perpendicular cylinders. Reprinted from ref 262. Copyright 2014 American Chemical Society.

evaporation from a solution containing a block copolymer with lower molecular weight, which was interpreted as a transition from an originally formed body-centered-cubic (BCC) to a simple-cubic (SC) lattice. The simple-cubic structure of the film surface is in agreement with the square-like surface symmetry of these membranes, which is caused by microphase separation of the PI block from the PS matrix at some stage of structure formation.³⁵ While GISAXS is mainly sensitive to the film surface and some part below, depending on the angle of incidence, SAXS across the sample provides information about the whole sample. Time-resolved SAXS studies were carried out on PS-*block*-P2VP solutions in DMF/THF by Stegelmeier et al.³²¹ They observed the first appearance of a scattering peak after a few seconds, which grows in intensity and moves toward smaller scattering angles. This was explained by an increased chain stretching as a result of increased microphase segregation strength, mainly caused by the disappearance of the volatile THF. After a short initial transient period, the time evolution of the peak position in Figure 20a relaxes exponentially toward its equilibrium value.

The same kinetics of the peak position is also observed with added copper salt, and all experiments can be collapsed onto an exponential master curve as shown in Figure 20b. In the same study, the influence of the precipitation step after some evaporation time was investigated by spraying water onto the evaporating film. As a result, the structure was not immediately frozen in because only an insufficient amount of precipitant could be introduced in that *in situ* SAXS experiment. However, the length scale of the structure immediately adopted the final length scale that was also reached without introducing the precipitant.³²¹ Also the spinning of PS-*block*-P4VP solutions with and without magnesium salt was investigated by SAXS at different positions after the extrudate left the spinning nozzle, which corresponds to different evaporation times. The results are more complex than in film-cast membranes, as the flow rates of polymer solution and bore liquid are additional parameters, which control the shear on the block copolymers in the nozzle and influence the structure formation.³⁰⁴

5.6. Continuum Models for Studying Solvent Evaporation from Block Copolymer Films

There are few studies of EISA from solvent-swollen block copolymer films or NIPS of block copolymer films. Solvent evaporation is the first step of membrane formation, followed by a quench into a coagulation bath, and the structures formed in the course of the initial solvent evaporation template the final

membrane structure as discussed in section 5. The process is considerably more complex than solvent evaporation from a homopolymer film because of the additional order parameter—the AB composition, φ —of microphase separation in the case of diblock copolymers. The number of order parameters increases further for copolymers with more than two blocks. This enlarges the parameter space, and there is an intricate interplay between the characteristic length scale of the microphase and the gradients of the density profiles. Moreover, the microstructure influences the distribution and transport of solvent inside the film. In the following, we confine the discussion to diblock copolymers to highlight some fundamental aspects introduced by microphase separation into the membrane formation.

For filtration applications, the perpendicular orientation of cylindrical domains with respect to the film surface is crucial. According to Phillip, Hillmyer, and Cussler, perpendicular orientation may kinetically arise from rapid solvent evaporation even if the equilibrium orientation of the cylindrical domains of the minority component would be parallel to the film surface.⁸⁸ They employed a one-dimensional, model B description of a solvent-swollen polymer film with a moving-boundary condition at the film surface. For typical experimental conditions, the Biot number is large (or the Péclet number is small); i.e., evaporation is controlled by diffusion of solvent inside the film. After a short time, τ_{fs} , the film surface equilibrates and adopts the densities, $\phi_\alpha^{\text{coex}}$, of the solvent-swollen polymer film in equilibrium with the vapor phase. Inside the polymer film, an approximately linear solvent gradient, $\partial\phi_S/\partial z \approx -[\phi_S^{(0)} - \phi_S^{\text{coex}}]/\Delta h < 0$, is established that extends over a length scale $\Delta h \sim \sqrt{t}$ away from the film surface.

By virtue of incompressibility, $\phi_p + \phi_S = 1$, $\phi_p(z)$ is high at the film surface and linearly decreases toward the initial value, $\phi_p^{(0)}$, over the length, Δh . If the polymer density is sufficiently large, Q_σ the solvent-mitigated incompatibility, eq 2, between the block copolymer species exceeds the ODT-value, $\chi_{\text{ODT}} N$, and microphase separation starts at the film surface by nucleation. Because of the equilibrium phase diagram and confinement effects, initially, spheres will form in the layer where $\chi_{\text{eff}} N$ exceeds $\chi_{\text{ODT}} N$. Subsequently, the existing microphase-separated structure propagates away from the film surface toward the substrate with a velocity

$$u_{\text{cyl}\perp} \sim \frac{R_e}{\tau_R(\phi_S)} [\chi_{\text{eff}}(\phi_S) N - \chi_{\text{ODT}} N] \quad (53)$$

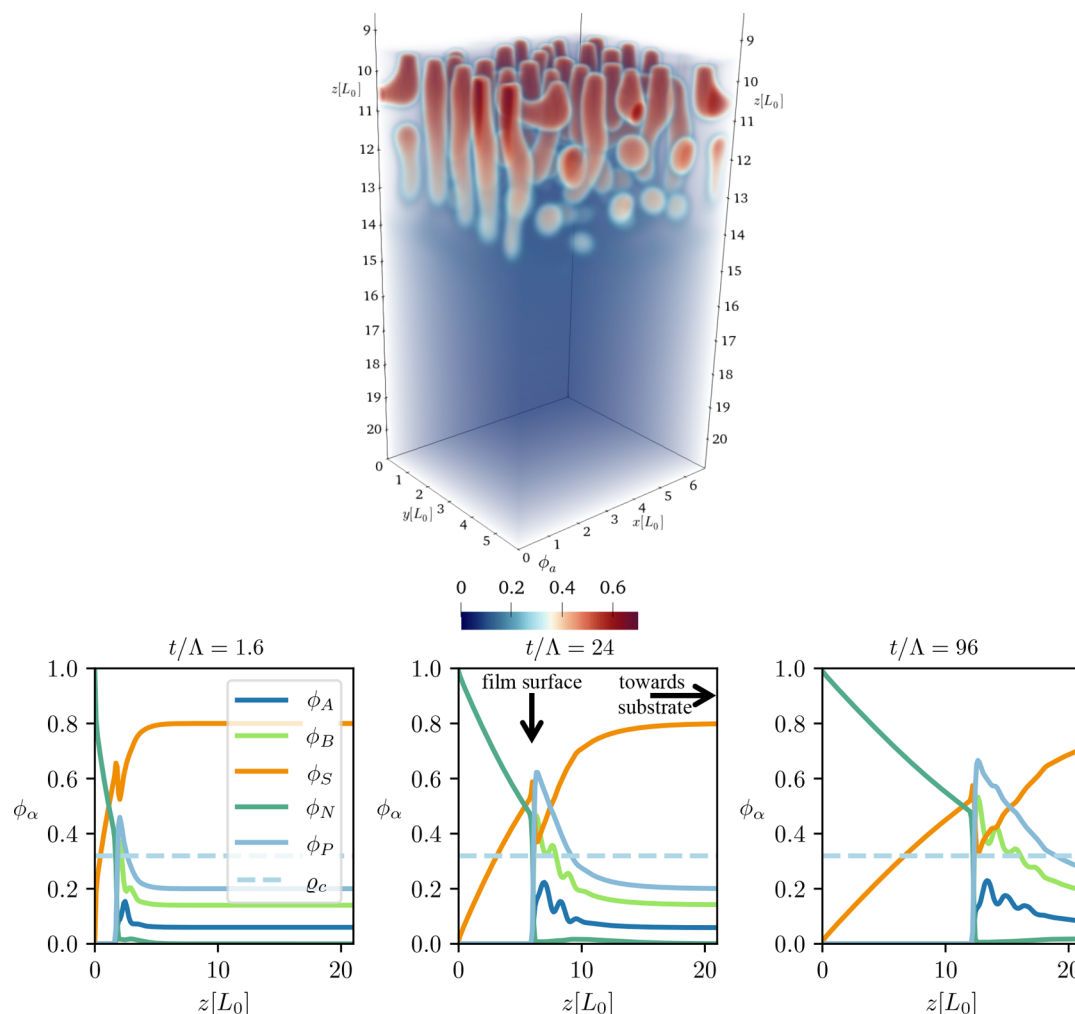


Figure 22. Evaporation from a solvent-swollen diblock copolymer film obtained by model B dynamics of a continuum model.¹³⁸ The top panel depicts the density, $\phi_A(r)$ of the minority component, $f = 0.3$, of the diblock copolymer, according to the color bar at the bottom. $N = 16$, $N_S = N_N = 1$. Initially, the composition of the film was $\phi_P(z) = 0.2$, $\phi_S(z) = 0.8$, and $\phi_N = 0$, and small fluctuations were added. $\chi_{AB}N = 46$, and the air is selective for the majority component, $\chi_{AN}N = 160 > \chi_{BN}N = 80$. The bottom panels present the transversally averaged density profiles of the components at three different times. Length scales are measured in units of the cylinder spacing, L_0 . From ref 323.

according to Goveas and Milner.³²² The first factor characterizes the rate of the underlying single-chain dynamics (or density-dependent Onsager coefficient), whereas the second factor quantifies the thermodynamic driving force. This front velocity depends on the distance from the film surface via the solvent-density profile, $\phi_S(z)$. Phillip, Hillmyer, and Cussler argued that perpendicular cylinders will form if the front velocity, u_{cyl} , increases with the distance from the film surface; i.e., the relaxation rate, $\frac{R_c}{\tau_R(\phi_S)}$, increases faster than the driving force decreases as the solvent density increases farther away from the film surface.

Fredrickson and co-workers used D-SCFT to numerically study the evaporation from copolymer–solvent mixtures.²⁶² They combined the accurate free-energy functional of SCFT with model B dynamics. The free surface of the film was not explicitly considered but a moving-boundary condition was applied that related the evaporation of solvent through the boundary to the shrinkage of the film thickness. The flux, in turn, was dictated by the difference between the solvent density at the surface and the coexistence value, ϕ_S^{coex} , of a film in equilibrium with the nonsolvent (air). One particular benefit of modeling is

that one can disentangle different effects, e.g., evaporation rate and solvent-mitigated incompatibility between blocks, that are difficult to independently vary in an experiment. The study revealed two key parameters for the evaporation-induced structure formation: the effective AB incompatibility at the film surface, $\chi_{\text{eff}}N$, according to the dilution approximation, eq 2, and the strength of the evaporative flux.

Small $\chi_{\text{eff}}N$ and a solvent that is selective for the majority component of the diblock copolymer facilitate the formation of the desired, perpendicular cylinders at the film surface, as illustrated in Figure 21. Unfortunately, this prediction cannot be directly compared to Figure 14 because (i) the experimental correlation refers to the final membrane morphology after solvent–nonsolvent exchange and (ii) a mixed solvent, comprised of components with different volatilities and selectivities, has been characterized by a single parameter, $\bar{\chi}$.³¹⁰

The Uneyama–Doi model¹³⁸ provides an approximate free-energy functional for mixtures of diblock copolymers with solvents. Because of its computational ease compared to D-SCFT, it is computationally feasible to study the evaporation of a solvent-swollen film in contact with a nonsolvent, mimicking air, and study much thicker films.³²³ The top panel of Figure 22

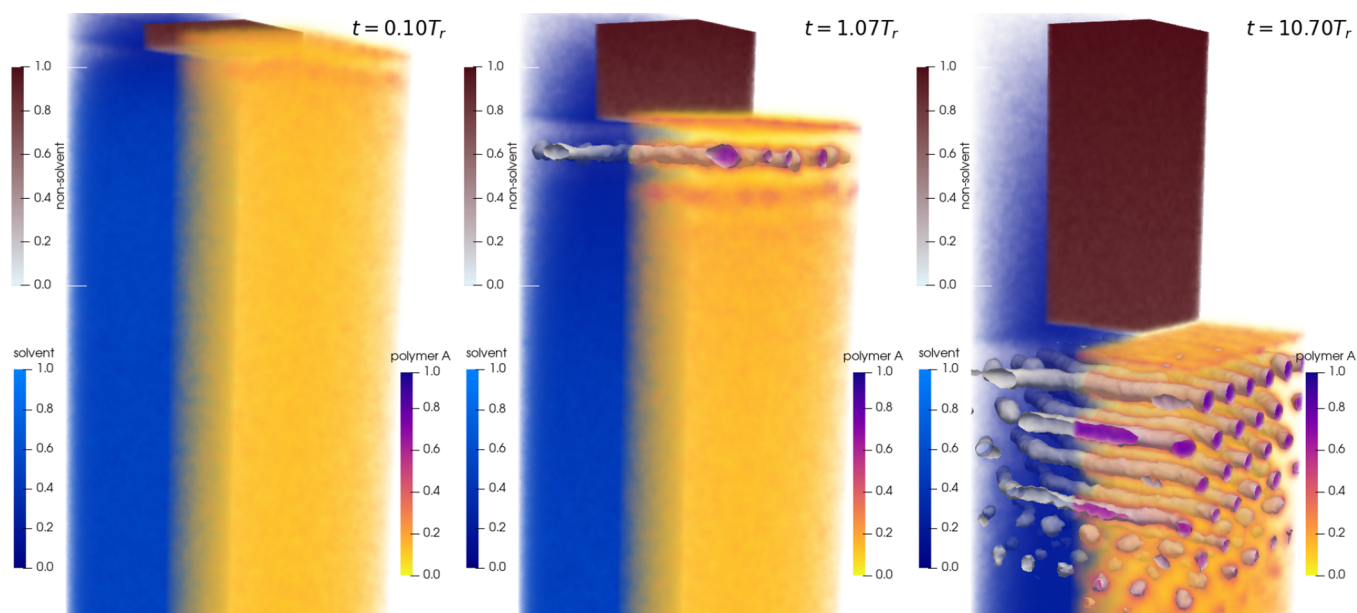


Figure 23. Particle simulation of evaporation from a solvent-swollen copolymer film with SOMA.²⁵⁵ The system geometry is $10 \times 10 \times 40 R_e^3$. The left half of the simulation box shows the density of solvent, ϕ_S (blue) and nonsolvent, ϕ_N (brown). On the right, the density, ϕ_A , of the minority block of the asymmetric diblock, $f = 1/4$, is presented, highlighted with contour surface (full box) after microphase separation sets in. The panels present different snapshots; time increases from left to right. $\chi_{AB}N = 30$, $\chi_{AS}N = \chi_{BS}N = 0$, and $\chi_{AN}N = \chi_{BN}N = 64$, and $\chi_{SN} = 0$.

illustrates the formation of perpendicular cylinders at the film surface. Both the preference of the air for the majority block as well as a rapid evaporation facilitates the formation of perpendicular cylinders in a layer at the film surface. In this layer, the polymers are enriched, and the polymer density exceeds the self-assembly threshold, q_c . One also observes the slightly alternating composition fluctuations inside of the disordered portion of the solvent-swollen film in contact with the ordered surface layer and the formation of spherical domains that subsequently fuse into cylinders. Both features have previously been observed in D-SCFT calculations,²⁶² suggesting that the simpler Uneyama–Doi model¹³⁸ appears to reproduce many features of the SCFT-functional and captured the universal behavior of self-assembly in block copolymer–solvent mixtures.

The panels below show the transversally averaged density profiles of the two components of the diblock copolymer, the solvent, nonsolvent, and the total polymer density for different times. The slope of the solvent profile inside the nonsolvent bath (air) indicates the strength of the evaporative flux. At the narrow film surface, the densities rapidly vary, and there is an enrichment of solvent at the narrow surface. Also the minority component, A, is enriched at the narrow film surface, although this effect is somewhat suppressed by the nonsolvent being selective for the majority component. In a particle-based description, one would also expect such an entropy-driven segregation of the minority block to the narrow film surface, and lattice simulations also indicate that a moderate preference of the vapor for the majority block favors the formation of perpendicular cylinders.³²⁴ Inside the polymer film, the polymer density increases toward the receding film surface. The dashed horizontal line indicates the polymer density, q_c , above which the asymmetric diblock, $f = 0.3$, self-assembles into a cylindrical morphology. Once the widths, Δh , of the zone with $\phi_p(z) > q_c$ exceed the characteristic scale, L_0 , of the self-assembled structure, microphase separation begins.³²³

5.7. Studying Solvent Evaporation from Block Copolymer Films by Particle Simulation

The first particle simulations of solvent evaporation from copolymer films were performed by Tsige et al. using a Lennard–Jones bead–spring model.³²⁵ They observed the formation of a solvent gradient inside the film, and the concomitant polymer skin gave rise to the self-assembly of the block copolymer.

Simulations of soft, coarse-grained particle models in conjunction with DPD molecular dynamics simulation have subsequently been used to study the kinetics of structure formation in solvent-swollen block copolymer films in response to evaporation.^{318,326} Potemkin and co-workers studied solvent evaporation from a film of cylinder-forming diblock copolymers, representing the segments of the two polymer blocks, A and B, the solvent, S, and the nonsolvent, N, by soft particles.³²⁶ The nonsolvent describes an inert gas, and solvent particles at a distance, δ , away from receding film surface are instantaneously and irreversibly switched to nonsolvent, similar to the scheme used by Termonia for homopolymer films.^{288–290} In the molecular simulation, no sharp self-assembly front is observed, and the ordering of the domains occurs on the time scale of the polymer relaxation time that is slow compared to the evaporation of the small solvent particles,³²⁶ potentially giving rise to viscoelastic effects in the early stages of drying.

This study demonstrated that (i) weak segregation between the blocks, (ii) fast solvent evaporation, and (iii) a weak solvent selectivity for the matrix-forming block favor the evaporation-induced formation of cylinders that are perpendicular to the film surface. In accord with the D-SCFT study,²⁶² the simulations observe that spherical micelles initially form at the film surfaces and subsequently join to worm-like cylindrical domains. The vicinity of the ODT facilitates defect annihilation,³²⁷ and the free-energy barrier for changes of the domain morphology increases with $\chi_{AB}N$.^{47,327,328} Potemkin et al. rationalized the requirements of fast evaporation and solvent selectivity for the matrix-forming block by proposing that the evaporative flow of

solvent through the matrix (in conjunction with flows at the internal AB interfaces) aligns the axis of the less swollen and less permeable cylindrical domains perpendicular to the film surface.³²⁶

Very large systems can be studied by calculating the nonbonded interactions via a grid and exploiting the scale separation between the strong bonded and the weak nonbonded interactions. Such a highly coarse-grained model can efficiently be studied by MC simulations in conjunction with the SCMF-algorithm on graphics processing units (GPUs), using the program SOFT coarse-grained Monte Carlo Acceleration (SOMA).^{40,255}

Figure 23 illustrates the solvent evaporation from a solvent-swollen diblock copolymer film in contact with a nonsolvent. Since the soft, nonbonded interactions do not result in a slowing down of the dynamics in regions of high polymer density, the MC simulation employs density-dependent mobilities.¹⁴⁶ At early times, the simulation cell is filled with solvent and copolymer. Similar to refs 288 and 326, the nonpreferential solvent particles are switched to nonsolvent particles at the top of the simulation cell, in order to model evaporation. Upon evaporation, a polymer-rich layer is formed at the film surface. In this polymer-rich and solvent-depleted zone, the system's mobility is reduced, and microphase separation begins by initially forming spherical micelles. As the film surface recedes and the self-assembly front progresses into the film, a gradient of solvent density builds up inside the film. At the self-assembly front, the solvent density is high, and the solvent-mitigated effective incompatibility just passes the ODT-threshold. In accord with the equilibrium phase diagram, spherical micelles form at the front.⁸⁸ Farther toward the film surface, the solvent density decreases, and the effective incompatibility between the blocks increases in turn, resulting in the joining of spherical micelles to cylinders, in accord with previous studies.^{262,326} While this simulation technique cannot include hydrodynamic flow, (i) it is computationally feasible to study large systems⁴⁰ with more than 10^9 soft, coarse-grained particles, (ii) systematically and independently explore the high-dimensional parameter space, and (iii) account for the slow relaxation of the molecular conformations in the course of solvent evaporation and self-assembly.

6. CONCLUSIONS AND PERSPECTIVES

We have presented a selection of theoretical approaches—ranging from simple thermodynamic considerations, via continuum models, up to particle simulations—and experimental results on the nonequilibrium processes in the formation of homopolymer and block copolymer membranes. Whereas technical applications of these polymer membrane materials are emerging, our understanding of the kinetics of structure formation in the course of the rather complex fabrication process still remains rather incomplete: (i) The fabrication of copolymer membranes involves the complex thermodynamics of mixture of a block copolymer and multiple solvents. Whereas the equilibrium phase diagram of linear diblock copolymer melts can be accurately described by SCFT¹²⁶ or simulations,³²⁹ already the deceptively simple phase diagram of a mixture of an AB copolymer with the corresponding homopolymers poses a challenge,^{330–334} and there are plenty of opportunities to tailor the equilibrium structure, e.g., by varying the molecular architecture.¹³⁴ It remains a challenge to account for these complex macromolecular architectures in continuum models such as the Ohta–Kawasaki model¹³⁷ or the Uneyama–Doi

description¹³⁸ and relate their parameters to specific polymer–solvent mixtures. (ii) Since the mixture of polymer materials and multiple solvents is in contact with a supporting substrate and a free surface to the vapor or coagulation bath, there will be a rich interplay between phase behavior in confined geometry and wetting or adsorption phenomena in equilibrium.^{153,335} In turn, confinement in thin³³⁶ and ultrathin³³⁷ layers significantly modifies the self-assembly of copolymers. (iii) The final membrane structure clearly is a nonequilibrium morphology, and the details of the fabrication process, e.g., the time interval of solvent evaporation before contact with the coagulation bath, can be used to tailor the membrane morphology.

The latter aspect is most important because many different nonequilibrium processes such as, e.g., solvent evaporation from a thin film,^{143,144,146,148,262,289,325,326} diffusive solvent–nonsolvent exchange,^{260,261,267–271} macro- and microphase separation,^{169,274,277} structure formation in the presence of property gradients^{169,206,274,277} or moving fronts,^{180,181,206,338} hydrodynamic flow,^{183,277,278} effects of viscoelasticity,^{170,171,195,287} and dynamic arrest due to vitrification,²⁰⁶ crystallization, or gelation conspire in polymer membrane formation, and the thermodynamic and processing variables span a high-dimensional parameter space that dictates the final nonequilibrium structure. As we have tried to illustrate with the help of selected examples, there has been much progress in each of the individual aspects; however, understanding and predicting their interplay in the course of process-directed macro- and microphase separation during NIPS remains a challenge.

By virtue of the long time and large length scales associated with the formation of polymer membranes, a highly coarse-grained particle description or field-theoretic, continuum approach appears to be appropriate. The required level of detail that needs to be captured by the modeling approach, however, still remains to be explored: (i) For instance, often in particle simulations or continuum modeling the starting state is assumed to be completely homogeneous. Computer simulations, however, indicate that fluctuations inside the initial polymer solution are important for the formation of homopolymer membranes via NIPS.²⁹² Likewise, micelles may already form in the as-cast block copolymer film, and they may serve as templates for the subsequent structure formation. (ii) The role of fluctuations is not well understood. Continuum models and D-SCFT often ignore thermal fluctuations or merely add fluctuations in the initial stage to initiate spinodal phase separation. Particle models, in turn, often represent polymers with an unrealistically small invariant degree of polymerization, \bar{N} , thereby exaggerating the role of thermal fluctuations. A realistic strength of thermal fluctuations is required to balance heterogeneous nucleation of domains in a spatially inhomogeneous system and surface-directed spinodal phase separation. (iii) The relation between single-chain dynamics and nonequilibrium structure formation requires attention. In a field-theoretical approach, this relation is established by Onsager coefficients, that are also functions of the local composition because the segmental friction of a segment depends on its environment. (iv) Whereas most continuum descriptions include the hydrodynamic variables, densities, and momenta, additional variables may be needed. A few works have considered temperature changes in time and space inside the film in the course of evaporation or NIPS.^{339–341} Additionally, the macromolecular conformations may not reach instantaneous equilibrium with these hydrodynamic variables but, instead, evolve on a comparable time scale. Integrating out these slow,

conformational degrees of freedom gives rise to Onsager coefficients that are nonlocal in space and time^{173–175} and viscoelastic moduli in the constitutive equation that relates stress to velocity gradients.¹⁷¹ Both effects are not well understood in a spatially inhomogeneous system or computationally infeasible to include in the calculation. Alternatively, such slow, conformational degrees of freedom can be explicitly included in the coarse-grained continuum model.^{170,192,195} The possible choice of the slow, conformational degrees of freedom and efficient schemes to compute their contribution to the free energy need to be explored.⁸² Such effects of viscoelastic phase separation are expected to have a significant qualitative effect on the domain morphology but have not yet been systematically studied in the context of NIPS. (v) Few models have addressed the dynamic arrest of structure formation via vitrification, gelation, or crystallization. The latter two mechanisms require additional order parameters besides densities and momenta.

Thus, there remains a gap in fundamental understanding between membrane materials, fabrication processes, and application properties of polymer membranes. In the near future, no single model will be able to simultaneously address the interplay between all of the aspects compiled above. Therefore, the study of judiciously chosen experimental model systems, highlighting particular nonequilibrium processes, will direct the modeling efforts by understanding the significance of the different phenomena in the different regions of the parameter space and validate the theoretical models. In turn, coarse-grained continuum models and particle simulations can provide direct insights into the spatiotemporal evolution and simultaneously report on collective properties such as density profiles and morphology as well as on single-chain conformations. Moreover, the modeling approaches allow independently varying of parameters, e.g., changing the dynamic asymmetry between the components without altering the equilibrium thermodynamics of the system or switching between entangled and unentangled dynamics, which may be beneficial for elucidating membrane formation mechanisms and highlight the consequences of specific properties and processes. This may be difficult to realize in experiments and may guide the system design to simultaneously optimize for high selectivity, high flux, high stability, large-scale processability, and low costs.

Additionally, data-driven techniques³⁴² may prove useful to identify important correlations in the already available experimental data and thereby focus the modeling efforts. In contrast to systems of hard-condensed matter, the necessary descriptors of nonequilibrium soft-matter systems have to be explored. As emphasized in this review, in addition to the basic thermodynamic characteristics of the constituents, the final nonequilibrium membrane structure is dictated by the sequence of processing steps. Developing meaningful and commonly accepted descriptors for this “history dependence” of nonequilibrium formation of polymer membranes is a challenge for the future.

Whereas much progress can be achieved by a careful design and choice of the coarse-grained model, advances in computational techniques for continuum models and particle simulations will additionally contribute to expand the range of scales that computations can cover, and the small and large scales accessible to simulations and experiments, respectively, start to converge. This will allow computations to systematically explore the parameters that dictate the nonequilibrium processes in polymer membrane formation and thereby help guide experimental efforts.

Although there are many experimental investigations on the preparation and characterization of polymer membranes with kinetically trapped structures, also from an experimental point of view there remain a number of open questions. In most studies, the composition of the atmosphere (air) is not documented, although humidity can have a strong effect during the evaporation step.^{311,343} As the evaporation of solvent is an endothermic process, the temperature may decrease significantly in thin films with an insufficient heat flow and heat capacity from the substrate. Therefore, temperature is changing across the film thickness (along the *z*-direction) and both, thermodynamics and chain relaxation time, are affected. Thus, it will be interesting to investigate the temperature profile during evaporation. Also the temperature difference between the film after the evaporation and the coagulation bath needs to be investigated in more detail, as there are only few data available so far.³⁴⁴ An additional complication arises when solvent mixtures with a temperature-dependent miscibility are used, which can induce phase separation between a polymer-rich and a polymer-lean phase, as it was shown for homopolymer systems.¹⁰⁸ In the case of block copolymers, this could be varied in different ways, such as using a solvent mixture, where the different components are selective for the different blocks, or both solvents being selective for the same block. Such a situation may lead to hierarchical pore structures, which may be interesting for membranes carrying different functionalities in different pores. If stimuli-responsive block copolymers are considered, this will add more complexity to the structure formation, as the polymer conformations may be triggered by an additional stimulus, such as, e.g., light during the membrane formation. Another area requiring more systematic investigations are hollow-fiber membranes from spinning and also electrospinning. Because of the required much larger amount of block copolymer to perform conventional hollow-fiber spinning from solution, there are much fewer studies available on hollow-fiber membranes as compared to flat-sheet membranes. In hollow-fiber membranes, there are big experimental challenges to obtain an open porous surface at the inner side, as typically water is used as a bore liquid, leading to an immediate coagulation when the block copolymer solution leaves the spinneret.³⁰¹ In the case of dual-layer hollow-fiber spinning, where a core fiber is spun simultaneously together with a layer-forming block copolymer, also the control of the interface morphology is a challenging task because both layers should stick to each other but form an open porous connection.³⁰³ The effect of the larger shear forces in the spinneret on the membrane morphology as compared to the shear imposed by a doctor blade in flat-membrane preparation deserves more investigations.³⁰⁴ Shear may influence not only the surface morphology but also the formation of macrovoids along the cross-section of the membrane. In flat-sheet geometry, roll casting is a possible strategy to produce membranes with significantly less amount of block copolymer,³¹⁹ and the influence of mechanical stress in the process is not studied yet. There are not many studies yet on the influence of an electric field during the evaporation time and the effect of the electric field on microphase separation, and the orientation of the microdomains is not fully understood.³⁴⁵ Coupling different external stress fields such as, e.g., biaxial mechanical stretching³⁴⁶ or combining uniaxial shear with an electric field during membrane casting,³⁴⁷ could influence the final membrane morphology and may become interesting for membrane formation. Besides single shear also large amplitude oscillatory shear is a known way to yield aligned block copolymer

morphologies, where the orientation of the microdomains depends on the frequency both in bulk^{348–350} and in concentrated solution.³⁵¹ Another challenging topic is block copolymer membranes with pores down to the sub-10 nm range, which requires low-molecular-weight block copolymers with a very high χ -parameter.³⁵² Such block copolymer membranes will likely suffer from low mechanical stability due to the lack of entanglements in the matrix blocks, a problem which may be overcome by cross-linking. While we focused our discussion on cylinder-forming block copolymers, also other morphologies such as gyroids or lamellae are of interest and have not been studied yet in the context of integral-asymmetric membranes. Also more complex block copolymers are interesting, and only few have been studied so far.^{27,76}

This is obviously an incomplete list of interesting issues to be addressed in the future. As pointed out before, a single, overarching modeling and simulation strategy for the complex nonequilibrium processes in polymer membrane formation has not yet emerged, but there are various opportunities where experimental data could assist the development and validation of models, e.g., by providing information about the initial micelle formation in copolymer solutions before contact with the coagulation bath or by systematically exploring the dynamic asymmetry between the components via changing the molecular weight of the polymers or tailoring the glass-transition temperature of the components. Since the polymer membrane is a dynamically arrested nonequilibrium state, it is important not only to provide experimental information about final membrane structure but to quantify the complex spatiotemporal structure formation along the fabrication process. This will contribute to identify the necessary descriptors that quantify the nonequilibrium process-directed structure formation. The compilation of a suitable data pool will serve to validate and refine physical models, and, additionally, it could be used for the application of artificial-intelligence techniques to suggest process parameters for the preparation of membranes with specific structures and compositions. Ultimately, the combination of modeling and simulation in conjunction with data-driven techniques may be employed as digital twins to complement experiments in the development of new membrane materials.

AUTHOR INFORMATION

Corresponding Authors

Marcus Müller — *Georg-August Universität, Institut für Theoretische Physik, 37073 Göttingen, Germany;*
✉ orcid.org/0000-0002-7472-973X; Email: mmueller@theorie.physik.uni-goettingen.de

Volker Abetz — *Helmholtz-Zentrum Hereon, Institut für Membranforschung, 21502 Geesthacht, Germany; Universität Hamburg, Institut für Physikalische Chemie, 20146 Hamburg, Germany;* ✉ orcid.org/0000-0002-4840-6611;
Email: volker.abetz@hereon.de

Complete contact information is available at:
<https://pubs.acs.org/10.1021/acs.chemrev.1c00029>

Notes

The authors declare no competing financial interest.

Biographies

Marcus Müller received his Ph.D. in 1995 from the Johannes Gutenberg-Universität in Mainz, Germany, working with Kurt Binder. After collaborating with Mike Cates on ring polymers at the EPCC

Edinburgh, he worked as a Feodor Lynen fellow with Michael Schick (University of Washington) on homopolymer/copolymer mixtures and fusion of model bilayer membranes. Back in Mainz, he obtained his habilitation in theoretical physics in 1999. Before joining the Institute for Theoretical Physics in Göttingen, he was an associate professor of physics at the University of Wisconsin-Madison and a Heisenberg fellow of the German Science Foundation (DFG). The APS awarded him the 2004 John H. Dillon Medal. In the same year, he received a Lichtenberg professorship from the Volkswagen foundation. He is a fellow of the APS, an associate editor of *ACS Macro Letters*, a fellow of the Max-Planck school Matter to Life, and currently speaker of the division of Chemical and Polymer Physics of the Germany Physical Society. His research interests focus on computational soft and biological matter. Using computer simulations and numerical self-consistent field calculations, he develops highly coarse-grained models for copolymers and biological membranes and investigates wetting and phase behavior in thin films and the kinetics of process-directed self-assembly of copolymers, homopolymer blends, and binary brushes.

Volker Abetz studied chemistry at the Albert-Ludwigs-Universität Freiburg, Germany. He worked on spectroscopic polarimetry of multicomponent polymer systems at Freiburg with Reimund Stadler and Stanford University with Gerald G. Fuller and received his Ph.D. in 1990 in Freiburg. In the following three years, he worked at the Max-Planck-Institut für Polymerforschung in Mainz, Germany, with Erhard W. Fischer on structure and dynamics of polymer blends. In 1993, he received a European fellowship to work with Guy C. Meyer on interpenetrating polymer networks at the Institut Charles Sadron, Strasbourg, France. Then he went to the Johannes Gutenberg-Universität Mainz and worked with Reimund Stadler in the field of block copolymers. They moved to Universität Bayreuth in 1997, and he obtained his habilitation in macromolecular chemistry in 2000. He became an associate professor for polymer chemistry at Universität Potsdam in 2004 and later in the same year full professor for polymer-based multicomponent materials at the Christian-Albrechts-Universität zu Kiel and a director of the Institute of Chemistry at GKSS-Forschungszentrum (now Institute of Membrane Research at Helmholtz-Zentrum Hereon) in Geesthacht, Germany. In 2012, he became a full professor for physical chemistry at the Universität Hamburg, Germany. The World Forum on Advanced Materials under the auspice of IUPAC awarded him the Paul J. Flory Polymer Research Prize 2017. His research interests are in the area of chemistry and physics of polymers and polymer composites for applications as structural materials and membranes, with a focus on the self-assembly of block copolymers, polymer blends, and networks.

ACKNOWLEDGMENTS

We thank N. Blagojevic, O. Dreyer, G. Ibbeken, M. Radjabian, L. Schneider, and Q. Tang for fruitful collaboration and acknowledge L. Schneider and O. Dreyer for the simulations that resulted in Figure 23. Financial support was provided by the Deutsche Forschungsgemeinschaft (DFG) under Grants Mu 1674/15-2, Mu 1674/16-2, AB 113/6-1, FP7 EU-project SELFMEM under grant agreement NMP3-SL-2009-228652, and I2B project “DigiZwiMem” by Helmholtz-Zentrum Hereon. The authors gratefully acknowledge the Gauss Centre for Supercomputing e.V. (www.gauss-centre.eu) for providing computing time through the von Neumann Institute for Computing (NIC) on the GCS Supercomputer JUWELS at Jülich Supercomputing Centre (JSC).

ADDITIONAL NOTES

^aIn principle, any polymer with a distribution of molecular weights or composition dispersity in the case of a block copolymer can be conceived as a multicomponent blend by itself, resulting in fractionation effects. This complication, however, is ignored in the following.

^bOnly in the case in which the solvent is nonselective and the interactions between the blocks are sufficiently screened by the solvent, the behavior of a copolymer in solution will resemble the behavior of a homopolymer.

^cIn the case of the Ohta–Kawasaki model¹³⁷ or the Uneyama–Doi model¹³⁸ for systems containing copolymers, no modification is necessary because the functional, eq 8, already includes the necessary gradient terms.

^dThe tie lines describe phase coexistence where the chemical potentials and the pressure in both coexisting phases are equal.

^eIgnore that the interactions at the substrate result in a time dependence of $\phi_\alpha(z=0)$ for $t < \tau_{\text{mix}}$. In this mixing regime, the densities at the substrate are those of the initial polymer film, $\phi_\alpha^{(0)}$. At the contact between substrate and the miscible polymer–solvent system, an adsorption layer may build up, but no wetting phenomena can occur.

^fIf χ_{SN} is sufficiently large such that solvent and air (nonsolvent) phase separate, the vapor pressure of the solvent in air should be below its saturation value.

^gEffects of long-range, van-der-Waals interactions between substrate and polymer or nonsolvent as well as prewetting phenomena have been ignored in the discussion.

REFERENCES

- (1) Drioli, E.; Brunetti, A.; Di Profio, G.; Barbieri, G. Process Intensification Strategies and Membrane Engineering. *Green Chem.* **2012**, *14*, 1561–1572.
- (2) Bechhold, H. Durchlässigkeit von Ultrafiltern. *Z. Phys. Chem.* **1908**, *64U*, 328–342.
- (3) Kolff, W. J.; Berk, H. Th. J.; Welle, N. M.; van der Ley, A. J. W.; van Dijk, E. C.; van Noordwijk, J. The Artificial Kidney: A Dialyser with a Great Area. *Acta Med. Scand.* **1944**, *117*, 121–134.
- (4) Strathmann, H. *Introduction to Membrane Science and Technology*; Wiley-VCH: Weinheim, 2011.
- (5) Sakai, K. Dialysis Membranes for Blood Purification. *Front. Med. Biol. Eng.* **2000**, *10*, 117–129.
- (6) Lee, A.; Elam, J. W.; Darling, S. B. Membrane Materials for Water Purification: Design, Development, and Application. *Environ. Sci. Water Res. Technol.* **2016**, *2*, 17–42.
- (7) Drioli, E.; Stankiewicz, A. I.; Macedonio, F. Membrane Engineering in Process Intensification—An Overview. *J. Membr. Sci.* **2011**, *380*, 1–8.
- (8) Shannon, M. A.; Bohn, P. W.; Elimelech, M.; Georgiadis, J. G.; Mariñas, B. J.; Mayes, A. M. Science and Technology for Water Purification in the Coming Decades. *Nature* **2008**, *452*, 301–310.
- (9) Mulder, M. *Basic Principles of Membrane Technology*; Springer: Netherlands, 1996.
- (10) Baker, R. W. *Membrane Technology and Applications*; Wiley Online Library, 2004.
- (11) Elimelech, M.; Phillip, W. A. The Future of Seawater Desalination: Energy, Technology, and the Environment. *Science* **2011**, *333*, 712–717.
- (12) Paul, D. R. *Polymeric Gas Separation Membranes*; Routledge & CRC Press, 1994.
- (13) Lu, G. Q.; Diniz da Costa, J. C.; Duke, M.; Giessler, S.; Socolow, R.; Williams, R. H.; Kreutz, T. Inorganic Membranes for Hydrogen Production and Purification: A Critical Review and Perspective. *J. Colloid Interface Sci.* **2007**, *314*, 589–603.
- (14) Kayvani Fard, A.; McKay, G.; Buekenhoudt, A.; Al Sulaiti, H.; Motmans, F.; Khraishah, M.; Atieh, M. Inorganic Membranes:

Preparation and Application for Water Treatment and Desalination. *Materials* **2018**, *11*, 74.

(15) Zhang, R.; Liu, Y.; He, M.; Su, Y.; Zhao, X.; Elimelech, M.; Jiang, Z. Antifouling Membranes for Sustainable Water Purification: Strategies and Mechanisms. *Chem. Soc. Rev.* **2016**, *45*, 5888–5924.

(16) Huang, S.; Ras, R. H. A.; Tian, X. Antifouling Membranes for Oily Wastewater Treatment: Interplay between Wetting and Membrane Fouling. *Curr. Opin. Colloid Interface Sci.* **2018**, *36*, 90–109.

(17) Ren, Y.; Liang, X.; Dou, H.; Ye, C.; Guo, Z.; Wang, J.; Pan, Y.; Wu, H.; Guiver, M. D.; Jiang, Z. Membrane-Based Olefin/Paraffin Separations. *Adv. Sci.* **2020**, *7*, 2001398.

(18) Saxena, A.; Tripathi, B. P.; Kumar, M.; Shahi, V. K. Membrane-based Techniques for the Separation and Purification of Proteins: An Overview. *Adv. Colloid Interface Sci.* **2009**, *145*, 1–22.

(19) Agüero, R.; Bringas, E.; Roman, M. F. S.; Ortiz, I.; Ibanez, R. Membrane Processes for Whey Proteins Separation and Purification. *A Review. Curr. Org. Chem.* **2017**, *21*, 1740–1752.

(20) Antony, A.; Low, J. H.; Gray, S.; Childress, A. E.; Le-Clech, P.; Leslie, G. Scale Formation and Control in High Pressure Membrane Water Treatment Systems: A Review. *J. Membr. Sci.* **2011**, *383*, 1–16.

(21) Guo, W.; Ngo, H.-H.; Li, J. A Mini-Review on Membrane Fouling. *Bioresour. Technol.* **2012**, *122*, 27–34.

(22) Quay, A.; Tong, T.; Hashmi, S. M.; Zhou, Y.; Zhao, S.; Elimelech, M. Combined Organic Fouling and Inorganic Scaling in Reverse Osmosis: Role of Protein-Silica Interactions. *Environ. Sci. Technol.* **2018**, *52*, 9145–9153.

(23) Paul, D. R. *Encyclopedia of Membranes*; Springer: Berlin, Germany, 2016; pp 1149–1151.

(24) Majeed, S.; Fierro, D.; Buhr, K.; Wind, J.; Du, B.; Boschetti-De Fierro, A.; Abetz, V. Multi-walled Carbon Nanotubes (MWCNTs) Mixed Polyacrylonitrile (PAN) Ultrafiltration Membranes. *J. Membr. Sci.* **2012**, *403–404*, 101–109.

(25) Loeb, S.; Sourirajan, S. Sea Water Demineralization by means of an Osmotic Membrane. *Adv. Chem. Ser.* **1963**, *38*, 117–132.

(26) Peinemann, K.-V.; Abetz, V.; Simon, P. F. W. Asymmetric Superstructure formed in a Block Copolymer via Phase Separation. *Nat. Mater.* **2007**, *6*, 992–996.

(27) Radjabian, M.; Abetz, V. Advanced Porous Polymer Membranes from Self-Assembling Block Copolymers. *Prog. Polym. Sci.* **2020**, *102*, 101219.

(28) Hampu, N.; Werber, J. R.; Chan, W. Y.; Feinberg, E. C.; Hillmyer, M. A. Next-Generation Ultrafiltration Membranes enabled by Block Polymers. *ACS Nano* **2020**, *14*, 16446–16471.

(29) Oss-Ronen, L.; Schmidt, J.; Abetz, V.; Radulescu, A.; Cohen, Y.; Talmon, Y. Characterization of Block Copolymer Self-Assembly: From Solution to Nanoporous Membranes. *Macromolecules* **2012**, *45*, 9631–9642.

(30) Gu, X.; Gunkel, I.; Hexemer, A.; Gu, W.; Russell, T. P. An in Situ Grazing Incidence X-Ray Scattering Study of Block Copolymer Thin Films During Solvent Vapor Annealing. *Adv. Mater.* **2014**, *26*, 273–281.

(31) Marques, D. S.; Dorin, R. M.; Wiesner, U.; Smilgies, D.-M.; Behzad, A. R.; Vainio, U.; Peinemann, K.-V.; Nunes, S. P. Time-resolved GISAXS and Cryo-Microscopy Characterization of Block Copolymer Membrane Formation. *Polymer* **2014**, *55*, 1327–1332.

(32) Zhang, J.; Posselt, D.; Smilgies, D.-M.; Perlich, J.; Kyriakos, K.; Jaksch, S.; Papadakis, C. M. Lamellar Diblock Copolymer Thin Films during Solvent Vapor Annealing studied by GISAXS: Different Behavior of Parallel and Perpendicular Lamellae. *Macromolecules* **2014**, *47*, 5711–5718.

(33) Samant, S.; Strzalka, J.; Yager, K. G.; Kisslinger, K.; Grolman, D.; Basutkar, M.; Salunke, N.; Singh, G.; Berry, B.; Karim, A. Ordering Pathway of Block Copolymers under Dynamic Thermal Gradients studied by in Situ GISAXS. *Macromolecules* **2016**, *49*, 8633–8642.

(34) Gunkel, I.; Gu, X.; Sun, Z.; Schaible, E.; Hexemer, A.; Russell, T. P. An In Situ GISAXS Study of Selective Solvent Vapor Annealing in Thin Block Copolymer Films: Symmetry Breaking of In-Plane Sphere Order upon Deswelling. *J. Polym. Sci., Part B: Polym. Phys.* **2016**, *54*, 331–338.

- (35) Gu, Y.; Dorin, R. M.; Tan, K. W.; Smilgies, D.-M.; Wiesner, U. In Situ Study of Evaporation-Induced Surface Structure Evolution in Asymmetric Triblock Terpolymer Membranes. *Macromolecules* **2016**, *49*, 4195–4201.
- (36) Berezkin, A. V.; Jung, F.; Posselt, D.; Smilgies, D.-M.; Papadakis, C. M. In Situ Tracking of Composition and Morphology of a Diblock Copolymer Film with GISAXS during Exchange of Solvent Vapors at Elevated Temperatures. *Adv. Funct. Mater.* **2018**, *28*, 1706226.
- (37) Liedel, C.; Hund, M.; Olszowska, V.; Böker, A. On the Alignment of a Cylindrical Block Copolymer: a Time-resolved and 3-dimensional SFM Study. *Soft Matter* **2012**, *8*, 995–1002.
- (38) Raybin, J.; Ren, J.; Chen, X.; Gronheid, R.; Nealey, P. F.; Sibener, S. J. Real-Time Atomic Force Microscopy Imaging of Block Copolymer Directed Self Assembly. *Nano Lett.* **2017**, *17*, 7717–7723.
- (39) Shelton, C. K.; Jones, R. L.; Epps, T. H. Kinetics of Domain Alignment in Block Polymer Thin Films during Solvent Vapor Annealing with Soft Shear: An in Situ Small-Angle Neutron Scattering Investigation. *Macromolecules* **2017**, *50*, 5367–5376.
- (40) Schneider, L. Y.; Müller, M. Engineering Scale Simulation of Nonequilibrium Network Phases for Battery Electrolytes. *Macromolecules* **2019**, *52*, 2050–2062.
- (41) Schaefer, C.; van der Schoot, P.; Michels, J. J. Structuring of Polymer Solutions upon Solvent Evaporation. *Phys. Rev. E* **2015**, *91*, 022602.
- (42) Schaefer, C.; Michels, J. J.; van der Schoot, P. Structuring of Thin-Film Polymer Mixtures upon Solvent Evaporation. *Macromolecules* **2016**, *49*, 6858–6870.
- (43) Schaefer, C.; Michels, J. J.; van der Schoot, P. Dynamic Surface Enrichment in Drying Thin-Film Binary Polymer Solutions. *Macromolecules* **2017**, *50*, 5914–5919.
- (44) Cummings, J.; Lowengrub, J. S.; Sumpter, B. G.; Wise, S. M.; Kumar, R. Modeling Solvent Evaporation during Thin Film Formation in Phase Separating Polymer Mixtures. *Soft Matter* **2018**, *14*, 1833–1846.
- (45) Stenbock-Fermor, A.; Knoll, A. W.; Böker, A.; Tsarkova, L. Enhancing Ordering Dynamics in Solvent-Annealed Block Copolymer Films by Lithographic Hard Mask Supports. *Macromolecules* **2014**, *47*, 3059–3067.
- (46) Stenbock-Fermor, A.; Rudov, A. A.; Gumerov, R. A.; Tsarkova, L. A.; Böker, A.; Möller, M.; Potemkin, I. I. Morphology-Controlled Kinetics of Solvent Uptake by Block Copolymer Films in Nonselective Solvent Vapors. *ACS Macro Lett.* **2014**, *3*, 803–807.
- (47) Hur, S.-M.; Khaira, G. S.; Ramirez-Hernandez, A.; Müller, M.; Nealey, P. F.; de Pablo, J. J. Simulation of Defect Reduction in Block Copolymer Thin Films by Solvent Annealing. *ACS Macro Lett.* **2015**, *4*, 11–15.
- (48) Hannon, A. F.; Bai, W.; Alexander-Katz, A.; Ross, C. A. Simulation Methods for Solvent Vapor Annealing of Block Copolymer Thin Films. *Soft Matter* **2015**, *11*, 3794–3805.
- (49) Chao, H.; Koski, J.; Riggelman, R. A. Solvent Vapor Annealing in Block Copolymer Nanocomposite Films: a Dynamic Mean Field Approach. *Soft Matter* **2017**, *13*, 239–249.
- (50) Xiong, S.; Li, D.; Hur, S.-M.; Craig, G. S. W.; Arges, C. G.; Qu, X.-P.; Nealey, P. F. The Solvent Distribution Effect on the Self-Assembly of Symmetric Triblock Copolymers during Solvent Vapor Annealing. *Macromolecules* **2018**, *51*, 7145–7151.
- (51) Paradiso, S. P.; Delaney, K. T.; Garcia-Cervera, C. J.; Cenicerros, H. D.; Fredrickson, G. H. Cyclic Solvent Annealing Improves Feature Orientation in Block Copolymer Thin Films. *Macromolecules* **2016**, *49*, 1743–1751.
- (52) Amundson, K.; Helfand, E.; Quan, X.; Hudson, S. D.; Smith, S. D. Alignment of Lamellar Block Copolymer Microstructure in an Electric Field. 2. Mechanisms of Alignment. *Macromolecules* **1994**, *27*, 6559–6570.
- (53) Morkved, T. L.; Lu, M.; Urbas, A. M.; Ehrichs, E. E.; Jaeger, H. M.; Mansky, P.; Russell, T. P. Local Control of Microdomain Orientation in Diblock Copolymer Thin Films with Electric Fields. *Science* **1996**, *273*, 931–933.
- (54) Ashok, B.; Muthukumar, M.; Russell, T. P. Confined Thin Film Diblock Copolymer in the Presence of an Electric Field. *J. Chem. Phys.* **2001**, *115*, 1559.
- (55) Böker, A.; Elbs, H.; Hänsel, H.; Knoll, A.; Ludwigs, S.; Zettl, H.; Urban, V.; Abetz, V.; Müller, A. H. E.; Krausch, G. Microscopic Mechanisms of Electric Field induced Alignment of Block Copolymer Microdomains. *Phys. Rev. Lett.* **2002**, *89*, 135502.
- (56) Kyrlyuk, A. V.; Zvelindovsky, A. V.; Sevink, G. J. A.; Fraaije, J. G. E. M. Lamellar Alignment of Diblock Copolymers in An Electric Field. *Macromolecules* **2002**, *35*, 1473–1476.
- (57) Thurn-Albrecht, T.; DeRouchey, J.; Russell, T. P.; Kolb, R. Pathways toward Electric Field induced Alignment of Block Copolymers. *Macromolecules* **2002**, *35*, 8106–8110.
- (58) Boker, A.; Elbs, H.; Hansel, H.; Knoll, A.; Ludwigs, S.; Zettl, H.; Zvelindovsky, A. V.; Sevink, G. J. A.; Urban, V.; Abetz, V.; Müller, A. H. E.; Krausch, G. Electric Field induced Alignment of Concentrated Block Copolymer Solutions. *Macromolecules* **2003**, *36*, 8078–8087.
- (59) Tsori, Y.; Andelman, D. Thin Film Diblock Copolymers in Electric Field: Transition from Perpendicular to Parallel Lamellae. *Macromolecules* **2002**, *35*, 5161–5170.
- (60) Tsori, Y.; Tournilhac, F.; Leibler, L. Orienting Ion-containing Block Copolymers using AC Electric Fields. *Macromolecules* **2003**, *36*, 5873–5877.
- (61) Matsen, M. W. Electric Field Alignment in Thin Films of Cylinder-Forming Diblock Copolymer. *Macromolecules* **2006**, *39*, 5512–5520.
- (62) Matsen, M. W. Stability of a Block-Copolymer Lamella in a Strong Electric Field. *Phys. Rev. Lett.* **2005**, *95*, 258302.
- (63) Matsen, M. W. Undulation Instability in Block-Copolymer Lamellae subjected to a Perpendicular Electric Field. *Soft Matter* **2006**, *2*, 1048–1056.
- (64) Tsori, Y.; Andelman, D.; Lin, C.-Y.; Schick, M. Block Copolymers in Electric Fields: A Comparison of Single-Mode and Self-Consistent-Field Approximations. *Macromolecules* **2006**, *39*, 289–293.
- (65) Schmidt, K.; Schoberth, H. G.; Schubert, F.; Hänsel, H.; Fischer, F.; Weiss, T.; Sevink, G.; Zvelindovsky, A.; Böker, A.; Krausch, G. Scaling Behavior of the Reorientation Kinetics of Block Copolymers exposed to Electric Fields. *Soft Matter* **2007**, *3*, 448–453.
- (66) Tsori, Y. Lamellar Phases in Nonuniform Electric Fields: Breaking the In-Plane Rotation Symmetry and the Role of Dielectric Constant Mismatch. *Macromolecules* **2007**, *40*, 1698–1702.
- (67) Tsori, Y. *Colloquium*: Phase Transitions in Polymers and Liquids in Electric Fields. *Rev. Mod. Phys.* **2009**, *81*, 1471–1494.
- (68) Schoberth, H. G.; Pester, C. W.; Ruppel, M.; Urban, V. S.; Böker, A. Orientation-Dependent Order-Disorder Transition of Block Copolymer Lamellae in Electric Fields. *ACS Macro Lett.* **2013**, *2*, 469–473.
- (69) Welling, U.; Müller, M.; Shalev, H.; Tsori, Y. Block Copolymer Ordering in Cylindrical Capacitors. *Macromolecules* **2014**, *47*, 1850–1864.
- (70) Pester, C. W.; Liedel, C.; Ruppel, M.; Böker, A. Block Copolymers in Electric Fields. *Prog. Polym. Sci.* **2017**, *64*, 182–214.
- (71) Martin, J. M.; Li, W.; Delaney, K. T.; Fredrickson, G. H. SCFT Study of Diblock Copolymer Melts in Electric Fields: Selective Stabilization of Orthorhombic Fddd Network Phase. *Macromolecules* **2018**, *51*, 3369–3378.
- (72) Schulze, M. W.; McIntosh, L. D.; Hillmyer, M. A.; Lodge, T. P. High-Modulus, High-Conductivity Nanostructured Polymer Electrolyte Membranes via Polymerization-Induced Phase Separation. *Nano Lett.* **2014**, *14*, 122–126.
- (73) Upadhyaya, L.; Semsarilar, M.; Fernández-Pacheco, R.; Martinez, G.; Mallada, R.; Deratani, A.; Quemener, D. Porous Membranes from Acid Decorated Block Copolymer Nano-Objects via RAFT Alcoholic Dispersion Polymerization. *Polym. Chem.* **2016**, *7*, 1899–1906.
- (74) Upadhyaya, L.; Semsarilar, M.; Nehache, S.; Cot, D.; Fernández-Pacheco, R.; Martinez, G.; Mallada, R.; Deratani, A.; Quemener, D. Nanostructured Mixed Matrix Membranes from Supramolecular

Assembly of Block Copolymer Nanoparticles and Iron Oxide Nanoparticles. *Macromolecules* **2016**, *49*, 7908–7916.

(75) Upadhyaya, L.; Oliveira, B.; Pereira, V. J.; Barreto Crespo, M. T.; Crespo, J. G.; Quemener, D.; Semsarilar, M. Nanocomposite Membranes from Nano-Particles prepared by Polymerization Induced Self-Assembly and their Biocidal Activity. *Sep. Purif. Technol.* **2020**, *251*, 117375.

(76) Zhang, Z.; Rahman, Md. M.; Abetz, C.; Höhme, A.-L.; Sperling, E.; Abetz, V. Chemically Tailored Multifunctional Asymmetric Isoporous Triblock Terpolymer Membranes for Selective Transport. *Adv. Mater.* **2020**, *32*, 1907014.

(77) Weidman, J. L.; Mulvenna, R. A.; Boudouris, B. W.; Phillip, W. A. Nanostructured Membranes from Triblock Polymer Precursors as High Capacity Copper Adsorbents. *Langmuir* **2015**, *31*, 11113–11123.

(78) Kanduč, M.; Kim, W. K.; Roa, R.; Dzubiella, J. Selective Molecular Transport in Thermoresponsive Polymer Membranes: Role of Nanoscale Hydration and Fluctuations. *Macromolecules* **2018**, *51*, 4853–4864.

(79) Sun, W.; Shi, J.; Chen, C.; Li, N.; Xu, Z.; Li, J.; Lv, H.; Qian, X.; Zhao, L. A Review on Organic-Inorganic Hybrid Nanocomposite Membranes: A Versatile Tool to Overcome the Barriers of Forward Osmosis. *RSC Adv.* **2018**, *8*, 10040–10056.

(80) Sing, K. S. W. *Studies in Surface Science and Catalysis*; Elsevier: Waltham, MA, USA, 1991; Vol. 62; pp 1–9.

(81) Abetz, V.; Kremer, K.; Müller, M.; Reiter, G. Functional Macromolecular Systems: Kinetic Pathways to Obtain Tailored Structures. *Macromol. Chem. Phys.* **2019**, *220*, 1800334.

(82) Müller, M. Process-Directed Self-Assembly of Copolymers: Results of and Challenges for Simulation Studies. *Prog. Polym. Sci.* **2020**, *101*, 101198.

(83) Hung, W.-L.; Wang, D.-M.; Lai, J.-Y.; Chou, S.-C. On the Initiation of Macrovoids in Polymeric Membranes - Effect of Polymer Chain Entanglement. *J. Membr. Sci.* **2016**, *505*, 70–81.

(84) Radjabian, M.; Abetz, C.; Fischer, B.; Meyer, A.; Abetz, V. Influence of Solvent on the Structure of an Amphiphilic Block Copolymer in Solution and in Formation of an Integral Asymmetric Membrane. *ACS Appl. Mater. Interfaces* **2017**, *9*, 31224–31234.

(85) Leibler, L. Theory of Microphase Separation in Block Copolymers. *Macromolecules* **1980**, *13*, 1602–1617.

(86) Bates, F. S.; Hillmyer, M. A.; Lodge, T. P.; Bates, C. M.; Delaney, K. T.; Fredrickson, G. H. Multiblock Polymers: Panacea or Pandora's Box? *Science* **2012**, *336*, 434–440.

(87) Thurn-Albrecht, T.; Schotter, J.; Kastle, C. A.; Emley, N.; Shibauchi, T.; Krusin-Elbaum, L.; Guarini, K.; Black, C. T.; Tuominen, M. T.; Russell, T. P. Ultrahigh-Density Nanowire Arrays Grown in Self-Assembled Diblock Copolymer Templates. *Science* **2000**, *290*, 2126–2129.

(88) Phillip, W. A.; Hillmyer, M. A.; Cussler, E. L. Cylinder Orientation Mechanism in Block Copolymer Thin Films Upon Solvent Evaporation. *Macromolecules* **2010**, *43*, 7763–7770.

(89) Stefik, M.; Wang, S.; Hovden, R.; Sai, H.; Tate, M. W.; Muller, D. A.; Steiner, U.; Gruner, S. M.; Wiesner, U. Networked and Chiral Nanocomposites from ABC Triblock Terpolymer Coassembly with Transition Metal Oxide Nanoparticles. *J. Mater. Chem.* **2012**, *22*, 1078–1087.

(90) Guo, L.; Wang, Y. Nanoslitting of Phase-separated Block Copolymers by Solvent Swelling for Membranes with Ultrahigh Flux and Sharp Selectivity. *Chem. Commun.* **2014**, *50*, 12022–12025.

(91) Metwalli, E.; Rasool, M.; Brunner, S.; Müller-Buschbaum, P. Lithium-Salt-Containing High-Molecular-Weight Polystyrene-block-Polyethylene Oxide Block Copolymer Films. *ChemPhysChem* **2015**, *16*, 2882–2889.

(92) Kim, S. H.; Misner, M. J.; Xu, T.; Kimura, M.; Russell, T. P. Highly Oriented and Ordered Arrays from Block Copolymers via Solvent Evaporation. *Adv. Mater.* **2004**, *16*, 226–231.

(93) Yang, S. Y.; Ryu, I.; Kim, H. Y.; Kim, J. K.; Jang, S. K.; Russell, T. P. Nanoporous Membranes with Ultrahigh Selectivity and Flux for the Filtration of Viruses. *Adv. Mater.* **2006**, *18*, 709–712.

(94) Cohen, C.; Tanny, G. B.; Prager, S. Diffusion-Controlled Formation of Porous Structures in Ternary Polymer Systems. *J. Polym. Sci., Polym. Phys. Ed.* **1979**, *17*, 477–489.

(95) Zhang, P.; Alsaifi, N. M.; Wang, Z.-G. Revisiting the Θ Point. *Macromolecules* **2020**, *53*, 10409–10420.

(96) Wang, Z.-G. 50th Anniversary Perspective: Polymer Conformation—A Pedagogical Review. *Macromolecules* **2017**, *50*, 9073–9114.

(97) Kirste, R. G.; Kruse, W. A.; Ibel, K. Determination of the Conformation of Polymers in the Amorphous Solid State and in Concentrated Solution by Neutron Diffraction. *Polymer* **1975**, *16*, 120–124.

(98) Flory, P. J. Thermodynamics of High Polymer Solutions. *J. Chem. Phys.* **1941**, *9*, 660.

(99) Huggins, M. L. Solutions of Long Chain Compounds. *J. Chem. Phys.* **1941**, *9*, 440.

(100) des Cloizeaux, J.; Jannink, G. *Polymers in Solution: Their Modeling and Structure*; Oxford Science Publications: Oxford, 1990.

(101) Duplantier, B. Lagrangian Tricritical Theory of Polymer Chain Solutions near the Θ -point. *J. Phys. (Paris)* **1982**, *43*, 991–1019.

(102) Wilding, N. B.; Müller, M.; Binder, K. Chain Length Dependence of the Polymer-Solvent Critical Point Parameters. *J. Chem. Phys.* **1996**, *105*, 802–809.

(103) Grassberger, P. Pruned-enriched Rosenbluth Method: Simulations of θ Polymers of Chain Length up to 1 000 000. *Phys. Rev. E: Stat. Phys., Plasmas, Fluids, Relat. Interdiscip. Top.* **1997**, *56*, 3682–3693.

(104) Hager, J.; Schäfer, L. Θ -point Behavior of Diluted Polymer Solutions: Can one observe the Universal Logarithmic Corrections predicted by Field Theory? *Phys. Rev. E: Stat. Phys., Plasmas, Fluids, Relat. Interdiscip. Top.* **1999**, *60*, 2071–2085.

(105) Cui, Z.; Hassankiadeh, N. T.; Lee, S. Y.; Lee, J. M.; Woo, K. T.; Sanguineti, A.; Arcella, V.; Lee, Y. M.; Drioli, E. Poly(vinylidene fluoride) Membrane Preparation with an Environmental Diluent via Thermally Induced Phase Separation. *J. Membr. Sci.* **2013**, *444*, 223–236.

(106) Song, S.-W.; Torkelson, J. M. Coarsening Effects on the Formation of Microporous Membranes produced via Thermally Induced Phase Separation of Polystyrene-Cyclohexanol Solutions. *J. Membr. Sci.* **1995**, *98*, 209–222.

(107) Berghmans, S.; Berghmans, H.; Meijer, H. E. H. Spinning of Hollow Porous Fibres via the TIPS Mechanism. *J. Membr. Sci.* **1996**, *116*, 171–189.

(108) Thankamony, R. L.; Li, X.; Fan, X.; Sheng, G.; Wang, X.; Sun, S.; Zhang, X.; Lai, Z. Preparation of Highly Porous Polymer Membranes with Hierarchical Porous Structures via Spinodal Decomposition of Mixed Solvents with UCST Phase Behavior. *ACS Appl. Mater. Interfaces* **2018**, *10*, 44041–44049.

(109) van Konynenburg, P. H.; Scott, R. L. Critical Lines and Phase Equilibria in Binary Van der Waals Mixtures. *Philos. Trans. R. Soc. A* **1980**, *298*, 496–540.

(110) Naughton, J. R.; Matsen, M. W. Limitations of the Dilution Approximation for Concentrated Block Copolymer/Solvent Mixtures. *Macromolecules* **2002**, *35*, 5688–5696.

(111) Joanny, J. F.; Leibler, L.; Ball, R. Is Chemical Mismatch important in Polymer Solutions. *J. Chem. Phys.* **1984**, *81*, 4640–4656.

(112) Schäfer, L.; Kappeler, C. A Renormalization-Group Analysis of Ternary Polymer-Solutions. *J. Phys. (Paris)* **1985**, *46*, 1853.

(113) Olvera de la Cruz, M. Theory of Microphase Separation in Block Copolymer Solutions. *J. Chem. Phys.* **1989**, *90*, 1995–2002.

(114) Schäfer, L.; Kappeler, C. Interaction Effects on the Size of a Polymer Chain in Ternary Solutions: A Renormalization Group Study. *J. Chem. Phys.* **1993**, *99*, 6135.

(115) Müller, M.; Binder, K.; Schäfer, L. Intra- and Interchain Correlations in Semidilute Polymer Solutions: Monte Carlo Simulations and Renormalization Group Results. *Macromolecules* **2000**, *33*, 4568–4580.

(116) Mai, Y.; Eisenberg, A. Self-Assembly of Block Copolymers. *Chem. Soc. Rev.* **2012**, *41*, 5969–5985.

- (117) Wong, C. K.; Qiang, X.; Müller, A. H. E.; Gröschel, A. H. Self-Assembly of Block Copolymers into Internally Ordered Microparticles. *Prog. Polym. Sci.* **2020**, *102*, 101211.
- (118) Gröschel, A. H.; Müller, A. H. E. Self-Assembly Concepts for Multicompartment Nanostructures. *Nanoscale* **2015**, *7*, 11841–11876.
- (119) Förster, S.; Khandpur, A. K.; Zhao, J.; Bates, F. S.; Hamley, I. W.; Ryan, A. J.; Bras, W. Complex Phase Behavior of Polyisoprene-Polystyrene Diblock Copolymers near the Order-Disorder Transition. *Macromolecules* **1994**, *27*, 6922–6935.
- (120) Breiner, U.; Krappe, U.; Stadler, R. Evolution of the “Knitting pattern” Morphology in ABC Triblock Copolymers. *Macromol. Rapid Commun.* **1996**, *17*, 567–575.
- (121) Janert, P. K.; Schick, M. Phase Behavior of Binary Homopolymer/Diblock Blends: Temperature and Chain Length Dependence. *Macromolecules* **1998**, *31*, 1109–1113.
- (122) Zhou, J.; Shi, A.-C. Microphase Separation induced by Differential Interactions in Diblock Copolymer/Homopolymer Blends. *J. Chem. Phys.* **2009**, *130*, 234904.
- (123) Helfand, E.; Tagami, Y. Theory of Interface between Immiscible Polymers. *J. Polym. Sci., Part B: Polym. Lett.* **1971**, *9*, 741.
- (124) Scheutjens, J. M. H. M.; Fleer, G. J. Statistical-Theory of the Adsorption of Interacting Chain Molecules. I. Partition-Function, Segment Density Distribution, and Adsorption-Isotherms. *J. Phys. Chem.* **1979**, *83*, 1619–1635.
- (125) Hong, K. M.; Noolandi, J. Theory of Inhomogeneous Multicomponent Polymer Systems. *Macromolecules* **1981**, *14*, 727–736.
- (126) Matsen, M. W.; Schick, M. Stable and Unstable Phases of a Diblock Copolymer Melt. *Phys. Rev. Lett.* **1994**, *72*, 2660–2663.
- (127) Shi, A. C.; Noolandi, J.; Desai, R. C. Theory of Anisotropic Fluctuations in Ordered Block Copolymer Phases. *Macromolecules* **1996**, *29*, 6487–6504.
- (128) Fredrickson, G. H. Dynamics and Rheology of Inhomogeneous Polymeric Fluids: A Complex Langevin Approach. *J. Chem. Phys.* **2002**, *117*, 6810–6820.
- (129) Fredrickson, G. H. *The Equilibrium Theory of Inhomogeneous Polymers*; Clarendon Press: Oxford, 2006.
- (130) Müller, M.; Schmid, F. Incorporating Fluctuations and Dynamics in Self-Consistent Field Theories for Polymer Blends. *Adv. Polym. Sci.* **2005**, *185*, 1–58.
- (131) Tyler, C. A.; Morse, D. C. Orthorhombic Fddd Network in Triblock and Diblock Copolymer Melts. *Phys. Rev. Lett.* **2005**, *94*, 208302.
- (132) Shi, A.-C.; Li, B. Self-Assembly of Diblock Copolymers under Confinement. *Soft Matter* **2013**, *9*, 1398–1413.
- (133) Matsen, M. W. The Standard Gaussian Model for Block Copolymer Melts. *J. Phys.: Condens. Matter* **2002**, *14*, R21–R47.
- (134) Xie, N.; Li, W.; Qiu, F.; Shi, A.-C. σ Phase Formed in Conformationally Asymmetric AB-Type Block Copolymers. *ACS Macro Lett.* **2014**, *3*, 906–910.
- (135) Müller, M.; Rey, J. C. O. Continuum Models for Directed Self-Assembly. *Mol. Syst. Des. Eng.* **2018**, *3*, 295–313.
- (136) Liu, J.; García-Cervera, C. J.; Delaney, K. T.; Fredrickson, G. H. Optimized Phase Field Model for Diblock Copolymer Melts. *Macromolecules* **2019**, *52*, 2878–2888.
- (137) Ohta, T.; Kawasaki, K. Equilibrium Morphology of Block Copolymer Melts. *Macromolecules* **1986**, *19*, 2621–2632.
- (138) Uneyama, T.; Doi, M. Density Functional Theory for Block Copolymer Melts and Blends. *Macromolecules* **2005**, *38*, 196–205.
- (139) Han, Y.; Xu, Z.; Shi, A.-C.; Zhang, L. Pathways Connecting two opposed Bilayers with a Fusion Pore: A Molecularly-Informed Phase Field Approach. *Soft Matter* **2020**, *16*, 366–374.
- (140) Strathmann, H.; Kock, K.; Amar, P.; Baker, R. W. The Formation Mechanism of Asymmetric Membranes. *Desalination* **1975**, *16*, 179–203.
- (141) Handge, U. A.; Gronwald, O.; Weber, M.; Koll, J.; Abetz, C.; Hankiewicz, B.; Abetz, V. Fabrication of Membranes of Polyethersulfone and Poly(N-vinyl pyrrolidone): Influence of Glycerol on Processing and Transport Properties. *Polym. Int.* **2020**, *69*, 502–512.
- (142) Smolders, C. A.; Reuvers, A. J.; Boom, R. M.; Wienk, I. M. Microstructures in Phase-Inversion Membranes. Part 1. Formation of Macrovoids. *J. Membr. Sci.* **1992**, *73*, 259–275.
- (143) de Gennes, P. G. Solvent Evaporation of Spin Cast Films: “Crust” Effects. *Eur. Phys. J. E: Soft Matter Biol. Phys.* **2002**, *7*, 31–34.
- (144) Okuzono, T.; Ozawa, K.; Doi, M. Simple Model of Skin Formation caused by Solvent Evaporation in Polymer Solutions. *Phys. Rev. Lett.* **2006**, *97*, 136103.
- (145) Tsige, M.; Grest, G. S. Molecular Dynamics Study of the Evaporation Process in Polymer Films. *Macromolecules* **2004**, *37*, 4333–4335.
- (146) Müller, M.; Smith, G. D. Phase Separation in Binary Mixtures containing Polymers: A quantitative Comparison of Single-Chain-in-Mean-Field Simulations and Computer Simulations of the corresponding Multichain Systems. *J. Polym. Sci., Part B: Polym. Phys.* **2005**, *43*, 934–958.
- (147) Peter, S.; Meyer, H.; Baschnagel, J. Molecular Dynamics Simulations of concentrated Polymer Solutions in thin Film Geometry. II. Solvent Evaporation near the glass transition. *J. Chem. Phys.* **2009**, *131*, 014903.
- (148) Tang, Q.; Müller, M. Evaporation-induced Liquid Expansion and Bubble Formation in binary Mixtures. *Phys. Rev. Lett.* **2021**, *126*, 028003.
- (149) Eisenriegler, E.; Kremer, K.; Binder, K. Adsorption of Polymer Chains at Surfaces - Scaling and Monte-Carlo Analyses. *J. Chem. Phys.* **1982**, *77*, 6296–6320.
- (150) Metzger, S.; Müller, M.; Binder, K.; Baschnagel, J. Surface Excess in dilute Polymer Solutions and the Adsorption Transition versus Wetting Phenomena. *J. Chem. Phys.* **2003**, *118*, 8489–8499.
- (151) Cahn, J. W. Critical-Point Wetting. *J. Chem. Phys.* **1977**, *66*, 3667–3672.
- (152) Müller, M.; MacDowell, L. G. Wetting of Polymer Liquids: Monte Carlo Simulations and Self-Consistent Field Calculations. *J. Phys.: Condens. Matter* **2003**, *15*, R609–R653.
- (153) Binder, K.; Landau, D.; Müller, M. Monte Carlo Studies of Wetting, Interface Localization and Capillary Condensation. *J. Stat. Phys.* **2003**, *110*, 1411–1514.
- (154) Nakanishi, K.; Tanaka, N. Sol-Gel with Phase Separation. Hierarchically Porous Materials Optimized for High-Performance Liquid Chromatography Separations. *Acc. Chem. Res.* **2007**, *40*, 863–873.
- (155) Wang, F.; Ratke, L.; Zhang, H.; Altschuh, P.; Nestler, B. A Phase-Field Study on Polymerization-Induced Phase Separation occasioned by Diffusion and Capillary Flow— A Mechanism for the Formation of Porous Microstructures in Membranes. *J. Sol-Gel Sci. Technol.* **2020**, *94*, 356–374.
- (156) Soler-Illia, G. J. d. A. A.; Sanchez, C.; Lebeau, B.; Patarin, J. Chemical Strategies to Design Textured Materials: From Microporous and Mesoporous Oxides to Nanonetworks and Hierarchical Structures. *Chem. Rev.* **2002**, *102*, 4093–4138.
- (157) Grosso, D.; Cagnol, F.; de A. Soler-Illia, G. J.; Crepaldi, E. L.; Amenitsch, H.; Brunet-Bruneau, A.; Bourgeois, A.; Sanchez, C. Fundamentals of Mesostructuring through Evaporation-Induced Self-Assembly. *Adv. Funct. Mater.* **2004**, *14*, 309–322.
- (158) Asghar, M. R.; Anwar, M. T.; Xia, G.; Zhang, J. Cellulose/Poly(vinylidene fluoride hexafluoropropylene) Composite Membrane with Titania Nanoparticles for Lithium-ion Batteries. *Mater. Chem. Phys.* **2020**, *252*, 123122.
- (159) Zhang, Z.; Rahman, Md. M.; Abetz, C.; Abetz, V. High-performance Asymmetric Isoporous Nanocomposite Membranes with Chemically-tailored Amphiphilic Nanochannels. *J. Mater. Chem. A* **2020**, *8*, 9554–9566.
- (160) Cahn, J. W. Free Energy of a Nonuniform System. II. Thermodynamic Basis. *J. Chem. Phys.* **1959**, *30*, 1121–1124.
- (161) de Gennes, P. G. *Scaling Concepts in Polymer Physics*; Cornell University Press: Ithaca and London, 1979.
- (162) Lifshitz, I. M.; Grosberg, A. Y.; Khokhlov, A. R. Some Problems of Statistical Physics of Polymer-Chains with Volume Interaction. *Rev. Mod. Phys.* **1978**, *50*, 683–713.

- (163) Yethiraj, A.; Woodward, C. E. Monte Carlo Density Functional Theory of Nonuniform Polymer Melts. *J. Chem. Phys.* **1995**, *102*, 5499–5505.
- (164) Yu, Y.-X.; Wu, J. Density Functional Theory for Inhomogeneous Mixtures of Polymeric Fluids. *J. Chem. Phys.* **2002**, *117*, 2368–2376.
- (165) Müller, M.; MacDowell, L. G. Interface and Surface Properties of Short Polymers in Solution: Monte Carlo Simulations and Self-Consistent Field Theory. *Macromolecules* **2000**, *33*, 3902–3923.
- (166) Frischknecht, A. L.; Weinhold, J. D.; Salinger, A. G.; Curro, J. G.; Douglas Frink, L. J.; McCoy, J. D. Density Functional Theory for Inhomogeneous Polymer Systems. I. Numerical Methods. *J. Chem. Phys.* **2002**, *117*, 10385–10397.
- (167) Müller, M.; MacDowell, L. G.; Yethiraj, A. Short Chains at Surfaces and Interfaces: a Quantitative Comparison between Density-Functional Theories and Monte Carlo Simulations. *J. Chem. Phys.* **2003**, *118*, 2929–2940.
- (168) Wu, J. Density Functional Theory for Chemical Engineering: From Capillarity to Soft Materials. *AIChE J.* **2006**, *52*, 1169–1193.
- (169) Tree, D. R.; Dos Santos, L. F.; Wilson, C. B.; Scott, T. R.; Garcia, J. U.; Fredrickson, G. H. Mass-transfer driven Spinodal Decomposition in a Ternary Polymer Solution. *Soft Matter* **2019**, *15*, 4614–4628.
- (170) Doi, M.; Onuki, A. Dynamic Coupling between Stress and Composition in Polymer Solutions and Blends. *J. Phys. II* **1992**, *2*, 1631–1656.
- (171) Tanaka, H. Viscoelastic Phase Separation. *J. Phys.: Condens. Matter* **2000**, *12*, R207.
- (172) Hohenberg, P. C.; Halperin, B. I. Theory of Dynamic Critical Phenomena. *Rev. Mod. Phys.* **1977**, *49*, 435–479.
- (173) Semenov, A. Relaxation of Long-Wavelength Density Fluctuations in a Concentrated Polymer Solution. *JETP* **1986**, *63*, 1230.
- (174) Wang, G.; Ren, Y.; Müller, M. Collective Short-Time Dynamics in Multicomponent Polymer Melts. *Macromolecules* **2019**, *52*, 7704–7720.
- (175) Rottler, J.; Müller, M. Kinetic Pathways of Block Copolymer Directed Self-Assembly: Insights from Efficient Continuum Modeling. *ACS Nano* **2020**, *14*, 13986–13994.
- (176) Brochard, F.; de Gennes, P. Dynamics of Compatible Polymer Mixtures. *Phys. A* **1983**, *118*, 289–299.
- (177) Akcasu, A.; Benmouna, M.; Benoit, H. Application of Random Phase Approximation to the Dynamics of Polymer Blends and Copolymers. *Polymer* **1986**, *27*, 1935–1942.
- (178) Benmouna, M.; Benoit, H.; Duval, M.; Akcasu, Z. Theory of Dynamic Scattering from Ternary Mixtures of two Homopolymers and a Solvent. *Macromolecules* **1987**, *20*, 1107–1112.
- (179) de Gennes, P. G. Dynamics of Fluctuations and Spinodal Decomposition in Polymer Blends. *J. Chem. Phys.* **1980**, *72*, 4756–4763.
- (180) Foard, E. M.; Wagner, A. J. Enslaved Phase-Separation Fronts in One-dimensional Binary Mixtures. *Phys. Rev. E* **2009**, *79*, 056710.
- (181) Foard, E. M.; Wagner, A. J. Survey of Morphologies formed in the Wake of an Enslaved Phase-Separation Front in Two Dimensions. *Phys. Rev. E* **2012**, *85*, 011501.
- (182) Hopp-Hirschler, M.; Nieken, U. Modeling of Pore Formation in Phase Inversion Processes: Model and Numerical Results. *J. Membr. Sci.* **2018**, *564*, 820–831.
- (183) Tree, D. R.; Delaney, K. T.; Cenicerros, H. D.; Iwama, T.; Fredrickson, G. H. A Multi-Fluid Model for Microstructure Formation in Polymer Membranes. *Soft Matter* **2017**, *13*, 3013–3030.
- (184) de la Torre, J. A.; Español, P.; Donev, A. Finite Element Discretization of non-linear Diffusion Equations with Thermal Fluctuations. *J. Chem. Phys.* **2015**, *142*, 094115.
- (185) Müller, M.; MacDowell, L. G.; Virnau, P.; Binder, K. Interface Properties and Bubble Nucleation in Compressible Mixtures containing Polymers. *J. Chem. Phys.* **2002**, *117*, 5480–5496.
- (186) Spencer, R. K. W.; Curry, P. F.; Wickham, R. A. Nucleation of the BCC Phase from Disorder in a Diblock Copolymer Melt: Testing approximate Theories through Simulation. *J. Chem. Phys.* **2016**, *145*, 144902.
- (187) Wickham, R. A.; Shi, A.-C.; Wang, Z.-G. Nucleation of Stable Cylinders from a Metastable Lamellar Phase in a Diblock Copolymer Melt. *J. Chem. Phys.* **2003**, *118*, 10293–10305.
- (188) Cheng, X.; Lin, L.; E, W.; Zhang, P.; Shi, A.-C. Nucleation of Ordered Phases in Block Copolymers. *Phys. Rev. Lett.* **2010**, *104*, 148301.
- (189) Binder, K. Nucleation Barriers, Spinodals and the Ginzburg Criterion. *Phys. Rev. A: At., Mol., Opt. Phys.* **1984**, *29*, 341–349.
- (190) Wang, Z.-G. Concentration Fluctuation in Binary Polymer Blends: χ Parameter, Spinodal and Ginzburg criterion. *J. Chem. Phys.* **2002**, *117*, 481.
- (191) Ting, C. L.; Müller, M. Membrane Stress Profiles from Self-Consistent Field Theory. *J. Chem. Phys.* **2017**, *146*, 104901.
- (192) Milner, S. T. Dynamical Theory of Concentration Fluctuations in Polymer Solutions under Shear. *Phys. Rev. E: Stat. Phys., Plasmas, Fluids, Relat. Interdiscip. Top.* **1993**, *48*, 3674–3691.
- (193) Nittmann, J.; Daccord, G.; Stanley, H. E. Fractal Growth Viscous Fingers: Quantitative Characterization of a Fluid Instability Phenomenon. *Nature* **1985**, *314*, 141–144.
- (194) Kessler, D. A.; Koplik, J.; Levine, H. Pattern Selection in Fingered Growth Phenomena. *Adv. Phys.* **1988**, *37*, 255–339.
- (195) Taniguchi, T.; Onuki, A. Network Domain Structure in Viscoelastic Phase Separation. *Phys. Rev. Lett.* **1996**, *77*, 4910–4913.
- (196) Sarti, G. C.; Marrucci, G. Thermomechanics of Dilute Polymer Solutions: Multiple Bead-Spring Model. *Chem. Eng. Sci.* **1973**, *28*, 1053–1059.
- (197) Booij, H. C. The Energy Storage in the Rouse model in an arbitrary Flow Field. *J. Chem. Phys.* **1984**, *80*, 4571–4572.
- (198) Ilg, P.; Kröger, M. Molecularly Derived Constitutive Equation for Low-molecular Polymer Melts from thermodynamically guided Simulation. *J. Rheol.* **2011**, *55*, 69.
- (199) Mavrantzas, V. G.; Theodorou, D. N. Atomistic Simulation of Polymer Melt Elasticity: Calculation of the Free Energy of an Oriented Polymer Melt. *Macromolecules* **1998**, *31*, 6310–6332.
- (200) Mavrantzas, V. G.; Öttinger, H. C. Atomistic Monte Carlo Simulations of Polymer Melt Elasticity: Their Nonequilibrium Thermodynamics GENERIC Formulation in a Generalized Canonical Ensemble. *Macromolecules* **2002**, *35*, 960–975.
- (201) Müller, M.; Sollich, P.; Sun, D.-W. Nonequilibrium Molecular Conformations in Polymer Self-Consistent Field Theory. *Macromolecules* **2020**, *53*, 10457–10474.
- (202) Onuki, A.; Taniguchi, T. Viscoelastic Effects in Early Stage Phase Separation in Polymeric Systems. *J. Chem. Phys.* **1997**, *106*, 5761–5770.
- (203) Binder, K.; Frisch, H. L.; Jäcke, J. Kinetics of Phase Separation in the Presence of Slowly Relaxing Structural Variables. *J. Chem. Phys.* **1986**, *85*, 1505–1512.
- (204) Sappelt, D.; Jäcke, J. Spinodal Decomposition with Formation of a Glassy Phase. *EPL* **1997**, *37*, 13–18.
- (205) Barton, B. F.; Graham, P. D.; McHugh, A. J. Dynamics of Spinodal Decomposition in Polymer Solutions near a Glass Transition. *Macromolecules* **1998**, *31*, 1672–1679.
- (206) Garcia, J. U.; Iwama, T.; Chan, E. Y.; Tree, D. R.; Delaney, K. T.; Fredrickson, G. H. Mechanisms of Asymmetric Membrane Formation in Nonsolvent-Induced Phase Separation. *ACS Macro Lett.* **2020**, *9*, 1617–1624.
- (207) Araki, T.; Tanaka, H. Three-Dimensional Numerical Simulations of Viscoelastic Phase Separation: Morphological Characteristics. *Macromolecules* **2001**, *34*, 1953–1963.
- (208) Testard, V.; Berthier, L.; Kob, W. Influence of the Glass Transition on the Liquid-Gas Spinodal Decomposition. *Phys. Rev. Lett.* **2011**, *106*, 125702.
- (209) Olais-Govea, J. M.; López-Flores, L.; Medina-Noyola, M. Non-Equilibrium Theory of Arrested Spinodal Decomposition. *J. Chem. Phys.* **2015**, *143*, 174505.
- (210) Flory, P. J. Statistical Thermodynamics of Random Networks. *Proc. R. Soc. London A* **1976**, *351*, 351–380.
- (211) Rubinstein, M.; Panyukov, S. Elasticity of Polymer Networks. *Macromolecules* **2002**, *35*, 6670–6686.

- (212) Dobrynin, A. V.; Carrillo, J.-M. Y. Universality in Nonlinear Elasticity of Biological and Polymeric Networks and Gels. *Macromolecules* **2011**, *44*, 140–146.
- (213) Chassé, W.; Lang, M.; Sommer, J.-U.; Saalwächter, K. Cross-Link Density Estimation of PDMS Networks with Precise Consideration of Networks Defects. *Macromolecules* **2012**, *45*, 899–912.
- (214) Everaers, R. Topological versus Rheological Entanglement Length in Primitive-Path Analysis Protocols, Tube Models, and Slip-Link Models. *Phys. Rev. E* **2012**, *86*, 022801.
- (215) Zhong, M.; Wang, R.; Kawamoto, K.; Olsen, B. D.; Johnson, J. A. Quantifying the Impact of Molecular Defects on Polymer Network Elasticity. *Science* **2016**, *353*, 1264–1268.
- (216) Creton, C. 50th Anniversary Perspective: Networks and Gels: Soft but Dynamic and Tough. *Macromolecules* **2017**, *50*, 8297–8316.
- (217) Lang, M. Elasticity of Phantom Model Networks with Cyclic Defects. *ACS Macro Lett.* **2018**, *7*, 536–539.
- (218) Long, Y.; Shanks, R. A.; Stachurski, Z. H. Kinetics of Polymer Crystallisation. *Prog. Polym. Sci.* **1995**, *20*, 651–701.
- (219) Muthukumar, M. Commentary on Theories of Polymer Crystallization. *Eur. Phys. J. E: Soft Matter Biol. Phys.* **2000**, *3*, 199–202.
- (220) Welch, P.; Muthukumar, M. Molecular Mechanisms of Polymer Crystallization from Solution. *Phys. Rev. Lett.* **2001**, *87*, 218302.
- (221) Hu, W.; Frenkel, D. *Interphases and Mesophases in Polymer Crystallization III*; Springer: Berlin, Germany, 2005; pp 1–35.
- (222) Strobl, G. Colloquium: Laws Controlling Crystallization and Melting in Bulk Polymers. *Rev. Mod. Phys.* **2009**, *81*, 1287–1300.
- (223) Luo, C.; Sommer, J.-U. Growth Pathway and Precursor States in Single Lamellar Crystallization: MD Simulations. *Macromolecules* **2011**, *44*, 1523–1529.
- (224) Tang, Q.; Müller, M.; Li, C. Y.; Hu, W. Anomalous Ostwald Ripening enables 2D Polymer Crystals via Fast Evaporation. *Phys. Rev. Lett.* **2019**, *123*, 207801.
- (225) Baschnagel, J.; Binder, K.; Doruker, P.; Gusev, A. A.; Hahn, O.; Kremer, K.; Mattice, W. L.; Müller-Plathe, F.; Murat, M.; Paul, W.; Santos, S.; Suter, U. W.; Tries, V. Bridging the Gap between Atomistic and Coarse-Grained Models of Polymers: Status and Perspectives. *Adv. Polym. Sci.* **2000**, *152*, 41–156.
- (226) Müller-Plathe, F. Coarse-Graining in Polymer Simulation: From the Atomistic To the Mesoscopic Scale and Back. *ChemPhysChem* **2002**, *3*, 754–769.
- (227) Müller, M. Studying Amphiphilic Self-Assembly with Soft Coarse-Grained Models. *J. Stat. Phys.* **2011**, *145*, 967.
- (228) Praprotnik, M.; Delle Site, L.; Kremer, K. Multiscale Simulation of Soft Matter: from Scale Bridging to Adaptive Resolution. *Annu. Rev. Phys. Chem.* **2008**, *59*, 545–571.
- (229) Noid, W. G. Perspective: Coarse-Grained Models for Biomolecular Systems. *J. Chem. Phys.* **2013**, *139*, 090901.
- (230) Foley, T. T.; Shell, M. S.; Noid, W. G. The Impact of Resolution upon Entropy and Information in Coarse-Grained Models. *J. Chem. Phys.* **2015**, *143*, 243104.
- (231) Cheng, S.; Grest, G. S. Dispersing Nanoparticles in a Polymer Film via Solvent Evaporation. *ACS Macro Lett.* **2016**, *5*, 694–698.
- (232) Statt, A.; Howard, M. P.; Panagiotopoulos, A. Z. Solvent Quality Influences Surface Structure of Glassy Polymer Thin Films after Evaporation. *J. Chem. Phys.* **2017**, *147*, 184901.
- (233) Howard, M. P.; Nikoubashman, A.; Panagiotopoulos, A. Z. Stratification in Drying Polymer-Polymer and Colloid-Polymer Mixtures. *Langmuir* **2017**, *33*, 11390–11398.
- (234) Marrink, S. J.; Risselada, H. J.; Yefimov, S.; Tieleman, D. P.; de Vries, A. H. The Martini Force Field: Coarse Grained Model for Biomolecular Simulations. *J. Phys. Chem. B* **2007**, *111*, 7812–7824.
- (235) Tang, Y.-h.; Ledieu, E.; Cervellere, M. R.; Millett, P. C.; Ford, D. M.; Qian, X. Formation of Polyethersulfone Membranes via Non-solvent induced Phase Separation Process from Dissipative Particle Dynamics Simulations. *J. Membr. Sci.* **2020**, *599*, 117826.
- (236) Langenberg, M.; Jackson, N. E.; de Pablo, J. J.; Müller, M. Role of Translational Entropy in Spatially Inhomogeneous, Coarse-Grained Models. *J. Chem. Phys.* **2018**, *148*, 094112.
- (237) Pagonabarraga, I.; Frenkel, D. Dissipative Particle Dynamics for Interacting Systems. *J. Chem. Phys.* **2001**, *115*, 5015–5026.
- (238) Trofimov, S. Y.; Nies, E. L. F.; Michels, M. A. J. Thermodynamic Consistency in Dissipative Particle Dynamics Simulations of strongly Nonideal Liquids and Liquid Mixtures. *J. Chem. Phys.* **2002**, *117*, 9383–9394.
- (239) Hoogerbrugge, P. J.; Koelman, J. M. V. A. Simulating Microscopic Hydrodynamics Phenomena with Dissipative Particle Dynamics. *Europhys. Lett.* **1992**, *19*, 155.
- (240) Espanol, P. Hydrodynamics from Dissipative Particle Dynamics. *Phys. Rev. E: Stat. Phys., Plasmas, Fluids, Relat. Interdiscip. Top.* **1995**, *52*, 1734.
- (241) Groot, R. D.; Warren, P. B. Dissipative Particle Dynamics: Bridging the Gap between Atomistic and Mesoscopic Simulation. *J. Chem. Phys.* **1997**, *107*, 4423–4435.
- (242) Espanol, P.; Warren, P. B. Perspective: Dissipative particle dynamics. *J. Chem. Phys.* **2017**, *146*, 150901.
- (243) Padding, J. T.; Briels, W. J. Uncrossability Constraints in Mesoscopic Polymer Melt Simulations: Non-Rouse Behavior of C₂₀H₄₂. *J. Chem. Phys.* **2001**, *115*, 2846–2859.
- (244) Kumar, S.; Larson, R. G. Brownian Dynamics Simulations of Flexible Polymers with Spring-Spring Repulsions. *J. Chem. Phys.* **2001**, *114*, 6937–6941.
- (245) Nikunen, P.; Vattulainen, I.; Karttunen, M. Reptational Dynamics in Dissipative Particle Dynamics Simulations of Polymer Melts. *Phys. Rev. E* **2007**, *75*, 036713.
- (246) Sirk, T. W.; Slizoberg, Y. R.; Brennan, J. K.; Lisal, M.; Andzelm, J. W. An enhanced Entangled Polymer Model for Dissipative Particle Dynamics. *J. Chem. Phys.* **2012**, *136*, 134903.
- (247) Chen, S.; Olson, E.; Jiang, S.; Yong, X. Nanoparticle Assembly modulated by Polymer Chain Conformation in Composite Materials. *Nanoscale* **2020**, *12*, 14560–14572.
- (248) Korolkovas, A.; Gutfreund, P.; Barrat, J.-L. Simulation of Entangled Polymer Solutions. *J. Chem. Phys.* **2016**, *145*, 124113.
- (249) Chappa, V. C.; Morse, D. C.; Zippelius, A.; Müller, M. Translationally Invariant Slip-Spring Model for Entangled Polymer Dynamics. *Phys. Rev. Lett.* **2012**, *109*, 148302.
- (250) Uneyama, T.; Masubuchi, Y. Multi-chain Slip-Spring model for Entangled Polymer Dynamics. *J. Chem. Phys.* **2012**, *137*, 154902.
- (251) Masubuchi, Y.; Langeloth, M.; Böhm, M. C.; Inoue, T.; Müller-Plathe, F. A Multichain Slip-Spring Dissipative Particle Dynamics Simulation Method for Entangled Polymer Solutions. *Macromolecules* **2016**, *49*, 9186–9191.
- (252) Ramirez-Hernandez, A.; Peters, B. L.; Schneider, L.; Andreev, M.; Schieber, J. D.; Müller, M.; Kröger, M.; de Pablo, J. J. A Detailed Examination of the Topological Constraints of Lamellae-Forming Block Copolymers. *Macromolecules* **2018**, *51*, 2110–2124.
- (253) Behbahani, A. F.; Schneider, L.; Rissanou, A.; Chazirakis, A.; Bačová, P.; Jana, P. K.; Li, W.; Doxastakis, M.; Políńska, P.; Burkhart, C.; Müller, M.; Harmandaris, V. A. Dynamics and Rheology of Polymer Melts via Hierarchical Atomistic, Coarse-Grained, and Slip-Spring Simulations. *Macromolecules* **2021**, *54*, 2740–2762.
- (254) Daoulas, K. C.; Müller, M. Single Chain in Mean Field simulations: Quasi-instantaneous Field Approximation and Quantitative Comparison with Monte Carlo Simulations. *J. Chem. Phys.* **2006**, *125*, 184904.
- (255) Schneider, L.; Müller, M. Multi-Architecture Monte-Carlo (MC) Simulation of Soft Coarse-Grained Polymeric Materials: SOFT coarse grained Monte-carlo Acceleration (SOMA). *Comput. Phys. Commun.* **2019**, *235*, 463.
- (256) E, W.; Engquist, B.; Li, X. T.; Ren, W. Q.; Vanden-Eijnden, E. Heterogeneous Multiscale Methods: A Review. *Comm. Computational Phys.* **2007**, *2*, 367–450.
- (257) Pego, R. L. Front Migration in the Nonlinear Cahn-Hilliard Equation. *Proc. R. Soc. London A* **1989**, *422*, 261–278.
- (258) Elder, K. R.; Grant, M.; Provatas, N.; Kosterlitz, J. M. Sharp Interface Limits of Phase-Field Models. *Phys. Rev. E: Stat. Phys., Plasmas, Fluids, Relat. Interdiscip. Top.* **2001**, *64*, 021604.

- (259) Magaletti, F.; Picano, F.; Chinappi, M.; Marino, L.; Casciola, C. M. The Sharp-Interface limit of the Cahn-Hilliard/Navier-Stokes Model for Binary Fluids. *J. Fluid Mech.* **2013**, *714*, 95–126.
- (260) Reuvers, A. J.; van den Berg, J. W. A.; Smolders, C. A. Formation of Membranes by means of Immersion Precipitation: Part I. A Model to describe Mass Transfer during Immersion Precipitation. *J. Membr. Sci.* **1987**, *34*, 45–65.
- (261) Dabral, M.; Francis, L. F.; Scriven, L. E. Drying Process Paths of Ternary Polymer Solution Coating. *AIChE J.* **2002**, *48*, 25–37.
- (262) Paradiso, S. P.; Delaney, K. T.; Garcia-Cervera, C. J.; Cenicerros, H. D.; Fredrickson, G. H. Block Copolymer Self Assembly during Rapid Solvent Evaporation: Insights into Cylinder Growth and Stability. *ACS Macro Lett.* **2014**, *3*, 16–20.
- (263) Lewis, W. K.; Whitman, W. G. Principles of Gas Absorption. *Ind. Eng. Chem.* **1924**, *16*, 1215–1220.
- (264) Prosperetti, A.; Plesset, M. S. The Stability of an Evaporating Liquid Surface. *Phys. Fluids* **1984**, *27*, 1590–1602.
- (265) Stegelmeier, C.; Filiz, V.; Abetz, V.; Perlich, J.; Fery, A.; Ruckdeschel, P.; Rosenfeldt, S.; Förster, S. Topological Paths and Transient Morphologies during Formation of Mesoporous Block Copolymer Membranes. *Macromolecules* **2014**, *47*, 5566–5577.
- (266) Wijmans, J. G.; Altena, F. W.; Smolders, C. A. Diffusion during the Immersion Precipitation Process. *J. Polym. Sci., Polym. Phys. Ed.* **1984**, *22*, 519–524.
- (267) McHugh, A. J.; Yilmaz, L. The Diffusion Equations for Polymer Membrane Formation in Ternary Systems. *J. Polym. Sci., Polym. Phys. Ed.* **1985**, *23*, 1271–1274.
- (268) Yilmaz, L.; McHugh, A. J. Modelling of Asymmetric Membrane Formation. I. Critique of Evaporation Models and Development of a Diffusion Equation Formalism for the Quench Period. *J. Membr. Sci.* **1986**, *28*, 287–310.
- (269) Yilmaz, L.; McHugh, A. J. Modeling of Asymmetric Membrane Formation. II. The Effects of Surface Boundary Conditions. *J. Appl. Polym. Sci.* **1988**, *35*, 1967–1979.
- (270) Tsay, C. S.; McHugh, A. J. Mass Transfer Modeling of Asymmetric Membrane Formation by Phase Inversion. *J. Polym. Sci., Part B: Polym. Phys.* **1990**, *28*, 1327–1365.
- (271) Cheng, L.-P.; Soh, Y. S.; Dwan, A.-H.; Gryte, C. C. An Improved Model for Mass Transfer during the Formation of Polymeric Membranes by the Immersion-Precipitation Process. *J. Polym. Sci., Part B: Polym. Phys.* **1994**, *32*, 1413–1425.
- (272) Strathmann, H.; Kock, K. The Formation Mechanism of Phase Inversion Membranes. *Desalination* **1977**, *21*, 241–255.
- (273) Schick, M. *Les Houches Lectures on "Liquids at Interfaces"*; Elsevier Science Publishers: Amsterdam, 1990; pp 1–89.
- (274) Zhou, B.; Powell, A. C. Phase Field Simulations of Early Stage Structure Formation during Immersion Precipitation of Polymeric Membranes in 2D and 3D. *J. Membr. Sci.* **2006**, *268*, 150–164.
- (275) Ball, R. C.; Essery, R. L. H. Spinodal Decomposition and Pattern Formation near Surfaces. *J. Phys.: Condens. Matter* **1990**, *2*, 10303–10320.
- (276) Puri, S.; Frisch, H. L. Surface-directed Spinodal Decomposition: Modelling and Numerical simulations. *J. Phys.: Condens. Matter* **1997**, *9*, 2109–2133.
- (277) Akthakul, A.; Scott, C. E.; Mayes, A. M.; Wagner, A. J. Lattice Boltzmann Simulation of Asymmetric Membrane Formation by Immersion Precipitation. *J. Membr. Sci.* **2005**, *249*, 213–226.
- (278) Tree, D. R.; Iwama, T.; Delaney, K. T.; Lee, J.; Fredrickson, G. H. Marangoni Flows during Nonsolvent Induced Phase Separation. *ACS Macro Lett.* **2018**, *7*, 582–586.
- (279) Siggia, E. Late Stages of Spinodal Decomposition. *Phys. Rev. A: At., Mol., Opt. Phys.* **1979**, *20*, 595.
- (280) Lifshitz, I. M.; Slyozov, V. V. The Kinetics of Precipitation from Supersaturated Solid Solutions. *J. Phys. Chem. Solids* **1961**, *19*, 35.
- (281) Wagner, C. Theorie der Alterung von Niederschlägen durch Umlösen. *Z. Elektrochem.* **1961**, *65*, 581.
- (282) Matz, R. The Structure of Cellulose Acetate Membranes I. The Development of Porous Structures in Anisotropic Membranes. *Desalination* **1972**, *10*, 1–15.
- (283) Frommer, M. A.; Messalem, R. M. Mechanism of Membrane Formation. VI. Convective Flows and Large Void Formation during Membrane Precipitation. *Product R&D* **1973**, *12*, 328–333.
- (284) Sternling, C. V.; Scriven, L. E. Interfacial Turbulence: Hydrodynamic Instability and the Marangoni Effect. *AIChE J.* **1959**, *5*, 514–523.
- (285) Ray, R. J.; Krantz, W. B.; Sani, R. L. Linear Stability Theory Model for Finger Formation in Asymmetric Membranes. *J. Membr. Sci.* **1985**, *23*, 155–182.
- (286) van Saarloos, W. Front Propagation into Unstable States. *Phys. Rep.* **2003**, *386*, 29–222.
- (287) Yoshimoto, K.; Taniguchi, T. Viscoelastic Phase Separation Model for Ternary Polymer Solutions. *J. Chem. Phys.* **2021**, *154*, 104903.
- (288) Termonia, Y. Monte Carlo Diffusion Model of Polymer Coagulation. *Phys. Rev. Lett.* **1994**, *72*, 3678–3681.
- (289) Termonia, Y. Fundamentals of Polymer Coagulation. *J. Polym. Sci., Part B: Polym. Phys.* **1995**, *33*, 279–288.
- (290) Termonia, Y. Molecular Modeling of Phase-inversion Membranes: Effect of Additives in the Coagulant. *J. Membr. Sci.* **1995**, *104*, 173–179.
- (291) Han, Y.; Wang, J.; Zhang, H. Effects of Kinetics Coefficients on Ternary Phase Separation during the Wet Spinning Process. *J. Appl. Polym. Sci.* **2012**, *125*, 3630–3637.
- (292) Termonia, Y. Coagulation of a Polymer Solution: Effect of Initial Dispersion of Polymer in Solvent. *J. Polym. Sci., Part B: Polym. Phys.* **1998**, *36*, 2493–2497.
- (293) He, X.; Chen, C.; Jiang, Z.; Su, Y. Computer Simulation of Formation of Polymeric Ultrafiltration Membrane via Immersion Precipitation. *J. Membr. Sci.* **2011**, *371*, 108–116.
- (294) Tang, Y.-h.; He, Y.-d.; Wang, X.-l. Three-dimensional Analysis of Membrane Formation via Thermally Induced Phase Separation by Dissipative Particle Dynamics Simulation. *J. Membr. Sci.* **2013**, *437*, 40–48.
- (295) Wang, X.-L.; Qian, H.-J.; Chen, L.-J.; Lu, Z.-Y.; Li, Z.-S. Dissipative Particle Dynamics Simulation on the Polymer Membrane Formation by Immersion Precipitation. *J. Membr. Sci.* **2008**, *311*, 251–258.
- (296) Lin, H.-h.; Tang, Y.-h.; Matsuyama, H.; Wang, X.-l. Dissipative Particle Dynamics Simulation on the Membrane Formation of Polymer-Solvent System via Nonsolvent Induced Phase Separation. *J. Membr. Sci.* **2018**, *548*, 288–297.
- (297) Huo, J.; Chen, Z.; Zhou, J. Zwitterionic Membrane via Nonsolvent Induced Phase Separation: A Computer Simulation Study. *Langmuir* **2019**, *35*, 1973–1983.
- (298) Abetz, V. Isoporous Block Copolymer Membranes. *Macromol. Rapid Commun.* **2015**, *36*, 10–22.
- (299) Hahn, J.; Clodt, J. I.; Abetz, C.; Filiz, V.; Abetz, V. Thin Isoporous Block Copolymer Membranes: It Is All about the Process. *ACS Appl. Mater. Interfaces* **2015**, *7*, 21130–21137.
- (300) Radjabian, M.; Koll, J.; Buhr, K.; Handge, U. A.; Abetz, V. Hollow Fiber Spinning of Block Copolymers: Influence of Spinning Conditions on Morphological Properties. *Polymer* **2013**, *54*, 1803–1812.
- (301) Radjabian, M.; Koll, J.; Buhr, K.; Vainio, U.; Abetz, C.; Handge, U. A.; Abetz, V. Tailoring the Morphology of Self-Assembled Block Copolymer Hollow Fiber Membranes. *Polymer* **2014**, *55*, 2986–2997.
- (302) Hilke, R.; Pradeep, N.; Behzad, A. R.; Nunes, S. P.; Peinemann, K.-V. Block Copolymer/Homopolymer Dual-Layer Hollow Fiber Membranes. *J. Membr. Sci.* **2014**, *472*, 39–44.
- (303) Noor, N.; Koll, J.; Radjabian, M.; Abetz, C.; Abetz, V. A Facile Method to Prepare Double-Layer Isoporous Hollow Fiber Membrane by In Situ Hydrogen Bond Formation in the Spinning Line. *Macromol. Rapid Commun.* **2016**, *37*, 414–419.
- (304) Sankhala, K.; Wieland, D. C. F.; Koll, J.; Radjabian, M.; Abetz, C.; Abetz, V. Self-Assembly of Block Copolymers during Hollow Fiber Spinning: An in Situ Small-Angle X-ray Scattering Study. *Nanoscale* **2019**, *11*, 7634–7647.

- (305) Sankhala, K.; Koll, J.; Radjabin, M.; Handge, U. A.; Abetz, V. A Pathway to Fabricate Hollow Fiber Membranes with Isoporous Inner Surface. *Adv. Mater. Interfaces* **2017**, *4*, 1600991.
- (306) Sankhala, K.; Koll, J.; Abetz, V. Setting the Stage for Fabrication of Self-Assembled Structures in Compact Geometries: Inside-Out Isoporous Hollow Fiber Membranes. *ACS Macro Lett.* **2018**, *7*, 840–845.
- (307) Rangou, S.; Buhr, K.; Filiz, V.; Clodt, J. I.; Lademann, B.; Hahn, J.; Jung, A.; Abetz, V. Self-Organized Isoporous Membranes with Tailored Pore Sizes. *J. Membr. Sci.* **2014**, *451*, 266–275.
- (308) Radjabin, M.; Abetz, V. Tailored Pore Sizes in Integral Asymmetric Membranes Formed by Blends of Block Copolymers. *Adv. Mater.* **2015**, *27*, 352–355.
- (309) Zhang, Q.; Li, Y. M.; Gu, Y.; Dorin, R. M.; Wiesner, U. Tuning Substructure and Properties of Supported Asymmetric Triblock Terpolymer Membranes. *Polymer* **2016**, *107*, 398–405.
- (310) Sutisna, B.; Polymeropoulos, G.; Musteata, V.; Peinemann, K.-V.; Avgeropoulos, A.; Smilgies, D.-M.; Hadjichristidis, N.; Nunes, S. P. Design of Block Copolymer Membranes using Segregation Strength Trend Lines. *Mol. Syst. Des. Eng.* **2016**, *1*, 278–289.
- (311) Sankhala, K.; Koll, J.; Abetz, V. Facilitated Structure Formation in Isoporous Block Copolymer Membranes upon Controlled Evaporation by Gas Flow. *Membranes* **2020**, *10*, 83.
- (312) Dorin, R. M.; Marques, D. S.; Sai, H.; Vainio, U.; Phillip, W. A.; Peinemann, K.-V.; Nunes, S. P.; Wiesner, U. Solution Small-Angle X-ray Scattering as a Screening and Predictive Tool in the Fabrication of Asymmetric Block Copolymer Membranes. *ACS Macro Lett.* **2012**, *1*, 614–617.
- (313) Nunes, S. P.; Sougrat, R.; Hooghan, B.; Anjum, D. H.; Behzad, A. R.; Zhao, L.; Pradeep, N.; Pinnau, I.; Vainio, U.; Peinemann, K.-V. Ultraporos Films with Uniform Nanochannels by Block Copolymer Micelles Assembly. *Macromolecules* **2010**, *43*, 8079–8085.
- (314) Gallei, M.; Rangou, S.; Filiz, V.; Buhr, K.; Bolmer, S.; Abetz, C.; Abetz, V. The Influence of Magnesium Acetate on the Structure Formation of Polystyrene-block-poly(4-vinylpyridine)-based Integral-Asymmetric Membranes. *Macromol. Chem. Phys.* **2013**, *214*, 1037–1046.
- (315) Clodt, J. I.; Rangou, S.; Schröder, A.; Buhr, K.; Hahn, J.; Jung, A.; Filiz, V.; Abetz, V. Carbohydrates as Additives for the Formation of Isoporous PS-*b*-P4VP Diblock Copolymer Membranes. *Macromol. Rapid Commun.* **2013**, *34*, 190–194.
- (316) Madhavan, P.; Peinemann, K.-V.; Nunes, S. P. Complexation-Tailored Morphology of Asymmetric Block Copolymer Membranes. *ACS Appl. Mater. Interfaces* **2013**, *5*, 7152–7159.
- (317) Hahn, J.; Filiz, V.; Rangou, S.; Clodt, J.; Jung, A.; Buhr, K.; Abetz, C.; Abetz, V. Structure Formation of Integral-Asymmetric Membranes of Polystyrene-block-Poly(ethylene oxide). *J. Polym. Sci., Part B: Polym. Phys.* **2013**, *51*, 281–290.
- (318) Marques, D. S.; Vainio, U.; Chaparro, N. M.; Calo, V. M.; Bezahd, A. R.; Pitera, J. W.; Peinemann, K.-V.; Nunes, S. P. Self-Assembly in Casting Solutions of Block Copolymer Membranes. *Soft Matter* **2013**, *9*, 5557–5564.
- (319) Bucher, T.; Filiz, V.; Abetz, C.; Abetz, V. Formation of Thin, Isoporous Block Copolymer Membranes by an Upscalable Profile Roller Coating Process—A Promising Way to Save Block Copolymer. *Membranes* **2018**, *8*, 57.
- (320) Hibi, Y.; Hesse, S. A.; Yu, F.; Thedford, R. P.; Wiesner, U. Structural Evolution of Ternary Amphiphilic Block Copolymer Solvent Systems for Phase Inversion Membrane Formation. *Macromolecules* **2020**, *53*, 4889–4900.
- (321) Stegelmeier, C.; Exner, A.; Hauschild, S.; Filiz, V.; Perlich, J.; Roth, S. V.; Abetz, V.; Förster, S. Evaporation-Induced Block Copolymer Self-Assembly into Membranes studied by in Situ Synchrotron SAXS. *Macromolecules* **2015**, *48*, 1524–1530.
- (322) Goveas, J. L.; Milner, S. T. Dynamics of the Lamellar-Cylindrical Transition in Weakly Segregated Diblock Copolymer Melts. *Macromolecules* **1997**, *30*, 2605–2612.
- (323) Ibbeken, G. J. *Self-Assembly of Polymers in Presence of Solvent Evaporation*. M.Sc. Thesis, Georg-August University, Göttingen, Germany, 2020.
- (324) Hao, J.; Wang, Z.; Wang, Z.; Yin, Y.; Jiang, R.; Li, B.; Wang, Q. Self-Assembly in Block Copolymer Thin Films upon Solvent Evaporation: A Simulation Study. *Macromolecules* **2017**, *50*, 4384–4396.
- (325) Tsige, M.; Mattsson, T. R.; Grest, G. S. Morphology of Evaporated Multiblock Copolymer Membranes studied by Molecular Dynamics Simulations. *Macromolecules* **2004**, *37*, 9132–9138.
- (326) Berezkin, A. V.; Papadakis, C. M.; Potemkin, I. I. Vertical Domain Orientation in Cylinder-Forming Diblock Copolymer Films upon Solvent Vapor Annealing. *Macromolecules* **2016**, *49*, 415–424.
- (327) Li, W. H.; Nealey, P. F.; de Pablo, J. J.; Müller, M. Defect Removal in the course of Directed Self-Assembly is facilitated in the Vicinity of the Order-Disorder Transition. *Phys. Rev. Lett.* **2014**, *113*, 168301.
- (328) Takahashi, H.; Laachi, N.; Delaney, K. T.; Hur, S.-M.; Weinheimer, C. J.; Shykind, D.; Fredrickson, G. H. Defectivity in Laterally Confined Lamella-Forming Diblock Copolymers: Thermodynamic and Kinetic Aspects. *Macromolecules* **2012**, *45*, 6253–6265.
- (329) Glaser, J.; Medapuram, P.; Beardsley, T. M.; Matsen, M. W.; Morse, D. C. Universality of Block Copolymer Melts. *Phys. Rev. Lett.* **2014**, *113*, 068302.
- (330) Spencer, R. K. W.; Matsen, M. W. Coexistence of Polymeric Microemulsion with Homopolymer-Rich Phases. *Macromolecules* **2021**, *54*, 1329–1337.
- (331) Vorselaars, B.; Spencer, R. K. W.; Matsen, M. W. Instability of the Microemulsion Channel in Block Copolymer-Homopolymer Blends. *Phys. Rev. Lett.* **2020**, *125*, 117801.
- (332) Düchs, D.; Ganesan, V.; Fredrickson, G. H.; Schmid, F. Fluctuation Effects in Ternary AB + A + B Polymeric Emulsions. *Macromolecules* **2003**, *36*, 9237–9248.
- (333) Janert, P. K.; Schick, M. Phase Behavior of Ternary Homopolymer/Diblock Blends: Influence of Relative Chain Lengths. *Macromolecules* **1997**, *30*, 137–144.
- (334) Müller, M.; Schick, M. Bulk and Interfacial Thermodynamics of a Symmetric, Ternary Homopolymer-Copolymer Mixture: A Monte Carlo Study. *J. Chem. Phys.* **1996**, *105*, 8885–8901.
- (335) Geoghegan, M.; Krausch, G. Wetting at Polymer Surfaces and Interfaces. *Prog. Polym. Sci.* **2003**, *28*, 261–302.
- (336) Li, W.; Liu, M.; Qiu, F.; Shi, A.-C. Phase Diagram of Diblock Copolymers Confined in Thin Films. *J. Phys. Chem. B* **2013**, *117*, 5280–5288.
- (337) Michman, E.; Langenberg, M.; Stenger, R.; Oded, M.; Schwartzman, M.; Müller, M.; Shenhar, R. Controlled Spacing between Nanopatterned Regions in Block Copolymer Films Obtained by utilizing Substrate Topography for Local Film Thickness Differentiation. *ACS Appl. Mater. Interfaces* **2019**, *11*, 35247–35254.
- (338) Hopp-Hirschler, M.; Shadloo, M. S.; Nieken, U. Viscous Fingering Phenomena in the Early Stage of Polymer Membrane Formation. *J. Fluid Mech.* **2019**, *864*, 97–140.
- (339) Shojaie, S. S.; Krantz, W. B.; Greenberg, A. R. Dense Polymer Film and Membrane Formation via the Dry-Cast Process Part I. Model Development. *J. Membr. Sci.* **1994**, *94*, 255–280.
- (340) Yip, Y.; McHugh, A. J. Modeling and Simulation of Nonsolvent Vapor-Induced Phase Separation. *J. Membr. Sci.* **2006**, *271*, 163–176.
- (341) Krantz, W. B.; Greenberg, A. R.; Hellman, D. J. Dry-casting: Computer Simulation, Sensitivity Analysis, Experimental and Phenomenological Model Studies. *J. Membr. Sci.* **2010**, *354*, 178–188.
- (342) Barnett, J. W.; Bilchak, C. R.; Wang, Y.; Benicewicz, B. C.; Murdock, L. A.; Bereau, T.; Kumar, S. K. Designing Exceptional Gas-separation Polymer Membranes using Machine Learning. *Sci. Adv.* **2020**, *6*, No. eaaz4301.
- (343) Li, Y. M.; Zhang, Q.; Álvarez Palacio, J. R.; Hakem, I. F.; Gu, Y.; Bockstaller, M. R.; Wiesner, U. Effect of Humidity on Surface Structure and Permeation of Triblock Terpolymer derived SNIPS Membranes. *Polymer* **2017**, *126*, 368–375.

(344) Jung, A.; Rangou, S.; Abetz, C.; Filiz, V.; Abetz, V. Structure Formation of Integral Asymmetric Composite Membranes of Polystyrene-block-Poly(2-vinylpyridine) on a Nonwoven. *Macromol. Mater. Eng.* **2012**, *297*, 790–798.

(345) Dreyer, O.; Wu, M.-L.; Radjabian, M.; Abetz, C.; Abetz, V. Structure of Nonsolvent-Quenched Block Copolymer Solutions after Exposure to Electric Fields during Solvent Evaporation. *Adv. Mater. Interfaces* **2019**, *6*, 1900646.

(346) Ding, L.; Xu, R.; Pu, L.; Yang, F.; Wu, T.; Xiang, M. Pore Formation and Evolution Mechanism during Biaxial Stretching of β -iPP used for Lithium-ion Batteries Separator. *Mater. Des.* **2019**, *179*, 107880.

(347) Xu, T.; Goldbach, J. T.; Russell, T. P. Sequential, Orthogonal Fields: A Path to Long-Range, 3-D Order in Block Copolymer Thin Films. *Macromolecules* **2003**, *36*, 7296–7300.

(348) Wiesner, U. Lamellar Diblock Copolymers under Large Amplitude Oscillatory Shear Flow: Order and dynamics. *Macromol. Chem. Phys.* **1997**, *198*, 3319–3352.

(349) Chen, Z.-R.; Kornfield, J. A.; Smith, S. D.; Grothaus, J. T.; Satkowski, M. M. Pathways to Macroscale Order in Nanostructured Block Copolymers. *Science* **1997**, *277*, 1248–1253.

(350) Stangler, S.; Abetz, V. Orientation Behavior of AB and ABC Block Copolymers under Large Amplitude Oscillatory Shear Flow. *Rheol. Acta* **2003**, *42*, 569–577.

(351) Stangler, S.; Abetz, V. Orientation Behaviour of AB and ABC Block Copolymers under Large Amplitude Oscillatory Shear Flow in Bulk and in Concentrated Solution. *e-Polym.* **2002**, *2*. DOI: [10.1515/epoly.2002.2.1.234](https://doi.org/10.1515/epoly.2002.2.1.234)

(352) Sinturel, C.; Bates, F. S.; Hillmyer, M. A. High χ -Low N Block Polymers: How Far Can We Go? *ACS Macro Lett.* **2015**, *4*, 1044–1050.